STUDY OF ORBITAL ANGULAR MOMENTUM RADIO BEAMS

BASED ON UNIFORM CIRCULAR ANTENNA ARRAY

by

Lei Fang

APPROVED BY SUPERVISORY COMMITTEE:

_____

Rashaunda M. Henderson, Chair

_____

Andrew Blanchard

_____

Qing Gu

_____

Kenneth K. O

To my family

STUDY OF ORBITAL ANGULAR MOMENTUM RADIO BEAMS

BASED ON UNIFORM CIRCULAR ANTENNA ARRAY

by

LEI FANG, BS, ME

DISSERTATION

Presented to the Faculty of

The University of Texas at Dallas

in Partial Fulfillment

of the Requirements

for the Degree of

DOCTOR OF PHILOSOPHY IN

ELECTRICAL ENGINEERING

THE UNIVERSITY OF TEXAS AT DALLAS

May 2020

ACKNOWLEDGMENTS

STUDY OF ORBITAL ANGULAR MOMENTUM RADIO BEAMS

BASED ON UNIFORM CIRCULAR ANTENNA ARRAY

Lei Fang, PhD
The University of Texas at Dallas, 2020

Supervising Professor: Rashaunda M. Henderson, Chair

This research focuses on developing uniform circular antenna arrays (UCAs) for the generation and application of orbital angular momentum (OAM) modes at millimeter-wave (mm-wave). Uniform circular arrays offer the potential of implementing a planar compact solution for emulating a twisted wave. In theory, multiple twisted waves can be multiplexed on one channel to increase communication capacity. In this dissertation, four main efforts have been undertaken to advance OAM designs for radio waves. First, an OAM-UCA factor using the cylindrical coordinate system has been derived and simulated in MATLAB, which can give the correct radiation pattern and phase distribution results in seconds, compared to time-consuming electromagnetic (EM) simulation. The OAM-UCA factor has been verified using the simulated and measured results, which shows its correctness. Secondly, based on the OAM-UCA factor and the intrinsic properties of OAM, a quantitative method to verify the OAM mode purity generated by the UCA has been developed. This capability can provide insight to optimize OAM-UCAs without lengthy design efforts. Thirdly, dipole UCAs have been realized for generating OAM mode 1 and 3 at lower E-band (71 to 76 GHz) by using 0.127 mm thickness

FR408 substrate. To improve the radiation gain, patch UCAs on a different packaging material have been realized for generating OAM modes 1, 2 and -3. Finally, 8-patch OAM-UCAs have been fabricated for the demonstration of the OAM radio link at the WiFi band (2.4 GHz).

TABLE OF CONTENTS

LIST OF FIGURES

xvi

Figure G.7. The fifth mask for the 67 GHz patch UCA fabrication on TerraGreen® substrate.134

LIST OF TABLES

CHAPTER 1

INTRODUCTION

1.1 Motivation

The explosive growth in the number of wireless devices and the demand for portable information content has led to the need for modern wireless systems with higher and higher communication capacity, and this trend will keep increasing as 5G comes [1]. Based on Shannon's theory, one direct method to increase communication capacity is to increase the bandwidth, which is one of the reasons to move to higher frequency bands, where more bandwidth can be occupied. The Federal Communications Commission (FCC) has granted the use of the higher frequency spectrum for future wireless systems such as 28 GHz and 39 GHz [2]. Based on Nokia, using 32 GHz, the link capacity can be 5 Gbps and the latency would be 50 µs [3], if utilizing V-band or E-band, the link capacity can achieve 20 Gbps with only 10 µs latency. However, all of these achievements are based on more bandwidth with the higher carrier frequency, therefore it is important to develop new methods to increase channel capacity for applications including 5G mm-wave wireless systems. One promising approach to increase capacity that has been explored in optics and radio frequency (RF) is the use of orbital angular momentum (OAM) [4], [5] [32], which is based on the OAM modes orthogonality. Other than frequency division multiplexing (FDM), time division multiplexing (TDM), polarization division multiplexing (PDM) and code division multiplexing (CDM), OAM provides a new dimension – OAM mode division multiplexing (MDM) to increase communication capacity. In 2012, the researchers in [6] successfully conducted the first OAM multiplexing based radio communication experiment at 2.4 GHz. In 2018, Nippon Telegraph and Telephone (NTT)

Corporation successfully demonstrated a 100 Gbps wireless transmission system using orbital angular momentum (OAM) multiplexing at 28 GHz [7], [8]. In [9], the researchers claimed that the combination of OAM and mm-wave or even THz will be applied in 6G.

1.2 Orbital angular momentum concept

In theory, OAM can be generated from the Laguerre-Gaussian (LG) modes, which are the solutions of the paraxial Helmholtz equation under the cylindrical coordinate system [10], where the expression of the LG mode - $u(r, \varphi, z)$ is given in 1.1:

$$u(r,\varphi,z) = \frac{C_{lp}^{LG}}{w(z)}\left(\frac{\sqrt{2}r}{w(z)}\right)^{|l|} exp\left(\frac{-r^2}{w^2(z)}\right) L_p^{|l|}\left(\frac{2r^2}{w^2(z)}\right) \exp\left(-ik\frac{r^2}{2R(z)} - ikz + i\psi(z)\right) \exp(-il\varphi)$$

$$(1.1)$$

In equation 1.1, the last term - $\exp(-il\varphi)$ is the OAM term, where l is the OAM mode order which can be any integer, and it indicates that the OAM beam has a helical phase front with a $2\pi l$ phase twist. When $l = 0$, it is a plane wave, which means the phase distribution at a plane perpendicular to the transmission direction is unique. When $l \neq 0$, the phase distribution at that plane will change with the azimuth angle φ, and the wavefront will be vortex-like, and the polarity of l will contribute to the phase changing direction with respect to φ. Figure 1.1 shows the properties of the LG beams carrying different OAM modes.

1.3 Orbital angular momentum radio beam generation

The first and most important step for OAM based radio communication is how to generate a radio wave carrying OAM. One way to do so is by passing a plane wave through a

spiral phase plate (SPP) [11]–[12]. The SPP introduces a specific phase delay to generate an

OAM mode by its thickness, which varies azimuthally based on 1.2:

| | Intensity | Phase | Wavefront |

$l = 0$

$l = +1$

$l = +2$
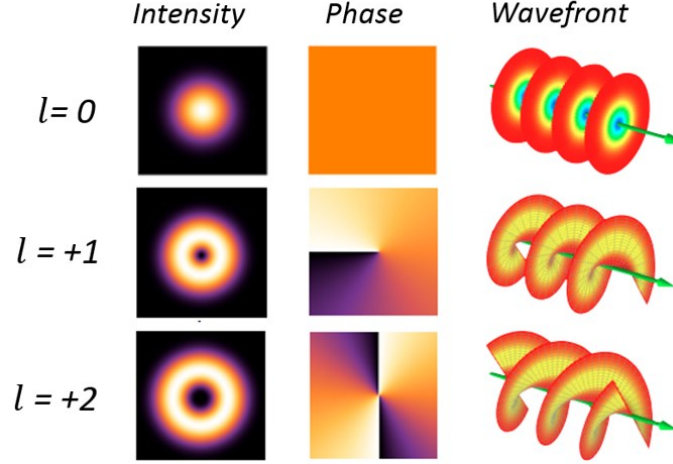
Figure 1.1. Intensity and phase of LG modes of different orders [10].

$$S = l/(n - 1) \tag{1.2}$$

Where S is the step height, n is the refractive index of the phase plate material, and l is

the OAM mode that the SPP generated [11].

However, the SPP is usually too large to realize a light-weight and miniaturized system,

which will limit its applications. In [13], the SPP radius realized by the authors is 15 cm for an E

band communication system, and Figure 1.2 shows the SPP structure realized in [13].

A time-switched array (TSA) or time modulated circular antenna array (TMCA) can also

be a solution to generate OAM radio beams [14], [15]. In [14], the authors' theoretical simulation

results verified that a circular TSA can be configured to generate OAM radiation modes at the

frequencies of $f_0 + l \cdot f_s$, where f_0 is the fundamental frequency, l is the OAM mode order, and

f_s is the overall switching frequency, which equals $1/T_s$, and T_s is the overall sequence switch

period (the time to sequentially switch all the array elements). The perfect OAM mode can only be generated at a single frequency point, and if a wideband signal is transmitted, it will be distributed over different OAM modes, which will be a challenge for the receiver. Increasing f_s can avoid this, but high-speed RF switches are required. This dilemma will limit its application in the millimeter-wave domain.
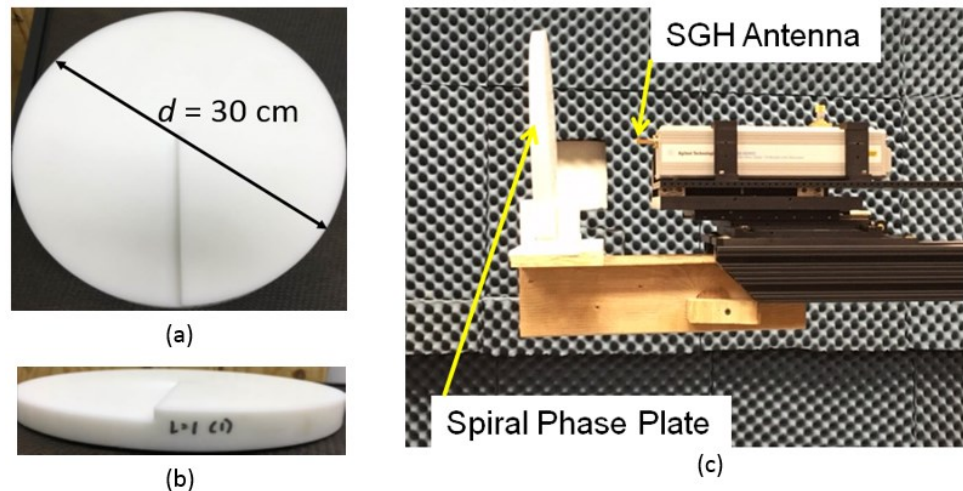
Figure 1.2. The SPP structure realized in [11].

Several researchers utilized a horn antenna to generate OAM radio beams [16]-[20]. In [16], the authors integrated the conventional horn antenna with a single-layer perforated planar dielectric lens by covering its aperture to generate OAM mode 1 at 50 GHz. One can treat this as a special case of SPP application for OAM radio wave generation. In [17], [18], the authors proposed a novel method to generate higher-order OAM modes based on a conical horn antenna. This method utilizes the two orthogonal polarization degenerate TE_{mn} modes in a circular waveguide through a mode-transformation section. Based on their theoretical analysis, the design can achieve OAM mode m at r and φ direction and mode $m-1$ at $x-$ and $y-$direction. In

[19], [20], the authors realized higher-order OAM modes generation by combining the different TE_{mn} modes in a horn antenna with SPP.

Generating OAM radio waves using uniform circular arrays (UCA) is an attractive method, since it is compact and easy to fabricate. [21] illustrated the requirements for a N-element UCA to generate OAM mode l, which indicates that the power fed to each element should be equal and have a $2\pi l/N$ phase shift between adjacent elements, and the minimum N should be $2|l| + 1$.

Initially, some researchers took the concept of OAM as the angular momentum (AM). Based on [10], AM is a measure to describe the amount of dynamical rotation that exists in the electromagnetic (EM) field. Besides transmitting in a straight line, an EM beam can also be "rotating" around its own axis, and this "rotating" contains two parts: "spinning" and "twisting". Therefore, AM is the combination of spin angular momentum (SAM) and orbital angular momentum (OAM), where SAM controls the polarization, and OAM controls the twisted wavefront. In [21]-[23], the authors built circular antenna arrays to generate "OAM" radio waves, however, the antenna elements in the array were all not in the same polarization, and their observation in the simulation and measurement were the properties of AM not OAM. This was already verified by [24], where one should extract the OAM mode from the AM mode by involving the SAM. The simplest method to extract the OAM mode is by making the SAM = 0, corresponding to linear polarization (LP). The array in [25] is the first reported linearly polarized circular patch array to generate OAM mode -1 at 10 GHz, where the array was realized on a 1.6 mm thickness FR4 substrate with an overall diameter of 60 mm.

1.4 OAM beams for RF communication state of the art

The theoretical foundation that using OAM can increase communication capacity is based on the fact that different order OAM modes are orthogonal to each other. This orthogonality feature allows for multiplexing and de-multiplexing different OAM modes carrying independent data, as a result, the total channel capacity and spectral efficiency can be increased [5]. In [6], the first experimental OAM-based radio communication link was built and demonstrated by involving two radio beams over a distance of 442 meters at 2.4 GHz. The authors have experimentally transmitted two data beams at the same frequency channel but encoded two different OAM modes. An untwisted radio beam with OAM mode 0 and the twisted one with OAM mode +1 were transmitted in parallel using a Yagi-Uda antenna and a helicoidal parabolic antenna at 2.4 GHz. The two beams were differentiated by the differential output of a pair of antennas at the received side over a distance of 442 meters.

In [5], the authors demonstrated a high-capacity millimeter-wave link at a carrier frequency of 28 GHz using four independent OAM beams with 2 polarizations in a laboratory environment, increasing the data rate by a factor of 8, thereby achieving 32 Gbps (1 Gbaud × 4 bit/symbol × 4 OAM beams × 2 polarizations). Eight multiplexed OAM beams were generated using SPPs and transmitted along the same spatial axis through 2.5 meters. They were sequentially recovered using the appropriate SPP, which can untwist an OAM beam back to an approximate Gaussian beam and be efficiently coupled into the receiver antenna.

In [26], the anthors presented a short-range experimental OAM based 60 GHz communication link using patch antenna arrays. The propagation distance, in that case, was 15 centimeters. The authors stacked a four-element patch array for generating OAM mode -1 with

an eight-element patch array for generating OAM mode +2 to multiplex two OAM beams at the transmitter. At the receiver, the team used an SPP to demultiplex desired OAMs independently. Thereby 8 Gbps (2 Gbaud × 2 bit/symbol × 2 OAM beams) mm-wave wireless communication link was achieved.

The most recent work by Nippon Telegraph and Telephone (NTT) corporation successfully demonstrated a 100 Gbps OAM based wireless transmission system at 28 GHz, where they achieved bit error rate (BER) free transmission over a distance of 10 meters by using OAM mode -2, -1, 0, +1, and +2, and the transceiver designed was based on two 16-element antenna arrays and one single antenna [7], [8], [27].

1.5 Dissertation Outline

The dissertation is organized with the following structure: Chapter 2 gives the concept of the uniform circular antenna array (UCA) factor for orbital angular moment (OAM) mode generation, and introduces a simple method to check OAM mode purity. Chapter 3 illustrates the study of OAM generating at lower E-band (71-76 GHz) using dipole UCAs. Chapter 4 presents the patch OAM-UCA at 67 GHz. Chapter 5 provides the experiments using 2.4 GHz patch UCAs for an OAM wireless communication demonstration. The conclusion and future work are detailed in Chapter 6.

CHAPTER 2

OAM-UCA FACTOR IN THE CYLINDRICAL COORDINATE SYSTEM

2.1 Introduction

As illustrated in Chapter 1, orbital angular moment (OAM) is supported by Laguerre-Gaussian (LG) modes, where the LG modes are the solutions of the paraxial Helmholtz equation under the cylindrical coordinate system [10]. The uniform circular array (UCA) can be used to generate a radio beam carrying LG modes, which is a radio beam with OAM. As mentioned in Chapter 1, besides the antenna type, the OAM-UCA radiation performance is determined by the number of elements (N) and the radius (a) of the array. The traditional OAM-UCA design process based on EM simulation tools is shown in Figure 2.1, the criterion to verify whether an OAM-UCA is good or not is to check its radiation pattern and phase distribution results, and also the feasibility of realizing the feed network in practical terms. To optimize an OAM-UCA's radius and the number of elements for a given OAM mode l, the optimization process in the EM simulation tools like ANSYS HFSS, can take hours or even days. The initial motivation to develop the OAM-UCA factor design method is to get rid of the time-consuming EM simulation process, with the method one is able to determine the radiation pattern and phase distribution results quickly for the UCA formed by ideal radiators.
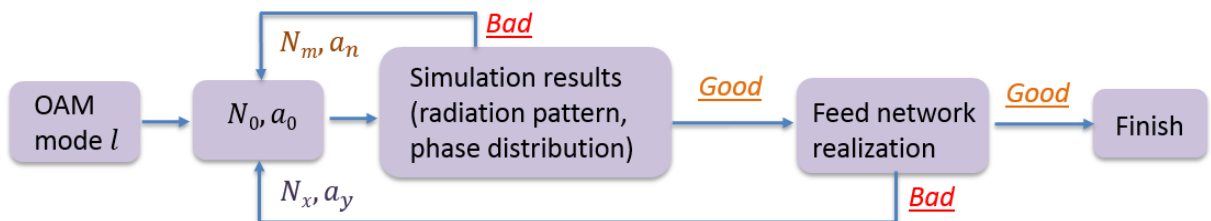
Figure 2.1. The traditional OAM-UCA design process based on EM simulation tools.

The radio beams generated by the traditional antenna and its array are usually analyzed in the spherical coordinate system [28]. However, for the radio beams carrying non-zero OAM modes, the spherical coordinate is not suitable, because of the requirement to utilize the phase distribution information on a plane which is perpendicular to the radio beam propagation direction. Based on the orthogonality property among different OAM modes, the phase information can be used to do the multiplexing and de-multiplexing. In the spherical coordinate system, expressing the radiation phase result on a plane is not convenient, while the cylindrical coordinate system will provide a straightforward result. This is the intrinsic motivation to use the cylindrical coordinate system rather than the spherical one to express OAM radio beams generated by UCAs.

This chapter focuses on the OAM-UCA factor application in the design process based on MATLAB simulation. The OAM-UCA factor in cylindrical coordinates has been programmed with MATLAB, and used to optimize the radiation performance and sidelobe level. This information can be used in advance to predict the number of elements and the radius of the OAM-UCA, instead of running lengthy EM simulation in the traditional design process. The measured results of a 73 GHz 8-patch UCA sample matches the simulation results, and verifies the correctness of the OAM-UCA factor and MATLAB code.

2.2 OAM-UCA factor in the cylindrical coordinate system

Figure 2.2 depicts a N-element UCA and the corresponding parameters in the cylindrical coordinate system, its accumulated E-field distribution at field point (r, φ, z) can be written as:

$$E(r, \varphi, z) = \sum_{n=1}^{N} a_n \cdot \frac{e^{-ikR_n}}{R_n} \cdot \exp[-i(l \cdot \varphi_n' + \varphi_{0n}')] \qquad (2.1)$$

9
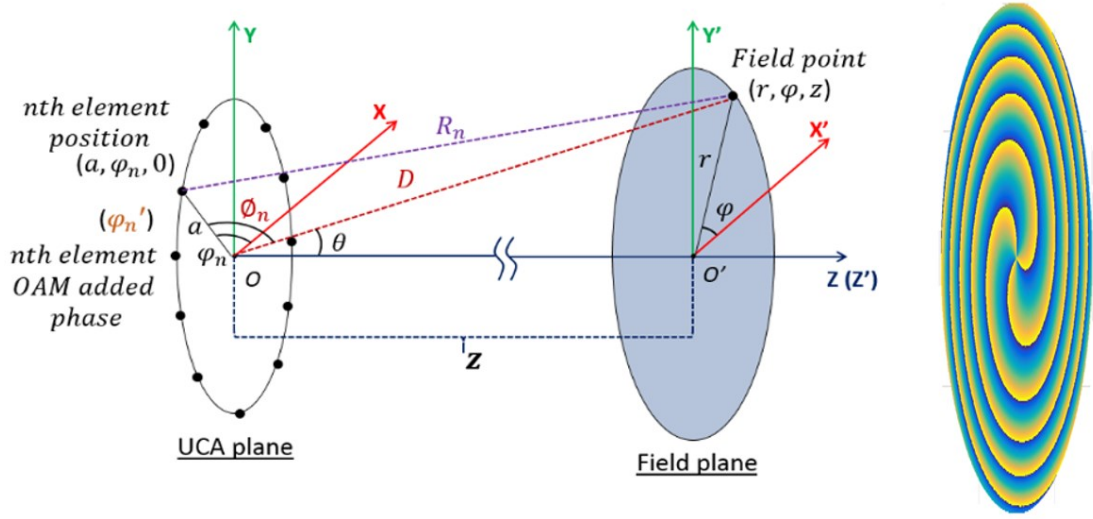
Figure 2.2. Illustration of OAM-UCA in the cylindrical coordinates.

Here, R_n stands for the distance from the array element (source point) to the field point, a_n is the amplitude of each element. For an ideal UCA, the elements are all the same and the amplitude can be normalized to 1. l stands for the OAM mode order, and $l \cdot \varphi_n' + \varphi_{0n}'$ is the OAM-added phase for each element, where $\varphi_n' = 2\pi n/N$, and φ_{0n}' is the intrinsic phase of each element. For an ideal UCA, the intrinsic phase of each element should be the same, and for simplicity, it could be set to zero. The prime notation here is to differentiate the OAM-added phase to the element's physical position phase term ($\phi_n = 2\pi n/N$), k is the wave number, which is $2\pi/\lambda$. a is the OAM-UCA radius, which is a measure of the UCA size. One should notice that in 2.1, the isotropic radiator is used to represent the individual element in the UCA, which gives the term, e^{-ikR_n}/R_n.

Based on the Cosine theorem, R_n can be expressed in 2.2:

$$R_n = \sqrt{a^2 + D^2 - 2aD\cos\phi_n} \qquad (2.2)$$

Where,

10

$$D = \sqrt{z^2 + r^2} \tag{2.3}$$

Where r is the field plane radius.

For $\cos\emptyset_n$, it can be expressed as a dot product of the unit vectors:

$$\cos\emptyset_n = \hat{a}_a \cdot \hat{a}_D \tag{2.4}$$

Where $\hat{a}_a$ is the unit vector of the UCA radius a, and in Cartesian coordinates system, it can be expressed as:

$$\hat{a}_a = \hat{a}_x\cos\varphi_n + \hat{a}_y\sin\varphi_n \tag{2.5}$$

And $\hat{a}_D$ is the unit vector of D, which is the distance between UCA center point O to the field point. In the Cartesian coordinates system, it can also be expressed as:

$$\hat{a}_D = \hat{a}_x\sin\theta\cos\varphi + \hat{a}_y\sin\theta\sin\varphi + \hat{a}_z\cos\theta \tag{2.6}$$

So the dot product of 2.5 and 2.6 will be:

$$\hat{a}_a \cdot \hat{a}_D = \sin\theta\,\cos(\varphi - \varphi_n) = \frac{r\cos(\varphi-\varphi_n)}{\sqrt{z^2+r^2}} \tag{2.7}$$

Substituting 2.3 and 2.7 into 2.2, R_n can be expressed as 2.8:

$$R_n = \sqrt{a^2 + z^2 + r^2 - 2ar\cos(\varphi - \varphi_n)} \tag{2.8}$$

In the far-field range, there will be $z^2 + r^2 \gg a^2$, and use the approximation $\sqrt{1 + x} \approx 1 + x/2$ (when $x \ll 1$), R_n could be simplified as:

$$R_n \approx \sqrt{z^2 + r^2} - \frac{ar\cos(\varphi-\varphi_n)}{\sqrt{z^2+r^2}} \tag{2.9}$$

As shown in 2.1, R_n exists in both phase and amplitude of the radiated field, in the far-field range, for the phase term, equation 2.9 is used, and for amplitude, R_n could be simplified as $R_n \approx D = \sqrt{z^2 + r^2}$.

Then the E-field distribution will be (after arrangement):

$$E(r, \varphi, z) = \frac{e^{-ik\sqrt{z^2+r^2}}}{\sqrt{z^2+r^2}} \sum_{n=1}^{N} \exp\left[\frac{ikar\cos(\varphi-\varphi_n)}{\sqrt{z^2+r^2}}\right] \cdot \exp[-i(l \cdot \varphi_n')] \qquad (2.10)$$

In 2.10, the second term after the summation notation contributes to OAM twisted phase distribution, and the first term is the contribution from the UCA elements' positions.

The UCA element position phase (φ_n) and OAM-added phase (φ_n') both equal to $2\pi n/N$, so φ_n' in 2.10 can be replaced with φ_n. And a new term, ϕ_n is defined, which stands for the result of $\varphi - \varphi_n$, therefore, $\varphi_n = \varphi - \phi_n$, then 2.10 can be expressed as:

$$E(r, \varphi, z) = \frac{e^{-ik\sqrt{z^2+r^2}}}{\sqrt{z^2+r^2}} \cdot \exp(-il\varphi) \times \sum_{n=1}^{N} \exp\left[\frac{ikar\cos(\phi_n)}{\sqrt{z^2+r^2}}\right] \cdot \exp(il\phi_n)$$

$$(2.11)$$

Here, the term - $\exp(-il\varphi)$ is shown, which is the OAM phase distribution term.

When UCA elements number - N gets bigger and bigger, the summation operator will become an integral. To realize it, a term, $\Delta\phi_n$, needs to be added here:

$$\Delta\phi_n = \phi_n - \phi_{n-1} = \varphi - \varphi_n - (\varphi - \varphi_{n-1}) = \varphi_{n-1} - \varphi_n = -\frac{2\pi}{N} \qquad (2.12)$$

then 2.12 can be expressed as:

$$E(r, \varphi, z) = \frac{e^{-ik\sqrt{z^2+r^2}}}{\sqrt{z^2+r^2}} \cdot \exp(-il\varphi) \cdot \frac{1}{\Delta\phi_n} \cdot \sum_{n=1}^{N} \exp\left[\frac{ikar\cos(\phi_n)}{\sqrt{z^2+r^2}}\right] \exp(il\phi_n) \cdot \Delta\phi_n$$

$$(2.13)$$

When $N \to \infty$, $\Delta\phi_n$ will be close to 0, and the summation operator turns into an integral, and changes ϕ_n to ϕ, $\Delta\phi_n$ to $d\phi$, therefore:

$$E(r, \varphi, z) = -\frac{e^{-ik\sqrt{z^2+r^2}}}{\sqrt{z^2+r^2}} \cdot \exp(-il\varphi) \cdot \frac{N}{2\pi} \cdot \int_0^{2\pi} \exp\left[\frac{ikar\cos(\phi)}{\sqrt{z^2+r^2}}\right] \cdot \exp(il\phi)\, d\phi$$

(2.14)

From the Bessel's first integral:

$$J_n(x) = \frac{1}{2\pi i^n} \int_0^{2\pi} \exp(ix \cdot \cos\theta) \cdot \exp(in\theta)d\theta \qquad (2.15)$$

So

$$\int_0^{2\pi} \exp\left[\frac{ikar\cos(\phi)}{\sqrt{z^2+r^2}}\right] \cdot \exp(il\phi)\, d\phi = 2\pi i^l \cdot J_l\left(\frac{kar}{\sqrt{z^2+r^2}}\right)$$

(2.16)

Then the accumulated E field distribution at field point (r, φ, z) can be written as:

$$E(r, \varphi, z) = -N \cdot i^l \cdot \frac{\exp(-ik\sqrt{z^2+r^2})}{\sqrt{z^2+r^2}} \cdot \exp(-il\varphi) \cdot J_l\left(\frac{kar}{\sqrt{z^2+r^2}}\right)$$

(2.17)

In 2.17, the term - $\exp(-il\varphi)$ is the OAM phase term, which contributes to the twisted phase distribution along the transmission direction. Until here, the OAM-UCA factor derivation under the cylindrical coordinate system is finished. 2.17 is the integral form OAM-UCA factor since it is achieved from the integral equation (2.16), and 2.1 is summation form OAM-UCA factor. One should notice that 2.17 is the ideal case, and it cannot be realized using the UCA

13

technique. It is only used as the reference to evaluate the performance of a finite element OAM-UCA.

Here, the UCA's radiation pattern is proportional to $|E(r, \varphi, z)|^2$, so for the OAM mode $l \neq 0$, the first kind Bessel function, $J_l(kar/\sqrt{z^2 + r^2})$, generates the center null in the radiation pattern, and the higher the l, the larger the center null. Figure 2.3 illustrates the curves of the first kind Bessel function with different orders.
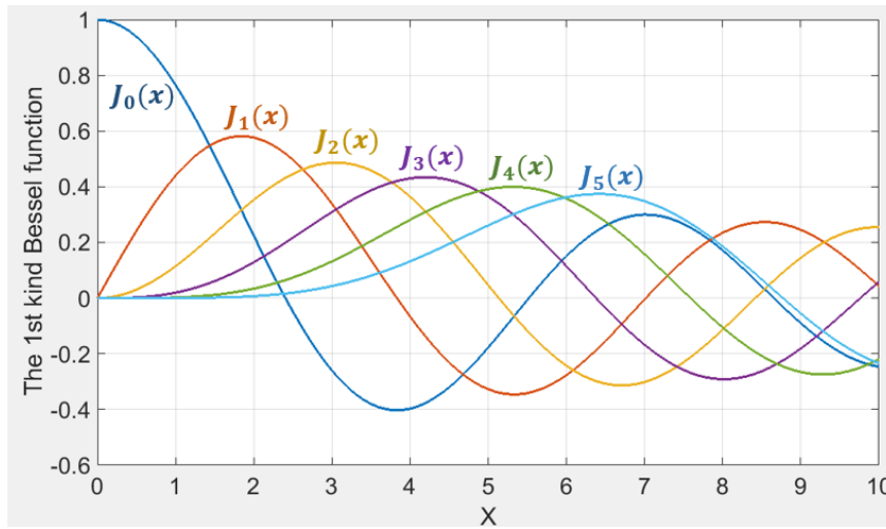
Figure 2.3. Illustration of the first kind Bessel function of different orders.

In Figure 2.3, for the first kind Bessel function with a fixed order, the peak position depends on its index, x. In 2.17, $x = kar/\sqrt{z^2 + r^2}$. By taking the definition of the elevation (or azimuth) angle of the planar coordinates, a new index is defined – the divergent angle (θ) for the OAM-UCA factor, where $\theta = sin^{-1}(r/\sqrt{z^2 + r^2})$, and 2.17 can be rewritten as:

$$E(r, \varphi, z) = -N \cdot i^l \cdot \frac{\exp(-ik\sqrt{z^2+r^2})}{\sqrt{z^2+r^2}} \cdot \exp(-il\varphi) \cdot J_l(k \cdot a \cdot sin\theta) \qquad (2.18)$$

In 2.18, for the non-zero OAM modes, the smaller UCA radius will give the larger divergent angle, which is consistent with the HFSS simulation and experiment measurement results.

Based on 2.1 and 2.17, a MATLAB code was developed, which can be used as the reference in designing an optimized UCA for OAM mode generation, the code is given in Appendix A.

2.3 MATLAB based OAM-UCA factor application

A. UCA element number for ripple-free OAM modes

As illustrated in Chapter 1, the minimum number of elements (N) of an OAM-UCA to generate OAM mode l should be satisfied as $N \geq 2\,|l| + 1$. For example, the minimum N for OAM mode 1 generation is 3, and in the MATLAB code, different N values were used to verify the phase distribution. Figure 2.4 shows the results of a fixed radius 1.5 λ radius UCA with 3, 4, 6 and 8 elements for OAM mode 1 generation at 73 GHz, where λ is the wavelength in the vacuum of 73 GHz. The phase response indicates that the OAM mode 1 is generated in the center area for all cases.

In [29], the authors illustrated that even the number of elements (N) satisfies the minimum requirement, and if N is not big enough, there will be ripples in the radiation pattern. Figure 2.5 shows the normalized radiation patterns of the same number of elements as in Figure 2.4. For $N = 3$ and 4, the radiation peak ring is not formed, and for $N = 6$, ripples exist in the peak ring and high sidelobes are still shown. When $N = 8$, there are no observed ripples on the peak ring, which has the same shape of the ideal case (∞-element UCA), and appears as the

minimum requirement for OAM mode 1 ripple-free radiation. The meaning for the ripple-free radiation is related to OAM mode purity, which will be discussed in the next section.
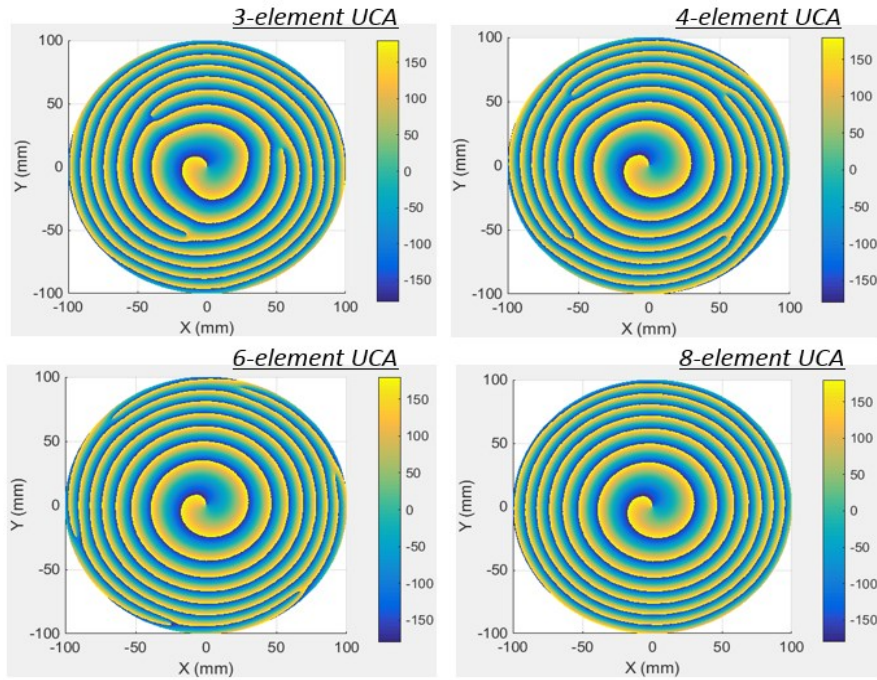
Figure 2.4. The electric field phase distribution of 1.5 λ radius UCA for OAM 1 generation with 3, 4, 6 and 8 elements.
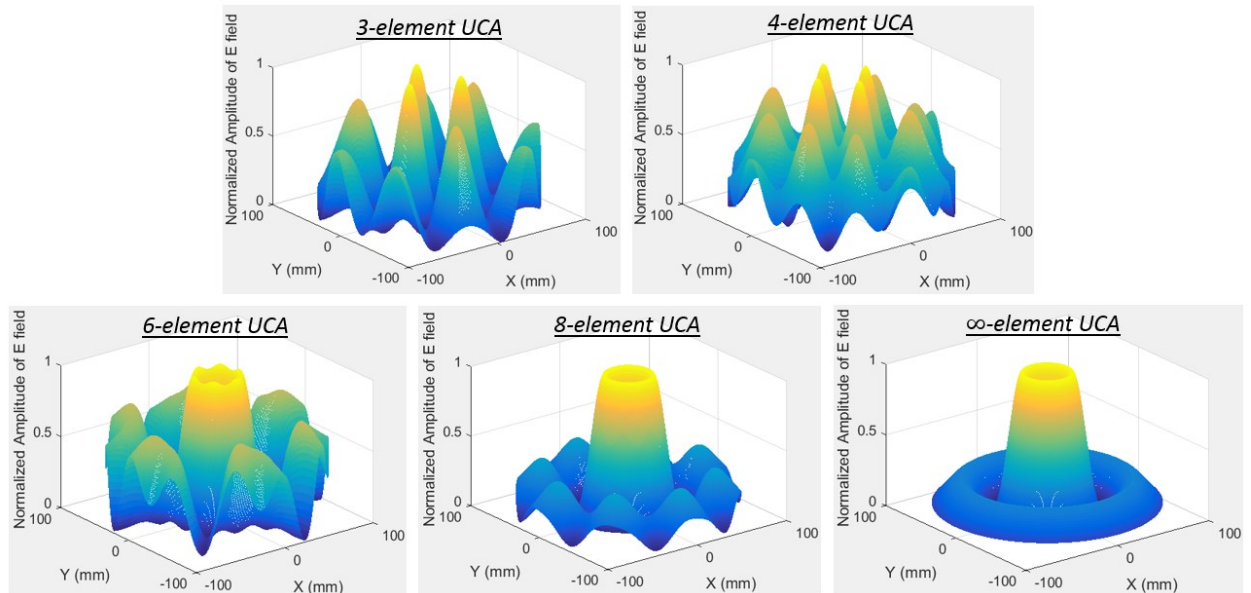
Figure 2.5. The normalized radiation pattern of 1.5 λ radius UCA for OAM 1 generation with 3, 4, 6, 8 and ∞ elements.

Based on 2.1, the ripple-free radiation is a strong function of N, but has a weak dependence on the UCA radius, unless the UCA radius is at the same level with the observation distance, while that is the extreme case and will not be analyzed in this work.

The same simulations for OAM modes 2, 3, 4 and 5 were performed to determine the minimum N needed to achieve ripple-free results, which is shown in Figure 2.6. The UCA element number requirements for peak radiation ripple-free is: $N = 12$ for OAM mode 2, $N = 14$ for OAM 3, $N = 16$ for OAM mode 4 is 16, and $N = 18$ for OAM mode 5.
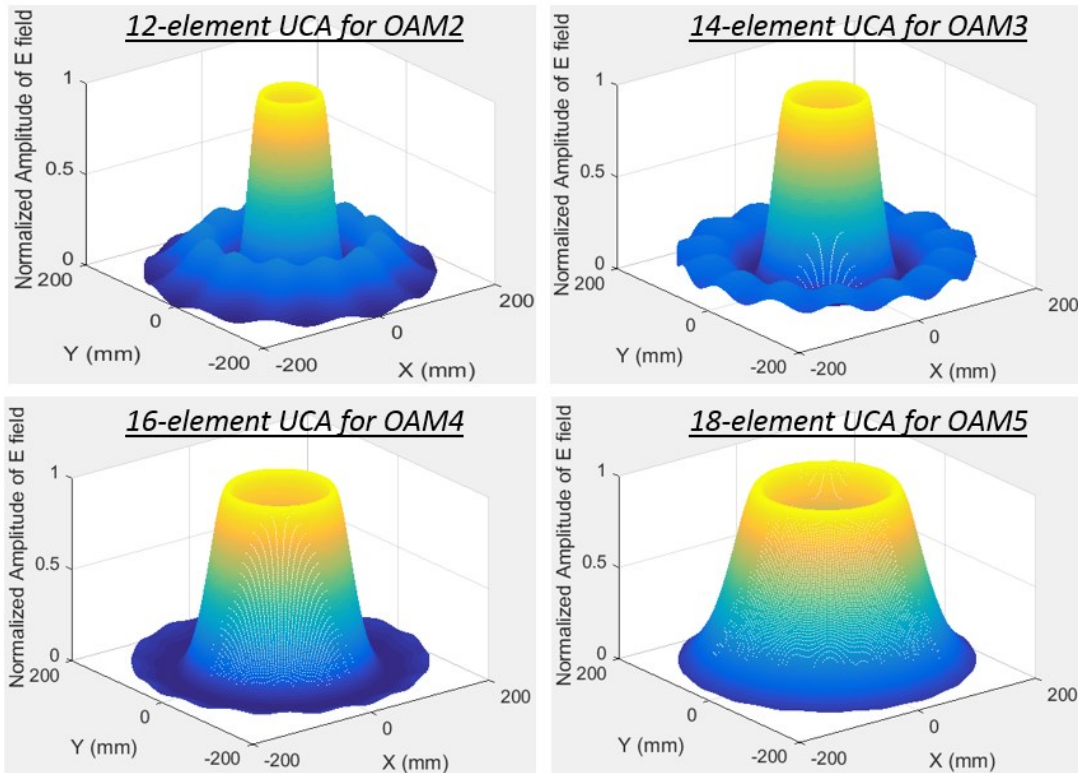
Figure 2.6. The normalized radiation pattern of 1.5 λ radius UCA for OAM 1 generation with 3, 4, 6, 8 and ∞ elements.

B. UCA radius effect

An 8-element UCA was used to check the radius effect, and the results are shown in Figure 2.7. The smallest UCA radius (0.5λ) has no sidelobes in the observing range, and the

corresponding divergent angle is about 30°. As the UCA radius increases, the divergent angle becomes smaller. However, after the radius is greater than 1.25λ, the divergent angle does not change too much, while one more sidelobe appears and the level of the first sidelobe becomes higher. An $a = 1.25\lambda$ could be a good stopping point for OAM mode 1 radius optimization, which will give about 13° divergent angle.
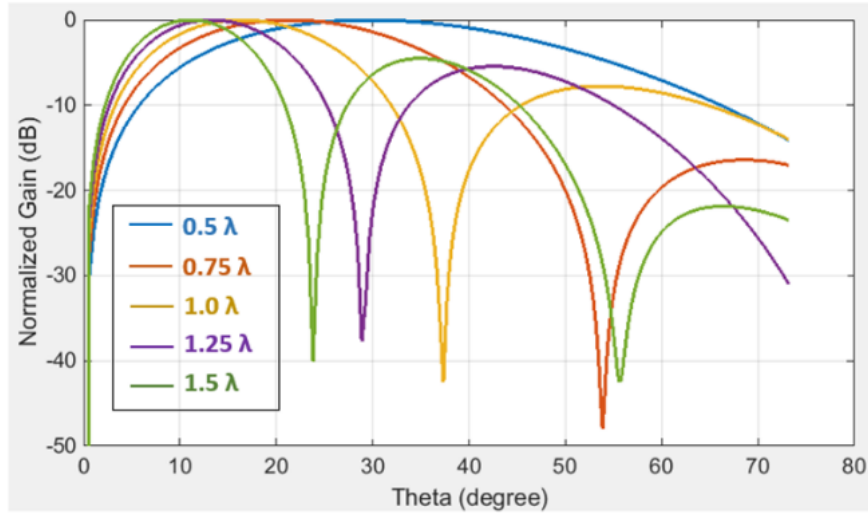
Figure 2.7. The normalized radiation pattern generated by an 8-element UCA for OAM mode 1 with the different radii.

Following the same procedure of OAM mode 1, the UCA radius was optimized for OAM modes 2 to 5. The standard for selecting the optimal radius is that the size only creates 1 sidelobe but with a relatively smaller divergent angle (standard #1). Figure 2.8 gives the results of the optimal radius vs. all the OAM modes, which is labeled as standard #1. The optimal UCA radius is roughly in a linear relationship with the corresponding OAM mode, which can be expressed as below:

$$a(\lambda) = 1.09 + 0.16 \times l \tag{2.19}$$

In Figure 2.8, the divergent angle has been fixed to 13° for all the OAM modes (standard #2), and the optimal radius determined using the MATLAB code. The linear relationship between the UCA radius and OAM mode still holds in standard #2, which can be expressed as 2.20, but the slope is 6.4 times higher than standard #1.

$$a(\lambda) = 0.225 + 1.225 \times l \qquad (2.20)$$
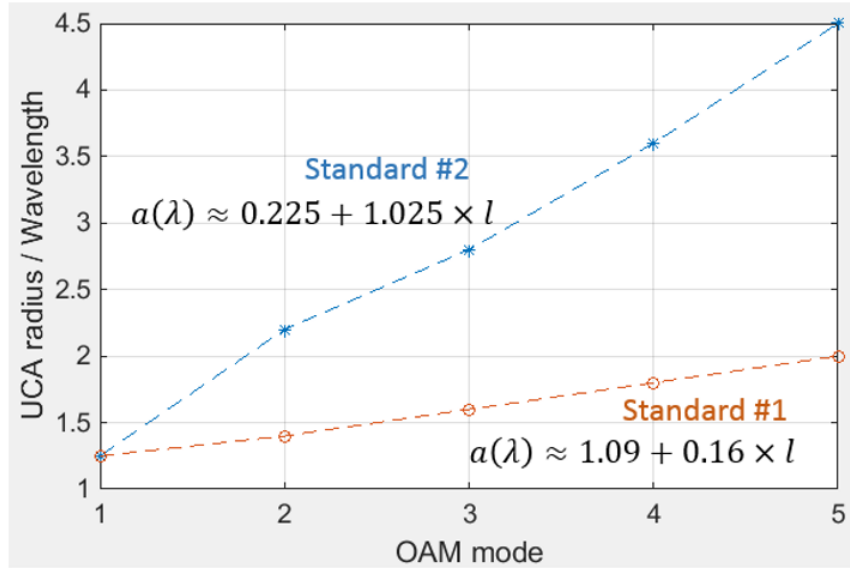
Figure 2.8. The OAM UCA optimal radius vs. all the OAM mode for standard #1 and #2 (13° divergent angle).

C. Verification of MATLAB with HFSS simulation and measurement

To verify the OAM-UCA radius and the number of elements effect, 4 and 8 elements UCA with different radii were utilized to generate OAM mode 1 at 73 GHz. Figure 2.9 shows the top view of the 3-D radiation pattern generated by MATLAB and ANSYS HFSS, and the MATLAB based OAM-UCA factor simulation results show good agreement with the ANSYS HFSS results. Both OAM-UCA and ANSYS HFSS simulation results verify the effect of the number of elements and radius of a UCA: with the same number of elements of the UCA, the

larger the UCA radius is, the smaller peak radiation divergent angle and more sidelobes will be. And with the same radius for a fixed OAM mode order, the more elements of a UCA, the less variation on the peak radiation ring and lower level sidelobes will be. The ANSYS HFSS simulation setup is given in Appendix B.

The key point is that running the OAM-UCA based MATLAB simulation takes seconds compared to ANSYS HFSS, which will take at least minutes or even hours to draw the structure, configure the simulation setup and then provide the results. During the OAM-UCA design process, this is important and can help one quickly decide the UCA radius and the number of elements for generating the desired OAM mode.

An 8-patch UCA for OAM mode 1 at 73 GHz was fabricated in the UT Dallas cleanroom and measured in a spherical chamber to verify the OAM-UCA factor [30]. The substrate used is a 0.127 mm thick FR408 ($\varepsilon_r = 3.75$, $tan\delta = 0.018$ at E-band) with 0.012 mm copper-clad thickness. The simulation is based on ANSYS HFSS to design the patch size to make it resonate at 73 GHz and achieve a 75 Ω input impedance. An 8-patch UCA for OAM mode 1 was realized with the in-plane feed network. Figure 2.10 shows the structure of the single patch and the UCA with a radius of 1.25λ at 73 GHz, which is the optimal value as shown in Figure 2.8. 75 Ω microstrip lines are used here to form the UCA's in-plane feed network, which is optimized to provide uniform power distribution for the individual patch and 45-degree phase shift between adjacent elements, so that the OAM mode 1 will be generated.
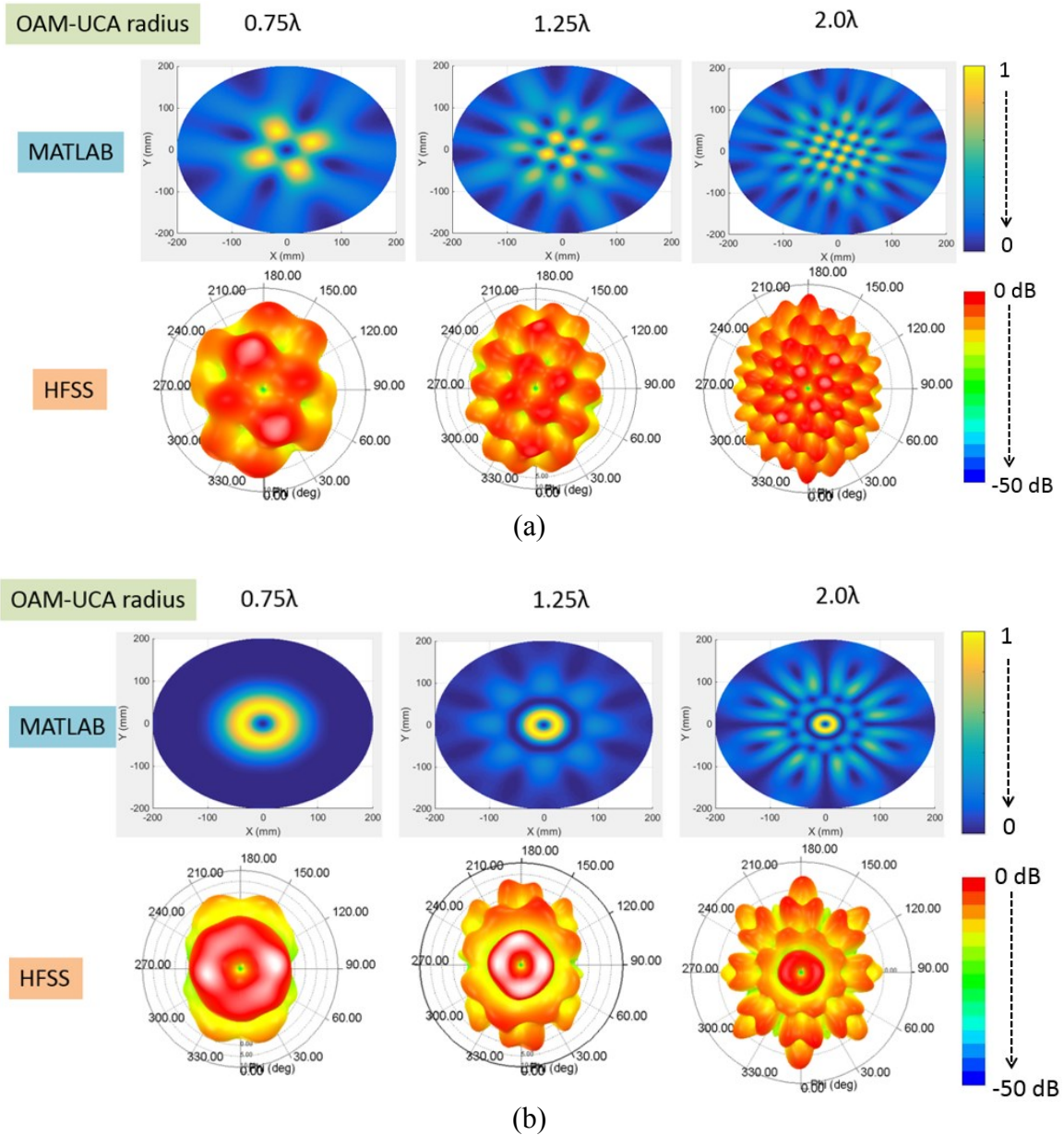
Figure 2.9. The results comparison between the OAM-UCA factor-based MATLAB simulation and ANSYS HFSS simulation. (a) 4-element UCA for OAM mode 1 @ 73 GHz; (b) 8-element UCA for OAM mode 1 @ 73 GHz.
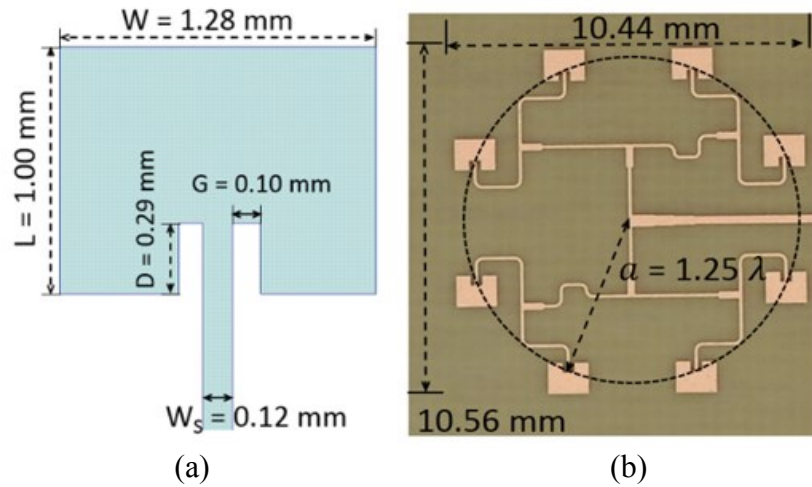
Figure 2.10. The 8-patch UCA for OAM mode 1 at 73 GHz verification: (a) single patch size; (b) 8-element patch UCA size.
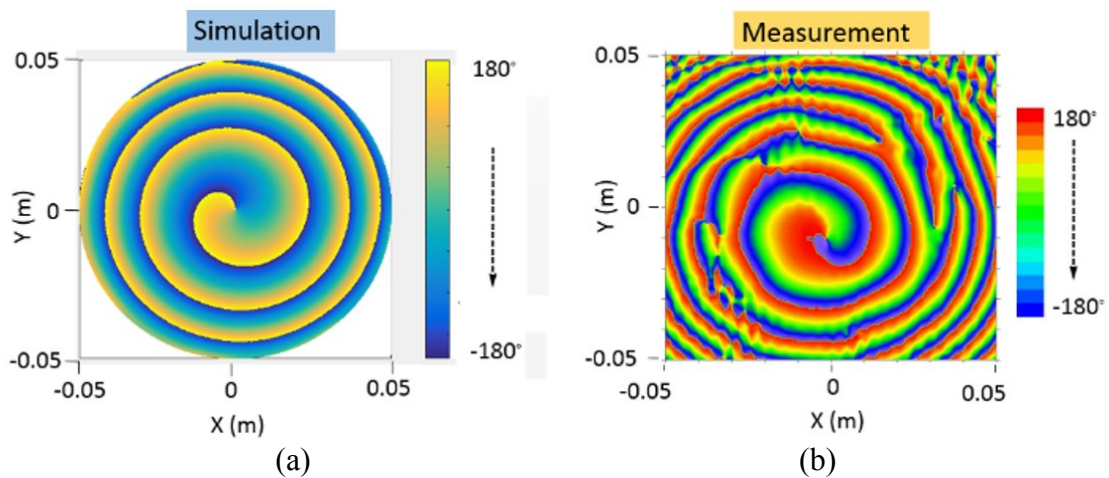
Figure 2.11. Phase distribution at 73 GHz of the 8-patch UCA for OAM mode 1: (a) MATLAB simulation based on OAM-UCA factor; (b) Chamber measurement.

Figure 2.11 shows the phase distribution of the 8-element patch UCA, and OAM mode 1 is generated in both simulation and measurement. The variation in the measured phase is influenced by the AUT stand and other measurement equipment in the chamber.

Figure 2.12 shows the 3D radiation pattern of the 8-patch UCA for OAM mode 1 for the HFSS simulation results and spherical chamber measurement results. Where the sample includes

the in-plane feed network with the 8 patches. The MATLAB coded OAM-UCA factor cannot

simulate the feed network effect and is shown in Figure 2.10 (b) for the 1.25λ radius case.

(a)   (b)
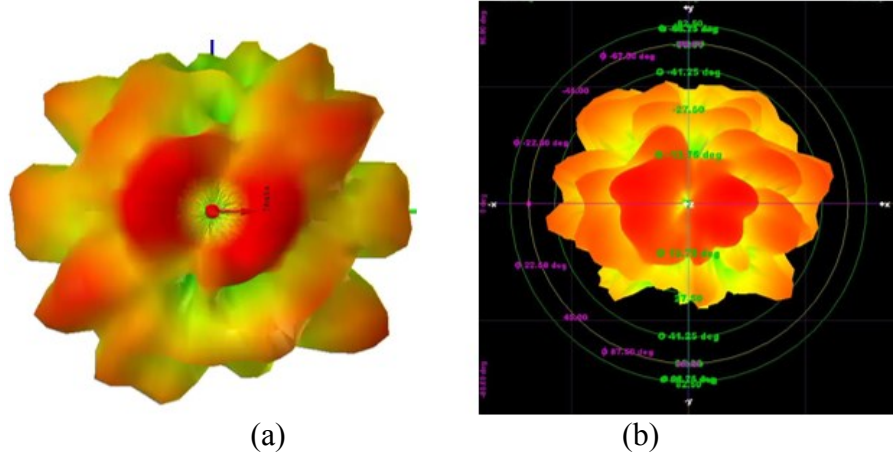
Figure 2.12. 3D radiation pattern at 73 GHz of the 8-patch UCA for OAM mode 1 on FR408 substrate: (a) HFSS simulation; (b) Chamber measurement.

To compare the radiation pattern in detail, Figure 2.13 shows the results of the OAM-UCA factor simulation, ANSYS HFSS simulation, and chamber measurement together. For the main lobes, the divergent angle appears at 13-degree and has the same beamwidth for all cases, which indicates OAM-UCA factor based MATLAB simulation is in good agreement with ANSYS HFSS simulation and chamber measurement. Regarding the first sidelobes, the positions are roughly at 43-degree for all, while the HFSS simulation and measurement show a narrower beamwidth and lower level compared to the MATLAB response. The reason is that the MATLAB simulation is only equation-based, which assumes the UCA elements are isotropic radiators and perfectly fed, while in HFSS and measurement, the patch antenna is used to build the UCA, which does not radiate isotropically. In addition, the microstrip feed network will impact the radiation pattern.
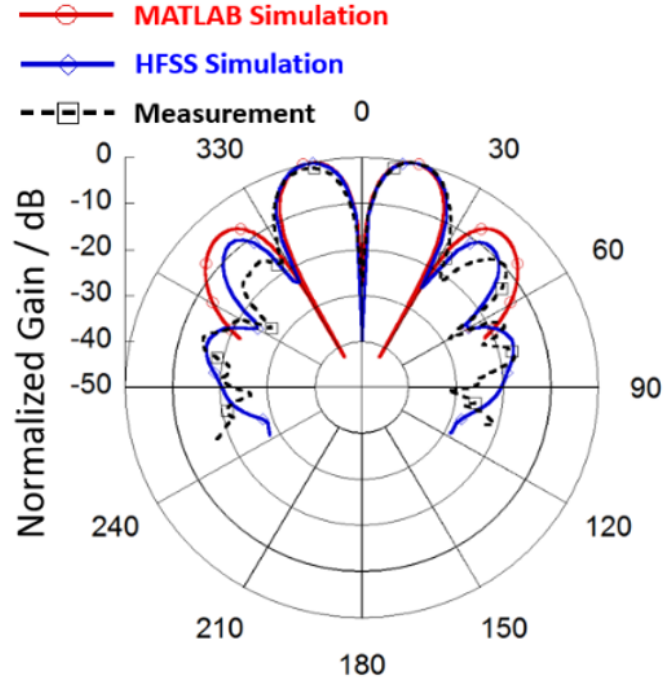
Figure 2.13. Normalized radiation pattern at 73 GHz of the 8-patch UCA for OAM mode 1.

2.4 OAM-UCA mode purity

Although the OAM mode can be generated by the UCA method or other methods, there always a question about the OAM mode purity. This section introduces a MATLAB-based OAM mode purity verification method.

The idea to check the OAM mode purity is based on the orthogonality property among different OAM modes. Like the Fourier series, the phase distribution at the observation plane of any method generated OAM mode can be written as below [31]:

$$\Psi(\varphi) = \sum_{l=-\infty}^{\infty} A_l * \exp(-il\varphi) \tag{2.21}$$

$$A_l = \int_{-\pi}^{\pi} \Psi(\varphi) * \exp(il\varphi) \, d\varphi \tag{2.22}$$

Where, $\Psi(\varphi)$ in 2.21 describes the total phase distribution result along the observation plane, l is the OAM mode number, A_l is the amplitude of the corresponding OAM mode.

Although 2.17 indicates that the OAM mode phase distribution also has a r-dependent term, to check the OAM mode purity, one only needs to take the integral along the phi-plane. The r-dependent term will not affect the result, which can be merged into A_l and make it into a complex number, where the magnitude of the A_l can be used as the measure to verify the purity of OAM mode l. The mode purity check method can be illustrated in Figure 2.14, the phase mask for OAM mode l is the term - $\exp(il\varphi)$ in 2.22. Based on this idea, a MATLAB code was developed to verify the OAM mode purity, and the code detail is shown in Appendix C.
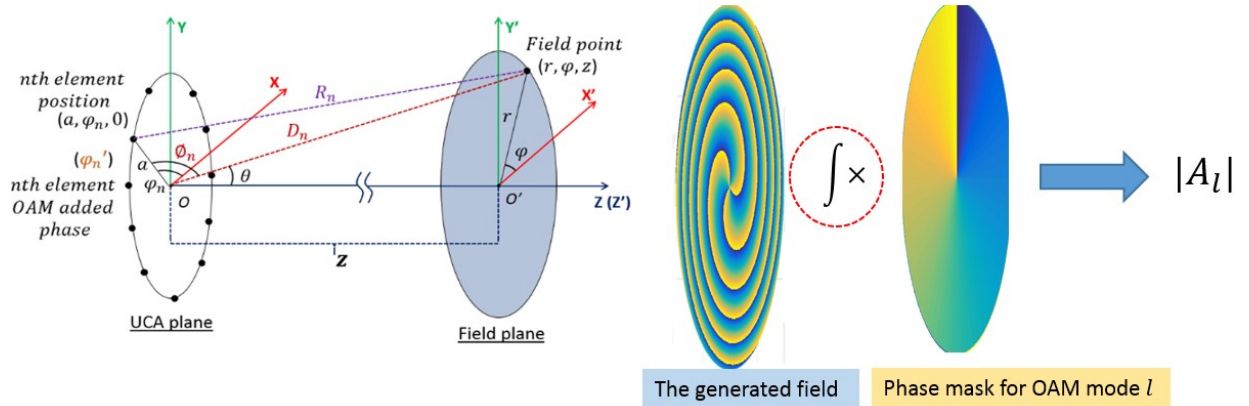
Figure 2.14. The illustration of the OAM mode purity verification method.

The OAM modes generated by equation 2.17 were verified, which is the integral form OAM-UCA factor and should generate the perfect OAM mode in theory. Figure 2.15 shows 3 examples of the phase distribution results of the generated OAM modes and the verification results using this method. In the mode purity plots in Figure 2.15, the X-axis is the OAM mode order and Y-axis is the mode purity percentage, the generated modes have 100% purity, which is expected.
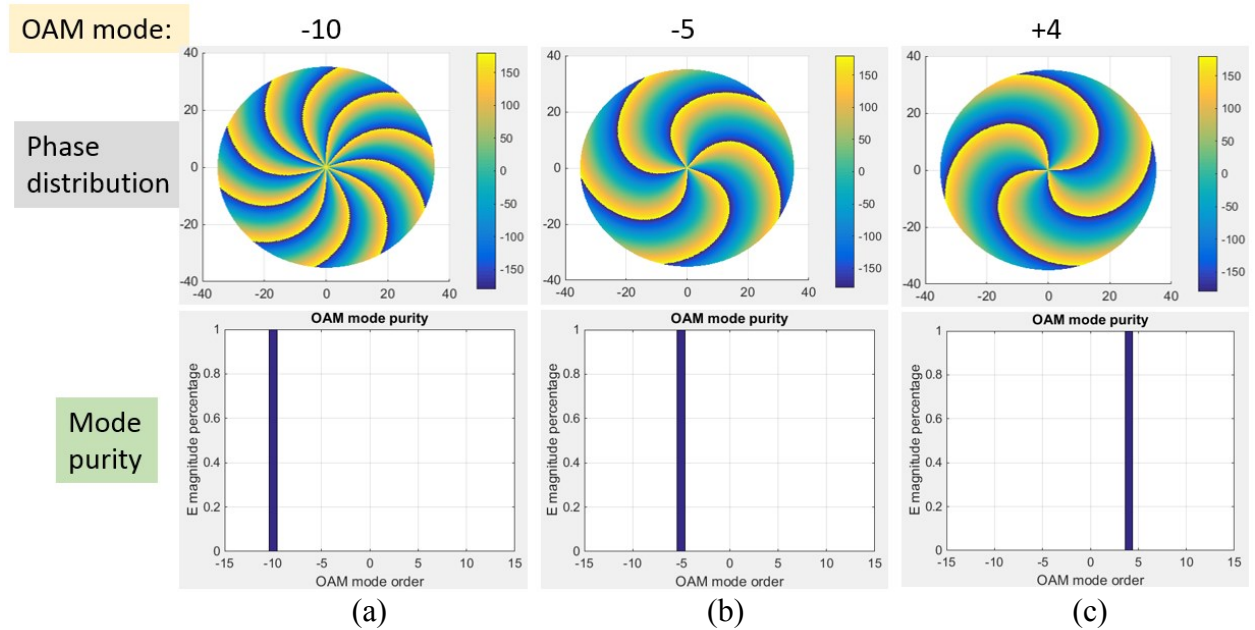
Figure 2.15. The generated OAM modes and the verification results: (a). OAM mode = -10; (b) OAM mode = -5; (c). OAM mode = + 4.

The purity of the OAM modes generated by the UCAs with the different number of elements were verified, the corresponding mode is generated using equation 2.1. Two concepts are introduced here: the spurious OAM mode and the minimum number of elements of an OAM-UCA for generating the pure mode. They are demonstrated using OAM mode 1 at 73 GHz as an example. The OAM-UCA radius is set as $a = 1.25\lambda$, where λ is the wavelength of 73 GHz in the vacuum. The distance from the observation plane to the UCA plane is set as $z = 30\,\lambda$, which meets the far-field condition. The observation plane radius $r = 50$ mm, and this is also the phase mask radius for checking the OAM mode purity. The number of elements (N) of the UCA is varied to check the mode purity. Results of $N = 2, 3, 4, 6$ and 8 are shown in Figure 2.16.

For $N = 2$, the correct mode is not generated, in the mode purity plots, it not only contains the mode 1, but also generates modes at -5, -3, -1, +3 and +5, named those undesired

26

modes as 'spurious' modes. Among them, mode -1 has the highest level, and then ± 3 modes, and then ± 5. The spurious mode (l_S) will be generated at

$$l_S = l + m * N \tag{2.23}$$

Where l is the desired OAM mode, N is the number of elements in the OAM-UCA, m can be any integer.

The highest spurious mode will be:

$$l_{S\_highest} = \begin{cases} l + N, & when\ l < 0 \\ l - N, & when\ l > 0 \end{cases} \tag{2.24}$$

For $N = 3$, which is the minimum requirement for OAM mode 1 generation, one can tell from the phase distribution result, the correct mode is generated. However, it only contains 68.92% correct mode, 21.51% mode -2, 4.54% mode +4, 1.68% mode -5. The results satisfy 2.23.

For $N = 4$, it contains 82.36% correct mode, 12.15% mode -3, 1.96% mode +5.

For $N = 6$, it contains 92.89% correct mode, 2.24% mode -5.

For $N = 8$, it contains 94.86% correct mode, other modes are below 1%.
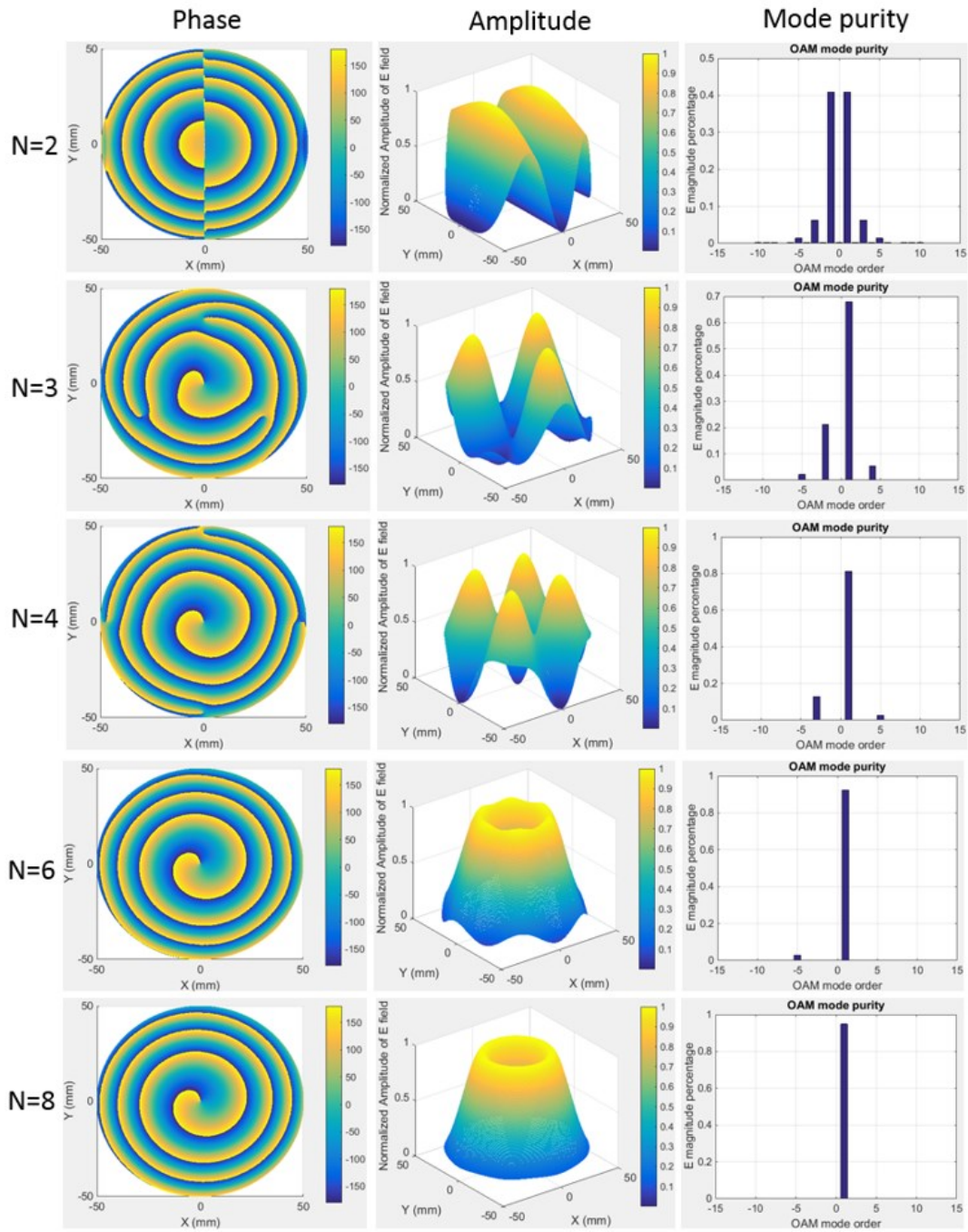
Figure 2.16. The generated OAM modes and the verification results with the different number of elements.

By increasing the number of elements beyond 8 will not improve the mode purity too much, and in the real design case, too many elements will make OAM-UCA design unrealistic, especially for the feed network design.

By keeping the same observation distance (30λ), the observation plane radius (the purity-checking mask size), and combining with section 2.3, the OAM mode purity of the OAM-UCAs, which with the peak ripple-free number of elements requirement (Figure 2.6) and 13-degree peak radiation divergent angle (Standard #2 of Figure 2.8) for OAM mode 2, 3, 4 and 5 were verified. The divergent angle fixed for different modes so that the purity-checking mask size is fixed and the purity checking results are fair for all the modes.

Table 2.1 lists the results. Based on this configuration, the mode purity for all the OAM-UCAs are all about 95%, and all the other spurious OAM modes are suppressed at the level lower than 1%. A mode with at least 95% purity is considered as the 'pure' OAM mode. Besides, the mode purity here refers to the magnitude of the electric field, if changing it to the power, then the 95% purity in the magnitude of the electric field means over 99.7% purity in the power. Thirdly, the definition of the ripple-free radiation in section 2.3 means the pure OAM mode. To my knowledge, this is the first time one has illustrated the relationship between ripple-free radiation and OAM mode purity.

The spurious modes are caused by a 180-degree phase ambiguity [10], and less phase difference between adjacent elements can ease the phase ambiguity effect. This is the reason more elements are required in an OAM-UCA to generate pure OAM mode.

Table 2.1. OAM mode purity verification results

OAM mode	The number of elements in the UCA	Radius / λ @ 73 GHz	Mode purity
1	8	1.25	94.86 %
2	12	2.05	94.64 %
3	14	2.80	94.76 %
4	16	3.60	94.85 %
5	18	4.50	95.04 %

Table 2.2. Phase mask radius vs. the purity of the OAM mode 2 generated by 8-element UCA with 2.05 λ radius at 73GHz

The phase mask radius (mm)	OAM mode 2 purity
100	74.44 %
50	82.09 %
40	90.30 %
30	93.11 %
20	94.61 %

The observation area or the phase mask size effect on the OAM mode purity is verified as the reference for selecting the receiver size of the OAM-multiplexing based wireless communication system. As an example, Figure 2.16 shows an 8-element UCA to generate OAM mode 2 at 73 GHz is selected, where the radius is 2.05λ, the observation distance is kept as 30 λ. Based on the results in Figure 2.6, an UCA with only 8 elements cannot generate the pure OAM mode 2, however, by decreasing the phase mask size, the mode purity checking result will be better, which means the 'pure' mode is limited in the radiation center area. Table 2.2 summarizes the relationship between the phase mask size and OAM mode 2 purity based on this setup. Due to the intrinsic property of the non-zero OAM mode, the center area of the radiation pattern has lower power, even though the mode is purer there, which is the trade-off to select receiver size. One standard that can be used in selecting the receiver size is to make it roughly the same size with the peak radiation angle, which can balance the power and the mode purity. For instance, in

Figure 2.17, a mask radius between 30 mm and 40 mm, which can capture more power and keep

the mode purity over 90%.
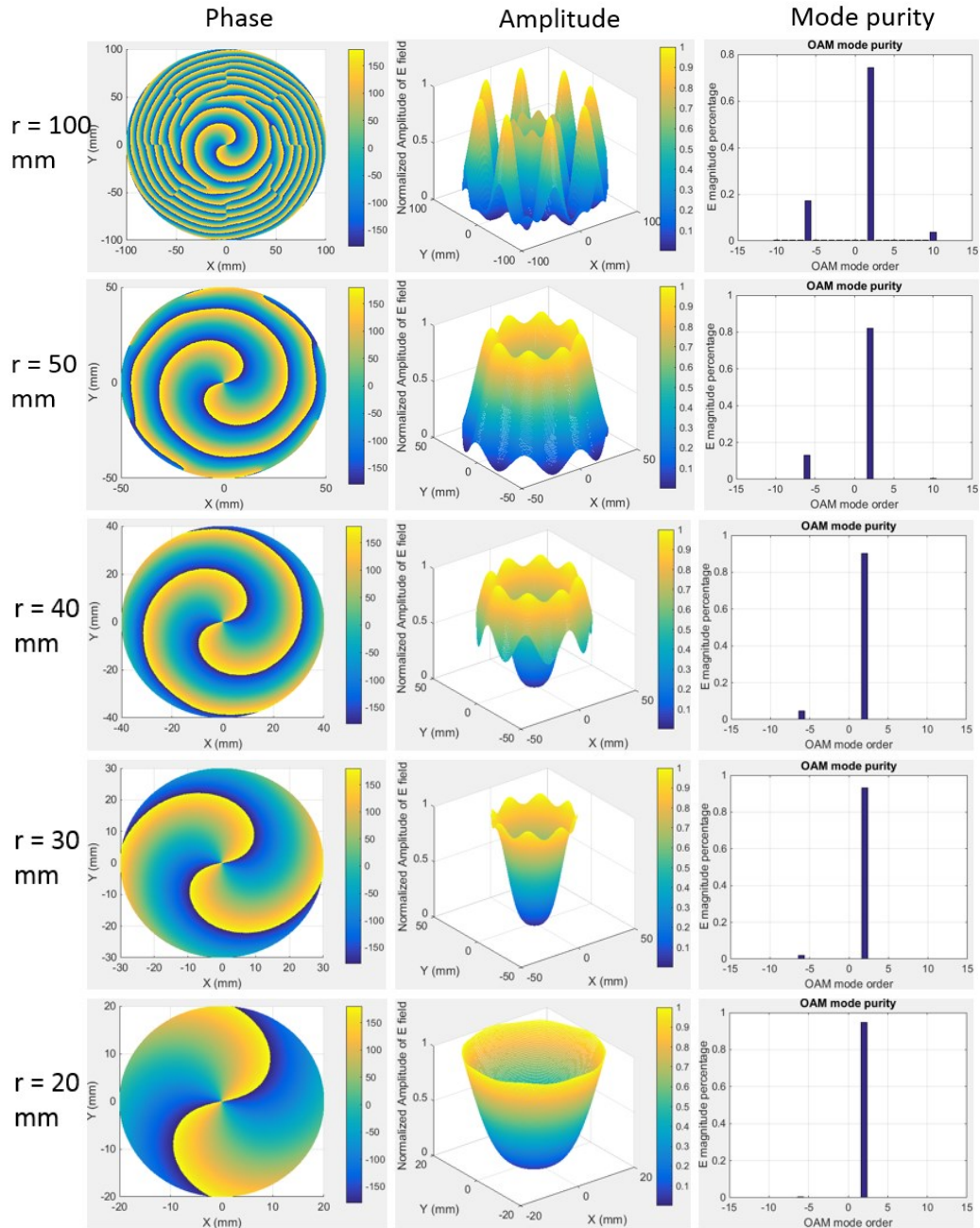
Figure 2.17. The generated OAM modes and the verification results using 8-element UCA for OAM mode 2 generation.

2.5 Conclusion

In this chapter, the OAM-UCA factor was developed under the cylindrical coordinate system, and coded in MATLAB. Compared to the lengthy ANSYS HFSS simulation, the OAM-UCA factor-based MATLAB simulation takes only seconds and gives the same results, which can accelerate OAM-UCA design. Based on the OAM-UCA factor, in the second section, The results of UCA elements number requirement for generating a ripple-free radiation pattern was given. The radius effect on the radiation pattern was verified and optimized for OAM mode up to 5. A 73 GHz 8-element patch UCA realized on FR408 substrate was used to verify the MATLAB code, where both the measured radiation pattern and the phase distribution match the simulated one. In the last section, a simple method to check the OAM mode purity was introduced, where the ripple-free radiation introduced in section 2.3 is proved that the OAM mode is pure, this is the first time to describe a relationship between OAM mode purity and the corresponding UCA's radiation pattern. In the end, the checking mask size effect on OAM mode purity was verified, which provides an idea for the OAM multiplexing based OAM communication system, which is limiting the receiver or aperture size to be about the same as the peak radiation ring. This would be a good choice, which can balance the OAM mode purity and the receiving power.

CHAPTER 3

DIPOLE UCA FOR OAM MODE GENERATION

3.1 Introduction

The patch antenna is used at first to realize an UCA for OAM generation [25], however, the patch has narrow bandwidth intrinsically, which will limit its application in wideband millimeter-wave (mm-wave) communication. The patch antenna would also suffer more loss from the substrate loss tangent, which will decrease the radiation efficiency [33]. The free space path loss is in proportion to $1/f^2$, where f is the frequency, so the mm-wave wireless communication will suffer more path loss than traditional centimeter-wave (cm-wave) [34]. Therefore, the antenna radiation efficiency is more important in mm-wave wireless communication, and the higher radiation efficiency, the more coverage area. Due to these reasons, dipole antennas are utilized as the UCA element to generate OAM modes. Figure 3.1 compares the results of the single dipole and patch antenna both centered at the 73 GHz and designed on the same substrate, which indicates the dipole occupies less area, has wider bandwidth and higher radiation efficiency than the patch.

Isola® FR408

0.012 mm copper clad

0.127 mm

$\varepsilon_r \approx 3.75$ @ E band
$loss \tan \approx 0.018$ @ E band

	Outlook	Size	Bandwidth	Radiation efficiency
Dipole		1.60 mm × 0.11 mm	27.0 %	88.5 %
Patch		1.28 mm × 0.99mm	4.2 %	60.8 %
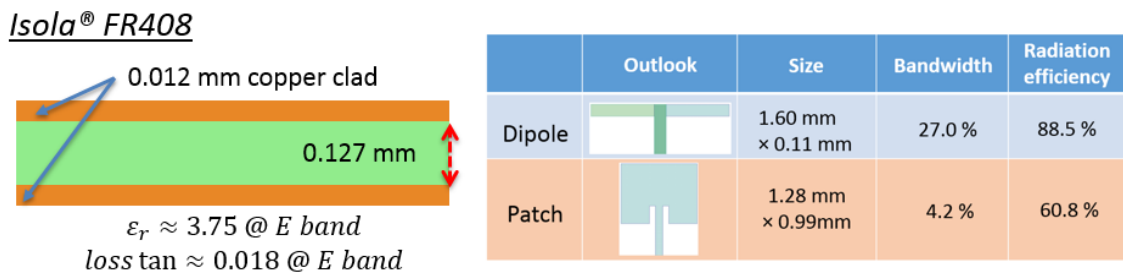
Figure 3.1.The comparison results of the single dipole and patch antenna designed on FR408 substrate and centered at 73 GHz.

3.2 Dipole antenna theory [35]

Dipole antenna theory is well studied, especially for the half-wavelength dipole, and in this chapter, all the dipole UCAs are realized using the half-wavelength dipole. Figure 3.2 shows the half-wavelength dipole structure in the spherical coordinate system. The total length of the dipole is l, which is $\lambda/2$. To obtain the dipole antenna radiation pattern at the far-field range, the analysis starts from current distribution along the dipole, and takes the dipole as a tiny thin one, which makes it only have length-dependent current distribution. The dipole is fed from its center with a differential and balanced current signal, and the current distribution on the half-wavelength dipole can be written as 3.1, which describes the current distribution on half-wavelength dipole has sinusoidal form with nulls at the endpoints, where k is the wavenumber.
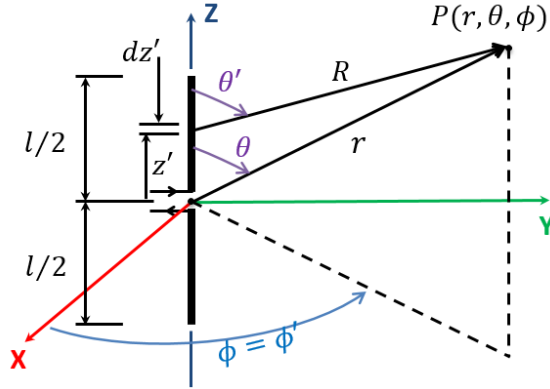
Figure 3.2. Dipole geometry.

$$I(x' = 0, y' = 0, z') = \begin{cases} \hat{a}_z I_0 \sin\left[k\left(\frac{l}{2} - z'\right)\right], \ where \ 0 \le z' \le l/2 \\ \hat{a}_z I_0 \sin\left[k\left(\frac{l}{2} + z'\right)\right], \ where \ -l/2 \le z' \le 0 \end{cases} \tag{3.1}$$

Using a far-field assumption, the radiation only has E_θ and H_ϕ components, where E_θ is the electric field in θ direction, and H_ϕ is the magnetic field in ϕ direction. The equation is

shown in 3.2, and they are in-phase. E_θ is Z_0 times of H_ϕ, where Z_0 is the free space impedance, which is 120π Ω.

$$E_\theta = jZ_0I_0 \frac{e^{-jkr}}{2\pi r} \left[\frac{\cos\left(\frac{kl}{2}\cos\theta\right) - \cos\left(\frac{kl}{2}\right)}{\sin\theta} \right] \tag{3.2a}$$

$$H_\phi = jI_0 \frac{e^{-jkr}}{2\pi r} \left[\frac{\cos\left(\frac{kl}{2}\cos\theta\right) - \cos\left(\frac{kl}{2}\right)}{\sin\theta} \right] \tag{3.2b}$$

Then the average Poynting vector can be written as:

$$\boldsymbol{W_{av}} = \frac{1}{2}Re[E \times H^*] = \hat{a}_r \frac{1}{2\eta}|E_\theta|^2 = \hat{a}_r Z_0 \frac{|I_0|^2}{8\pi^2 r^2} \left[\frac{\cos\left(\frac{kl}{2}\cos\theta\right) - \cos\left(\frac{kl}{2}\right)}{\sin\theta} \right]^2 \tag{3.3}$$

To calculate the total radiated power, one needs to integrate the average Poynting vector over a sphere with the radius of r, which is given in 3.4.

$$P_{rad} = \oiint \boldsymbol{W_{av}} \cdot d\boldsymbol{S} = \int_0^{2\pi} d\phi \int_0^\pi \hat{a}_r W_{av} \cdot \hat{a}_r r^2 \sin\theta d\theta$$

$$= Z_0 \frac{|I_0|^2}{4\pi} \int_0^\pi \frac{[\cos\left(\frac{kl}{2}\cos\theta\right) - \cos(\frac{kl}{2})]^2}{\sin\theta} d\theta$$

$$\tag{3.4}$$

For the half-wavelength dipole case, the total radiated power would be:

$$P_{rad} = Z_0 \frac{|I_0|^2}{4\pi} \int_0^\pi \frac{\left[\cos\left(\frac{\pi}{2}\cos\theta\right)\right]^2}{\sin\theta} d\theta \tag{3.5}$$

Taking the general power concept, $P_{rad} = 0.5|I_0|^2 R_{rad}$, one can define the radiation resistance of a half-wavelength dipole using 3.6. The integration function is on θ, and over the range from 0 to π, which gives the value of 1.2188, therefore the radiation resistance of a half-wavelength dipole is about 73 Ω.

$$R_{rad} = \frac{Z_0}{2\pi} \int_0^\pi \frac{\left[\cos\left(\frac{\pi}{2}\cos\theta\right)\right]^2}{\sin\theta} d\theta = 60 \times 1.2188 = 73.128 \ \Omega \qquad (3.6)$$

Besides the radiation resistance, due to the wire resistance of the dipole arms, ohmic loss resistance also exists in a dipole, and together with the radiation resistance determine the dipole radiation efficiency. The ohmic loss resistance can be expressed as 3.7.

$$R_{Ohmic} = \sqrt{\frac{\pi f \mu}{\sigma}} \cdot \frac{l}{2\pi a} \qquad (3.7)$$

Where f is the dipole resonating frequency, μ is the magnetic permeability, σ is the conductivity of the metal, l is the dipole length in total, a is dipole arm radius.

The radiation efficiency - η, is defined as 3.8. Usually, in the low-frequency range (<1 GHz), the ohmic loss of the have-wavelength dipole is only 2-3 ohms, therefore its radiation efficiency can be over 95%.

$$\eta = \frac{R_{rad}}{R_{rad}+R_{Ohmic}} \qquad (3.8)$$

One important parameter of the antenna is the directivity, as it is a measure to evaluate the directional radiation of the antenna. It is defined as the ratio of the real antenna's maximum radiation intensity over the ideal isotropic antenna radiation intensity. The radiation intensity is defined as the radiated power out of the unit spherical angle. For the half-wavelength dipole antenna, its radiation intensity can be defined as 3.9, which only has a theta dependency, and would show uniform distribution along the phi direction. Plotting the normalized result of 3.9 along theta, one can obtain the normalized 2D radiation pattern of the half-wavelength dipole, which is shown in Figure 3.3. It shows the maximum radiation intensity is at theta = 90-degree, and the 3-dB beamwidth is 78°. The 3D radiation pattern is shown in Figure 3.4.

$$U = r^2 W_{av} = \frac{|I_0|^2}{8\pi^2} Z_0 \left[\frac{\cos\left(\frac{\pi}{2}\cos\theta\right)}{\sin\theta} \right]^2 \qquad (3.9)$$
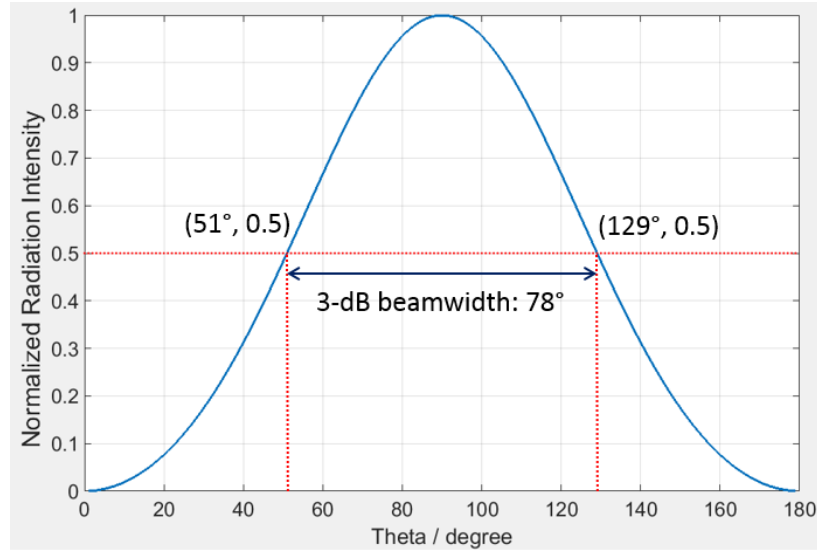
Figure 3.3. The half-wavelength dipole 2D radiation pattern.
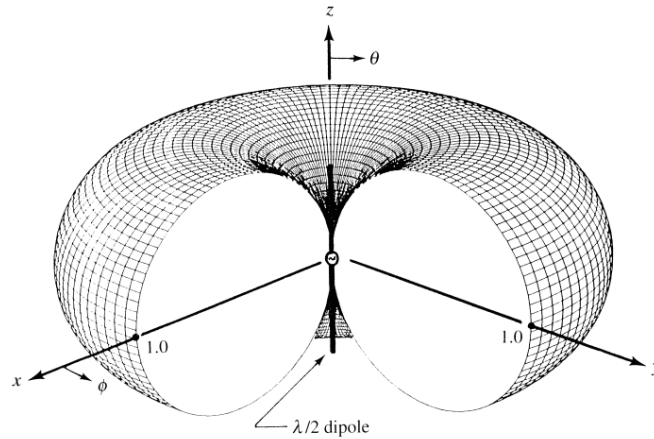
Figure 3.4. The half-wavelength dipole 3D radiation pattern [35].

The directivity can be defined as 3.10, the half-wavelength dipole has a directivity of 2.15 dBi, where dBi means dB value refers to the isotropic radiator.

$$D = \frac{U_{max}}{\frac{P_{rad}}{4\pi}} = \frac{4\pi U}{P_{rad}}\Big|_{\theta=90°} = \frac{Z_0}{\pi R_{rad}} = \frac{120}{73.128} = 1.641 = 2.15 \, dBi \qquad (3.10)$$

3.3 Dipole and the feed line realization on FR408

Antenna input impedance:
$$Z_{in} = f(L, W, L_{ov})$$
L: Dipole arm length.
W: Dipole arm width.
L_{ov}: Dipole two arm overlap length.
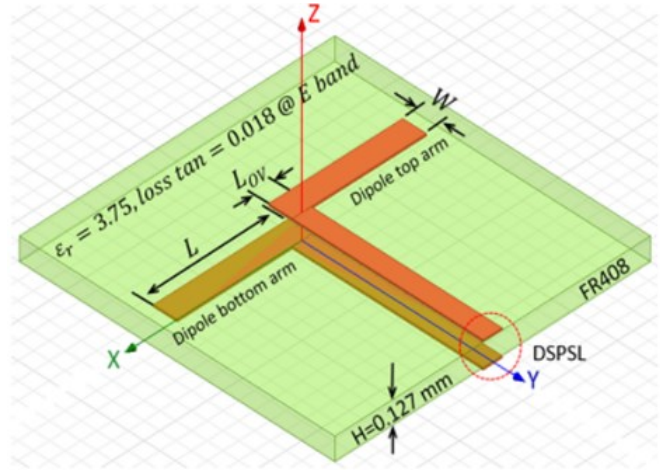
Figure 3.5. The realized 73 GHz dipole antenna structure.

For the 73 GHz dipole antenna design in this dissertation, Isola® FR408 is used as the substrate for fabrication, Figure 3.1 shows the substrate properties, and the realized dipole structure is shown in Figure 3.5. One dipole arm is placed on the top layer and the other arm on the bottom layer of the copper (Cu)-clad laminate. Two arms have an overlap area, which determines the dipole antenna input impedance together with the dipole arm width and length. Here, the dipole arm length, L = 0.85 mm, the width, W = 0.12 mm, and the overlap area, L_{OV} = 0.12 mm, which will make the input impedance, Z_{in} = 105 Ω [33], this was determined using ANSYS HFSS.

Unlike the patch antenna, the dipole needs a differential and balanced feeding, and double-sided parallel strip-line (DSPSL) is utilized to realize it. The structure and field distribution are shown in Figure 3.6. The DSPSL is formed by two vertical parallel strip-lines with equal width. Since the DSPSL transmits a differential signal, the center plane between the top and bottom lines can be treated as a virtual ground (0V), its characteristic impedance is twice

that of the microstrip line with the same line width and half of the substrate thickness. The width is kept as 0.12 mm to make the characteristic impedance of the DSPSL equal to the dipole antenna input impedance, which is 105 Ω.
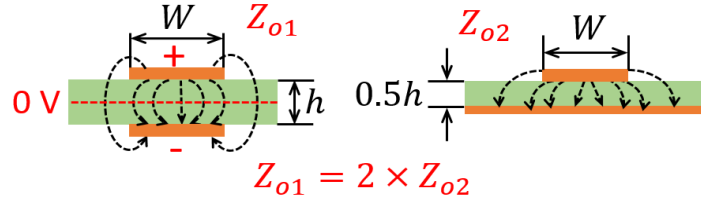
Figure 3.6. The structure of double-sided parallel strip line(DSPSL) and illustration of the field distribution and characteristic impedance.

The DSPSL structure cannot be fed directly, and to be able to use the GSG probe to excite the antenna, a transition structure from conductor-backed coplanar waveguide (CBCPW) to microstrip (MS) line and to DSPSL is designed. The top view of the transition and the corresponding sizes are shown in Figure 3.7, whose structure can be divided into 4 parts: (1) CBCPW for probe access, (2) CPW to MS transition, (3) MS and (4) MS to DSPSL transition. Based on the work in [36], a 50 Ω CBCPW line, the center signal line width W_1= 0.088 mm, gap width $S = 0.025$ mm, the top ground width $W_{g1} = 0.40$ mm, and the top ground length is L_{g1}. The CBCPW to MS transition area length $L = 0.10$ mm, the bottom layer rectangular ground length $L_{g2} = L_{g1} + L$ mm, the bottom layer rectangular ground width $W_{g2} = 2.00$ mm. The MS signal line width $W_2 = 0.26$ mm and trapezoidal ground length $L_{g3} = 1.70$ mm, which is chosen based on ANSYS HFSS simulation, and results in the characteristic impedance of MS line to be 50 Ω and DSPSL to be 63 Ω. The field conversion illustration in each transmission line is shown in Figure 3.8, where the whole transition structure from CBCPW to DSPSL is a balun, which converts the unbalanced field distribution in CBCPW to be balanced in DSPSL with low

reflection and wide bandwidth. To verify the transition structure performance, a back-to-back (B2B) CBCPW to DSPSL transition structure was realized, where the center DSPSL length is 1.58 mm. The top ground length, L_{g1} is varied from 0.60 mm, 0.80 mm and 0.90 mm, and Figure 3.9 shows the B2B transition structure and the corresponding GSG probe with 0.10 mm pitch, which utilized to feed the signal.

W_1	0.088 mm
S	0.025 mm
W_{g1}	0.40 mm
L_{g1}	0.90 mm
L	0.10 mm
W_{g2}	2.0 mm
L_{g2}	1.0 mm
W_2	0.26 mm
L_{g3}	1.70 mm
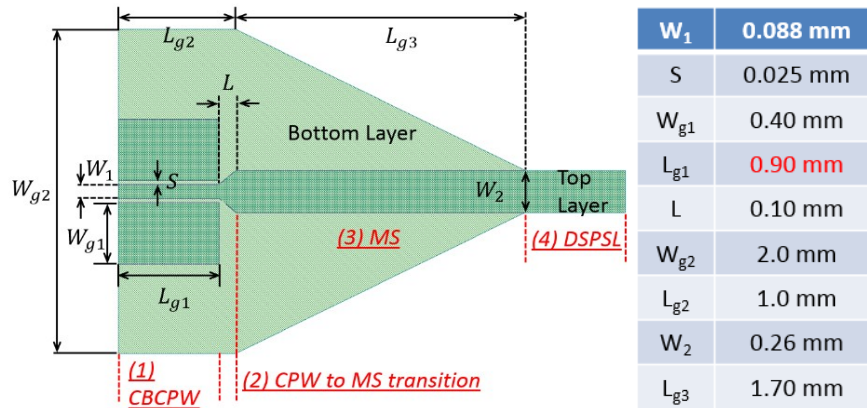
Figure 3.7. The structure of CBCPW to DSPSL transition [36].
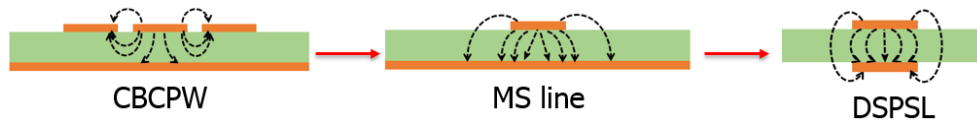
Figure 3.8. The field conversion in the transition structure.

(a)   (b)
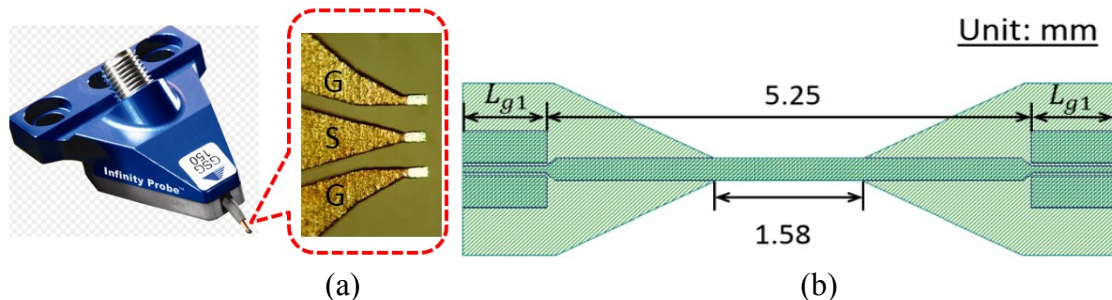
Figure 3.9. (a) The illustration of the GSG probe with 0.1 um pitch; (b) Top view of the B2B structure of the CBCPW to DSPSL transition.

40
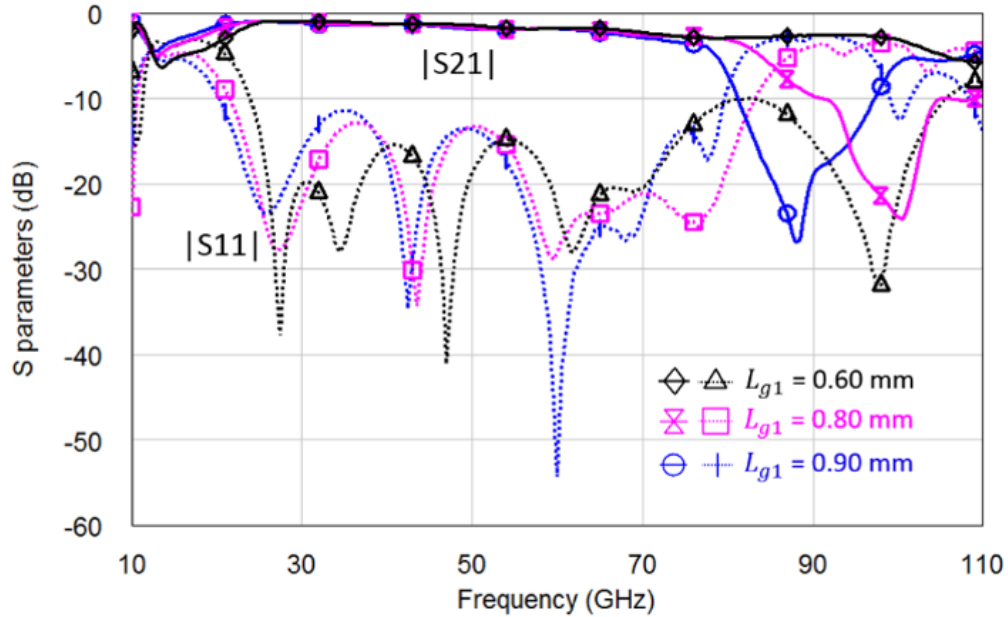
Figure 3.10. The simulated insertion and return loss of the B2B CBCPW to DSPSL transition structure.

Figure. 3.10 shows the simulated |S21| and |S11| curves of the B2B structure in Figure 3.9 with different L_{g1}. There is a band-stop frequency range on the |S21| curve, and it looks like a "valley". As L_{g1} increases, the corresponding frequency of the "valley" moves down. For L_{g1} = 0.90 mm, the "valley" frequency is 88.2 GHz, for L_{g1} = 0.80 mm, the "valley" frequency moves to 100.5 GHz, and for L_{g1} = 0.60 mm, the "valley" frequency is expected to be higher than 110 GHz. The estimated frequency range of the transition using L_{g1} = 0.60 mm is from 24 GHz to 105 GHz and has a relatively flat and low insertion loss, which is suitable for the 73 GHz application. The reason behind the band-stop range is the patch antenna mode excitation on CBCPW top floating ground pad, which is verified using ANSYS HFSS and shown in Figure 3.11, where L_{g1} = 0.90 mm as an example. To simulate the situation where the GSG probe launches on the CBCPW pads, a special excitation setup is developed (Figure 3.11 (b)), where a

50 Ω lumped port excites the center signal line of the CPCPW, and its width, W_1= 0.06 mm, and the height, H_1= 0.01 mm. The two top floating ground pads are connected using the PEC boundary, as illustrated in Figure 3.11 (b), the height, H_2= 0.07 mm, the width, W_2= 0.06 mm, and the total width, W_3= 0.32 mm, which is for the simulation of 0.10 mm GSG probe pitch. The lumped port integration line is in the vertical direction and points from the CBCPW center signal line surface to the PEC boundary.

From Figure 3.11 (a), the patch antenna mode is excited on the rectangular top floating ground pad at 80 GHz, because 0.9 mm is nearly half wavelength of 80 GHz on 0.127 mm FR408 material, therefore the signal around 80 GHz will be radiated out through the CBCPW top floating ground pad, and cause the band-stop range on the |S21| curve. Figure 3.12 shows the ANSYS HFSS simulation and measurement results of the structure in Figure 3.11. The simulated and measured curves are matched in general. One method to avoid the patch antenna mode excitation on the top ground pad is by adding vias and making a connection with the bottom ground. However, due to the process limitation, adding vias is not available. The other simple and convenient solution is changing the size of the top ground pad, which can help the CBCPW to DSPSL transition structure move the band-stop range from the working frequency range.

(a)   (b)
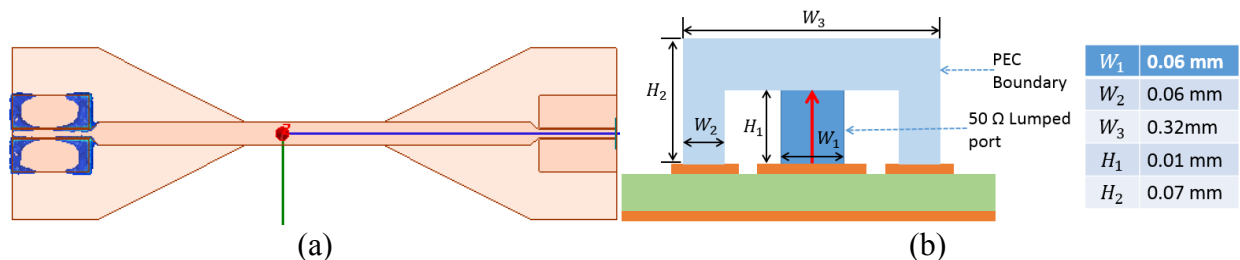
Figure 3.11. Illustration of the patch antenna mode excitation in the CBCPW to DSPSL transition: (a) The patch antenna mode on the CBCPW top ground pad; (b) The excitation port setup in ANSYS HFSS.
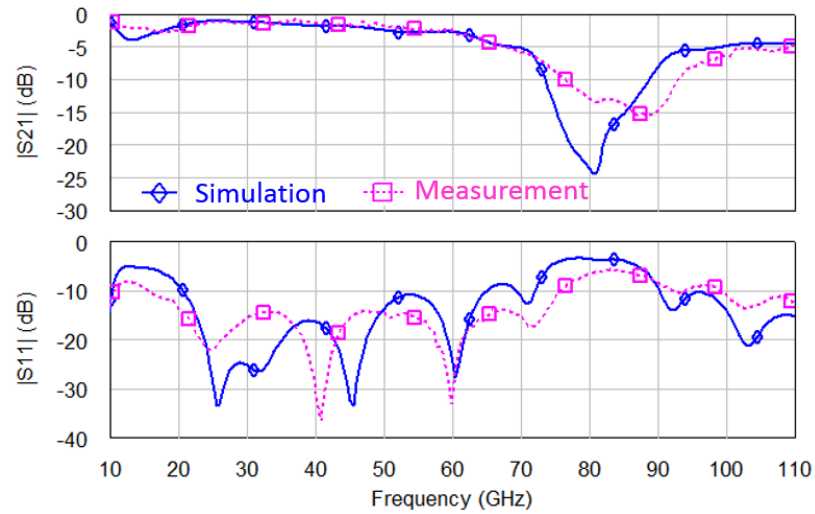
Figure 3.12. The simulated and measured insertion and return loss of the B2B CBCPW to DSPSL transition structure, with L_{g1}= 0.90 mm.
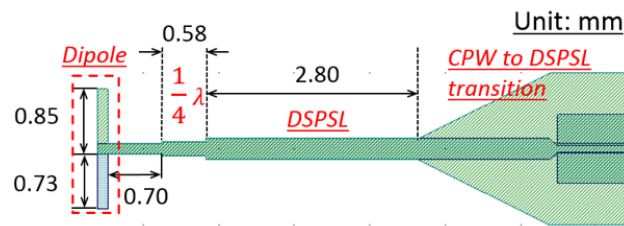
Figure 3.13. The structure of the dipole antenna with the CBCPW to DSPSL transition structure.

In order to utilize the transition structure in the dipole antenna, a quarter-wavelength transformer was added between the transition structure and the dipole, to transform the 63 Ω characteristic impedance of DSPSL to the 105 Ω dipole input impedance. Figure 3.14 shows the simulated and measured input return loss results of the single dipole antenna. The resonance frequency for the measurement result shifts by 7 GHz from 74 GHz to 67 GHz, and the bandwidth expands at the low-frequency end. This is caused by substrate permittivity variation or over-etching in fabrication. In order to measure the antenna on the Cascade probe station, the sample was placed on a 6.25 mm thick Rohacell® foam material with ε_r=1.093, loss tangent =

43

0.0155 at 26.5 GHz. However, the actual 10 dB bandwidth is still from 56 to 79 GHz, which can

cover the frequency range desired for antenna measurements.
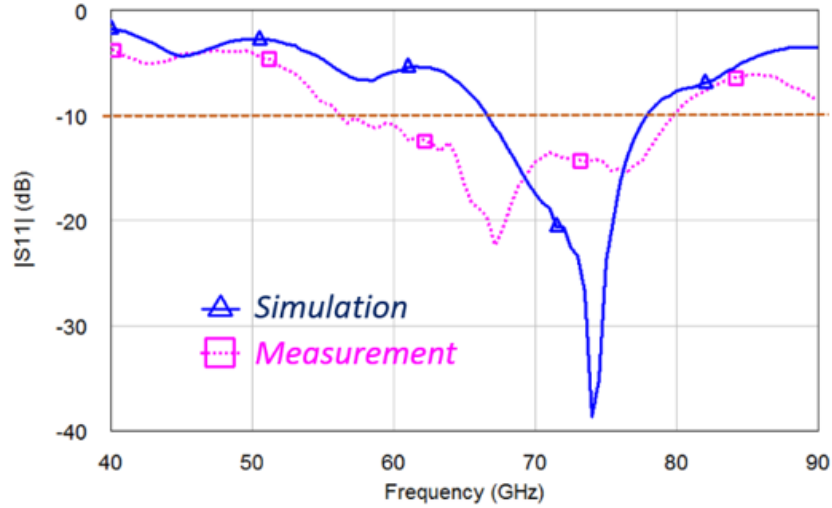
Figure 3.14. A single dipole antenna input return loss results.

3.4 Dipole OAM-UCA design

3.4.1   Generating OAM mode 1 and 3 using dipole UCAs [33]:

One 8 - element dipole array is designed to generate an OAM mode 1 radio beam, which

is shown in Figure 3.15 (a). The dipole arm length and width are 0.85 mm and 0.10 mm,

respectively. A modification to the dipole dimensions achieves the impedance match to

approximately 63 Ω. Three T-junction networks are used to properly divide the signals. A strong

effort was made to achieve symmetry in the structure. Each element is spaced approximately $\lambda/2$

away from one another and this amounts to a radius from the center feed structure of 0.8 λ_0. A

45° phase difference between elements is achieved by orienting the dipole to point in opposite

directions and adding different lengths of feed lines.

A second 12 - element dipole array was designed to realize an OAM mode -3 radio beam, which is shown in Figure 3.15 (b). The dipole arm length is 0.85 mm, and the width is 0.12 mm, the feed linewidth is 0.12 mm with an input impedance for this kind of dipole of 105 Ω. A 90° phase difference between elements is realized using the same method in the 8 − element dipole array above.

The transition structure shown in Figure 3.7 is also used here to feed the two UCAs. One should note that the -1 and -3 OAM mode can be easily obtained by mirroring the structure of the +1 and +3 OAM mode antenna arrays.

The UCAs were fabricated in the UT Dallas cleanroom where photolithography steps have been used to etch 0.012 mm of Cu to define the dipoles. Backside alignment is performed to etch the second half of the dipole metallization.

The antenna arrays' input return loss was simulated using AWR AXIEM and the radiation patterns were simulated using ANSYS HFSS. Agilent's PNA (E8361A) and Oleson Microwave Labs' OML module extenders were used to measure the input return loss up to 110 GHz. The antenna array was placed inside an anechoic chamber and a far-field scan was taken to capture the normalized radiation pattern, where normalized radiation patterns were taken.

A. Input Return Loss

The input return loss was measured on a Cascade® probe station using a load-reflect-reflect-match (LRRM) calibration to bring the reference plane to the probe tips. A 100 μm pitch GSG probe was used to feed the array. The measurement results are shown in Figure 3.16, where the array was mounted on a 6.25 mm dense Rohacell® foam block. The presence of the ground

plane and the additional feed line length required to separate the probe feed increased the loss in the networks along with the 6-9 dB due to the T-junction splitters. The 8 − element UCA input return loss is approximately 7 dB at 73.5 GHz and the 12 − element UCA input return loss is about 10 dB at 73.5 GHz, which is reasonable for antenna measurements. It was determined that the CBCPW to MS line transition was sensitive to CPW length and deteriorated the |S11| curve.

(a)
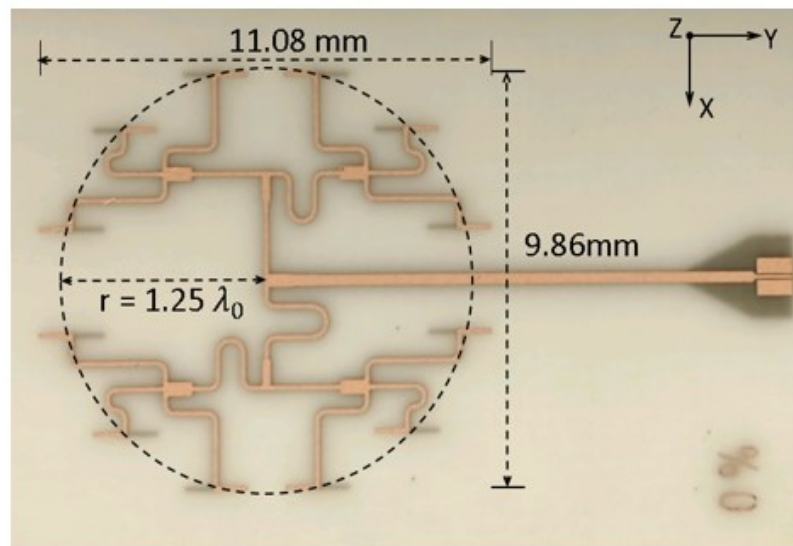
(b)

Figure 3.15. The 2 realized dipole UCA with feed network: (a) 8-dipole UCA for OAM mode 1; (b) 12-dipole UCA for OAM mode -3.

B. Radiation Pattern and Phase Distribution

Antenna arrays were mounted onto the antenna under test (AUT) probe platform, which is built using 10 layers of Rohacell® foam material (thickness = 62.5 mm in total). The same GSG probe for |S11| measurement was used to feed the array. Figure 3.17 shows the HFSS simulation and measurement results of radiation pattern cuts ($\phi = 0°$ and $90°$) for each array, and Figure 3.18 shows the chamber measurement setup for radiation pattern measurement. One of the features of the higher-order OAM mode is the expansion of the center null in the radiation pattern. The simulation and measurement radiation patterns are in good agreement, except for a few differences due to variations in fabrication and the presence of the AUT stand. The measurement center null is − 10 dB for the 8 − dipole UCA and − 8 dB for the 12 − element UCA.

The measured results of the designed antenna arrays can generate OAM mode 1 and 3. The OAM modes are defined by a null in the amplitude at the center of the beam (Figure 3.17) and a helical phase front. The null associated with mode 3 is larger than that of mode 1, although the additional elements for mode 3 distort the overall radiation pattern. Figure 3.19 shows the ANSYS HFSS simulated results for the phase distribution for each array. The phase of mode 3 is described by three rotational spins while mode 1 has one rotational spin. Figure 3.20 shows the chamber set up for phase distribution measurement using a Southwest Microwave® connector for easier setup.

(a)   (b)
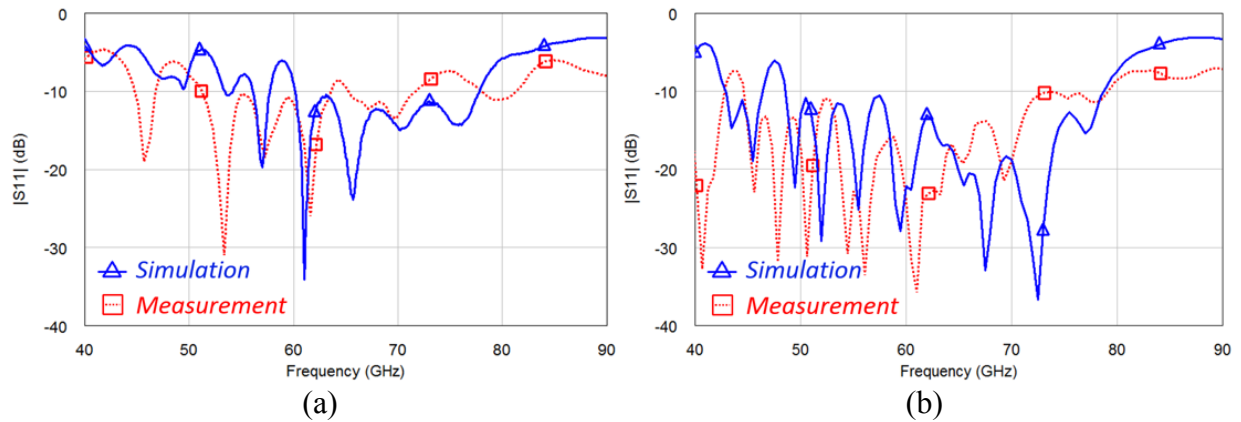
Figure 3.16. Simulation and measurement input return loss for the two dipole arrays: (a) 8 – element array for OAM mode 1; (b) 12 – element array for OAM mode 3.
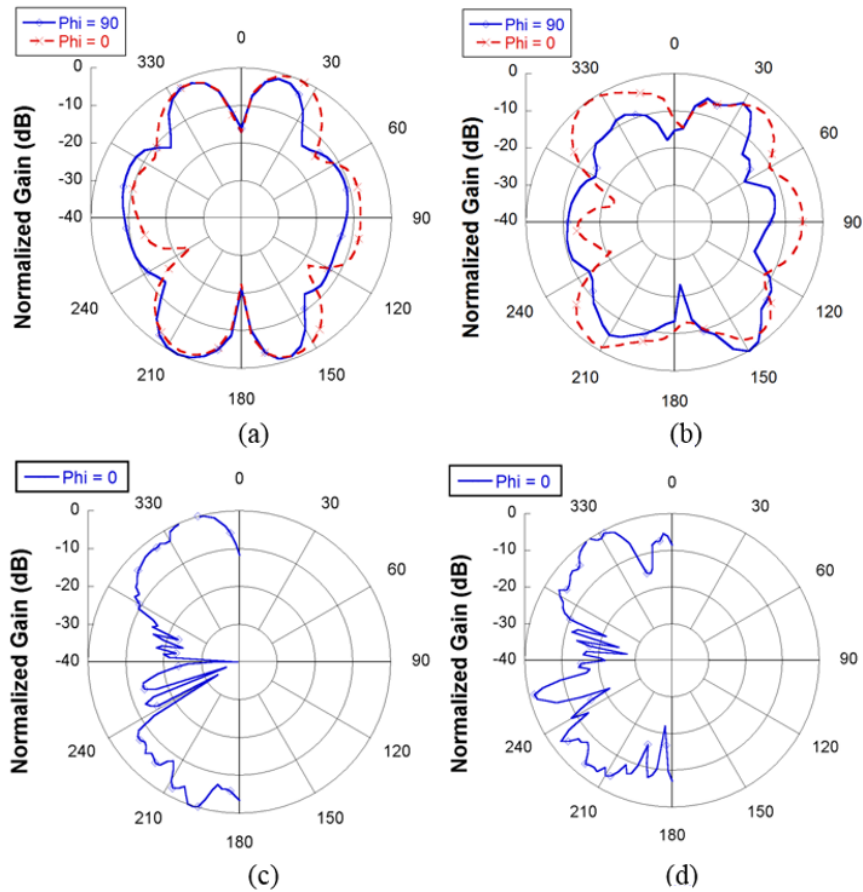
Figure 3.17. Dipole array radiation cuts ($\phi = 0°$ and $90°$): (a) Simulated 8-dipole OAM mode 1; (b) Simulated 12-dipole OAM mode 3; (c) Measured 8-dipole OAM mode 1 ($\phi = 0°$); (d) Measurement result of 12-dipole for OAM mode 3 radiation cut ($\phi = 0°$).
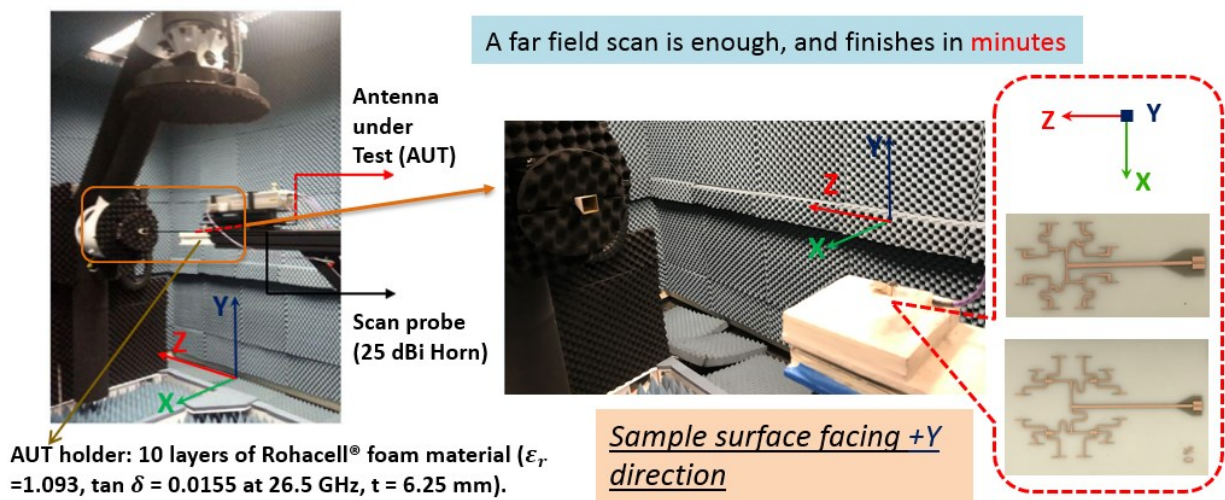
Figure 3.0.18. Dipole array radiation cuts ($\phi = 0°$ and $90°$) chamber measurement setup.
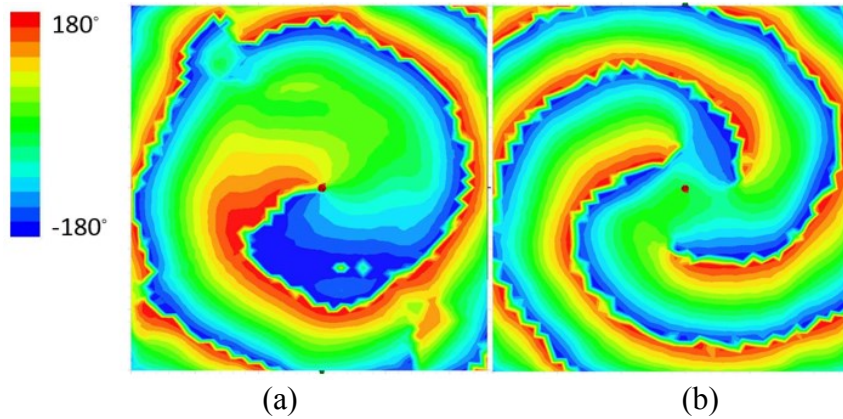
Figure 3.19. Two dipole array phase distribution results: (a) 8-dipole for OAM mode 1; (b) 12-dipole for OAM mode 3.
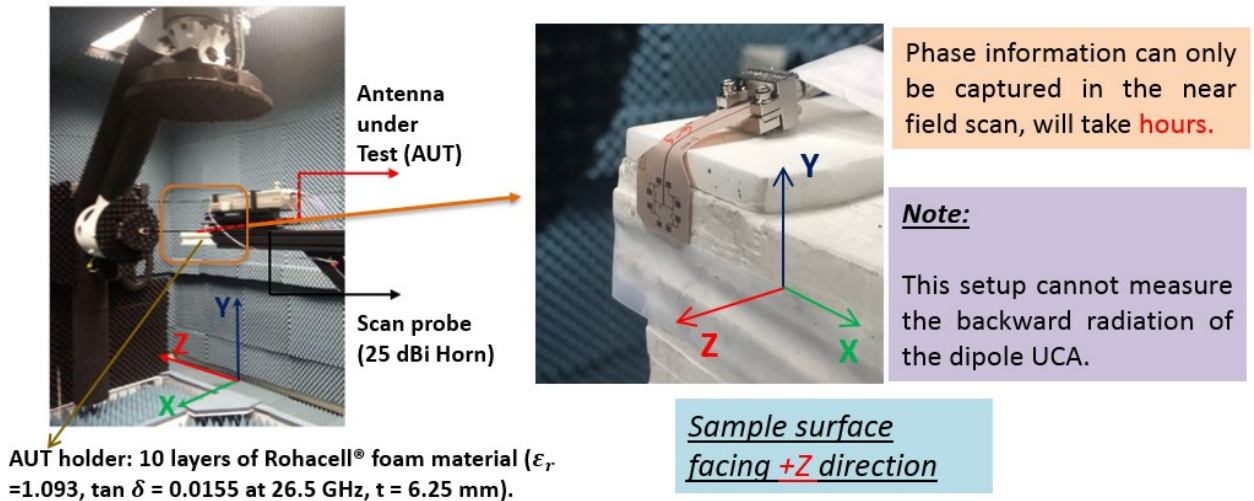
Figure 3.0.20. Dipole UCA phase distribution chamber measurement setup.

C. Summary

73.5 GHz half-wavelength dipole antenna arrays have been used to realize two OAM modes on a flexible FR408 substrate. The mode is captured due to the null measured at the center of the antenna array. Array sizes are reduced when using dipoles although the elements interact with each other due to their close proximity. This impacts the overall radiation pattern. Unlike

patch antennas demonstrated in the literature [25], the dipole will resonate in both the upper and lower hemisphere.

3.4.2 Generating OAM mode 1 using UCA with series and corporate feed [37]:

A. The corporate feed UCA

Based on the dipole antenna structure in Figure 3.5, a corporate feed UCA is generated using 4 dipoles, as shown in Figure 3.15 (a). The UCA's radius is 2.5 mm, which is approximately $0.6\lambda_0$ at 73 GHz. The spacing between each antenna element is 3.5 mm, which is roughly $0.9\lambda_0$ at 73 GHz. To be excited by a single source, a feed network with T-junction dividers has been designed. The phase shift is achieved using different lengths of the DSPSL and by rotating the orientation of the dipoles' arms accordingly. In Figure 3.21 (a), element 2 has a 90° phase shift from element 1. This is realized by the longer feed line of element 2, while elements 1 and 3 are fed using the same length feed line, but with dipole arms on opposite layers, generating a 180° phase shift. The array size is optimized using ANSYS HFSS to balance the amplitude and phase along with the radiation pattern of the array structure. Two T-junction networks are used to properly divide the input power.

B. The series feed UCA

The series feed UCA with a smaller radius as shown in Figure 3.21 (b). The radius of the array is 2.1 mm, and the spacing between each element is 3.0 mm (not considering the feed), which is roughly $0.75\lambda_0$ at 73 GHz. The width of the DSPSL feed line is still kept as 0.12 mm, and quarter-wave transformers are used at each branch with one single T-junction to realize the impedance match.

The benefits of using a series feed network include a smaller array area, less power dissipation, and lower interaction between the feed network and antenna elements, since there is no feed network in the center of the array. However, the trade-off is that it is harder to realize two series antenna elements that will have the same amplitude compared with the corporate array. Here, one should note that the -1 OAM mode can be easily obtained by mirroring the structure of the +1 OAM mode antenna arrays.

(a)

(b)

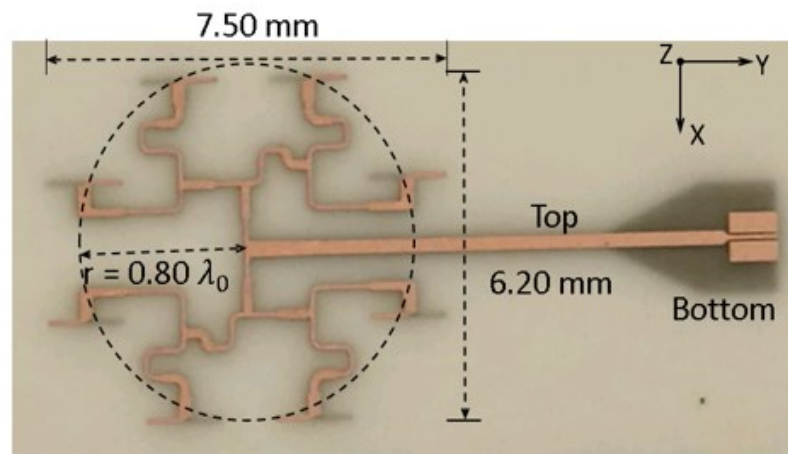Figure 3.21. 4-dipole UCA for OAM mode generation: (a). The corporate feed UCA; (b). The series feed UCA

C. Input match

The arrays were mounted on a 10-layer stack Rohacell® foam material. The simulated and measured results are shown in Figure 3.22 from 70 to 90 GHz. At 73 GHz, the corporate feed array input return loss is approximately 11 dB and the series feed array is also 11 dB. By modifying the relative permittivity to 3.5 and including the foam mount, the simulation agrees with the measurement. The corporate feed array's resonance is dampened and shifted by 4 GHz. This may be due to the influence of the feed lines and over-etching of Cu in fabrication.
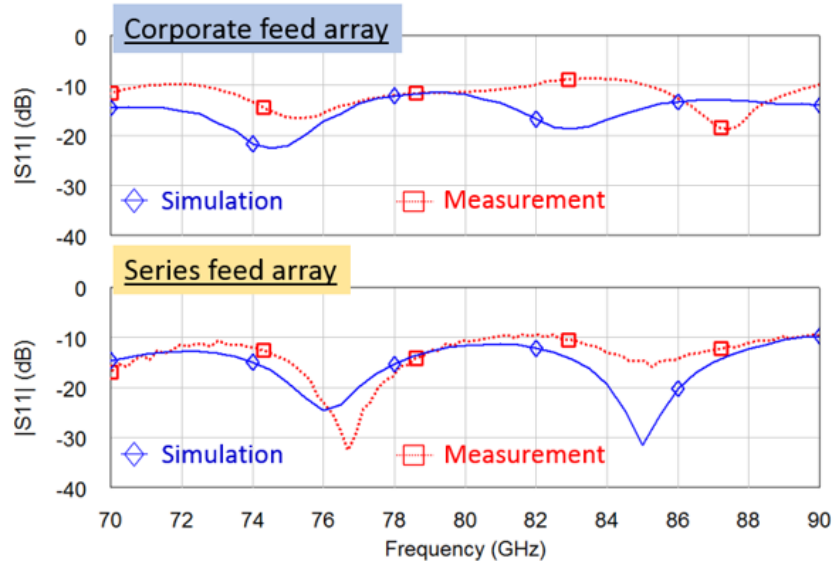
Figure 3.22. The simulated and measured input return loss for the two dipole UCAs.

D. Radiation pattern and phase distribution

The same GSG probe used for measuring |S11| was used to measure the two arrays' radiation performance. Figure 3.23 shows the HFSS simulation and measurement results of the radiation pattern cuts ($\phi = 0°$ and 90°) for each array. The simulated and measured radiation patterns are in good agreement, except for a few differences due to variations in fabrication and

the presence of the antenna under test (AUT) stand. The 4-dipole corporate feed array measured a center null of approximately − 15 dB in the $\phi = 0°$ and 90° cuts. The 4-dipole series feed array has a − 10 dB center null in the $\phi = 0°$ and 90° cuts, and the null locations agree well. The corporate feed array exhibits more ripples, which may be due to feedline interaction with the dipoles, and because of the larger array size. Figure 3.24 shows the simulated results for the phase distribution of each array, the results are taken from a plane 5 mm away from the array. The designed antenna UCAs can generate OAM mode of ±1.
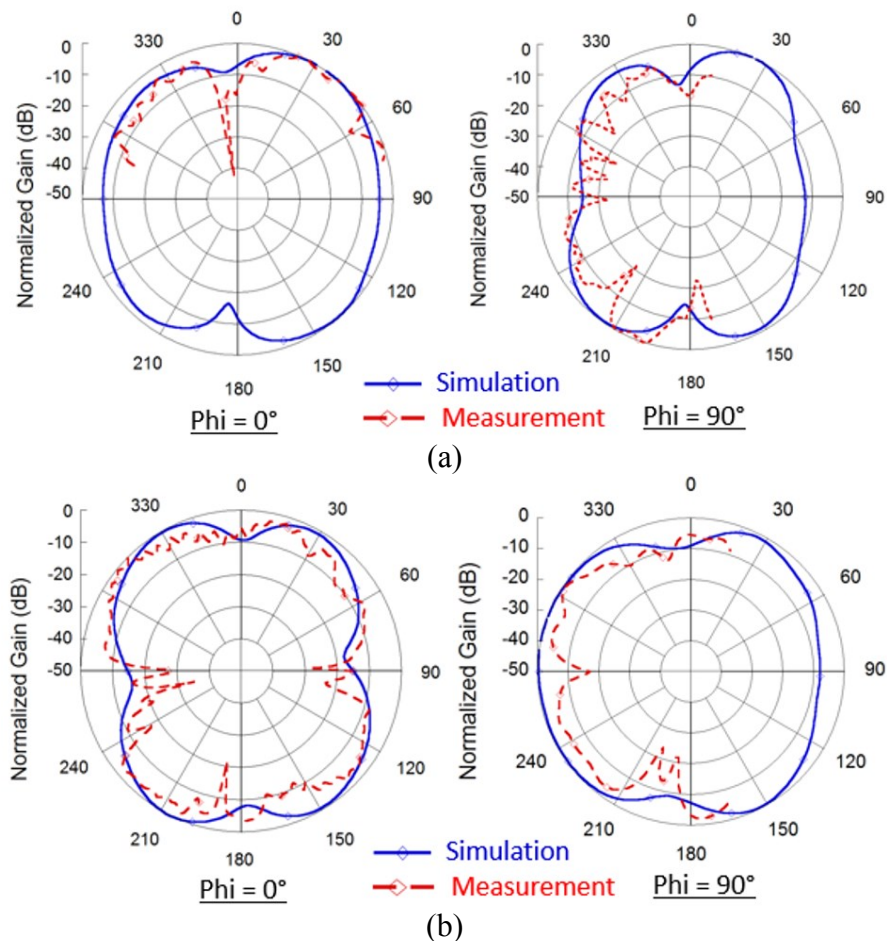
Figure 3.23. The simulation and measurement radiation cuts of the two arrays: (a) 4-dipole corporate feed UCA; (b) 4-dipole series feed UCA.

E. Summary

Two types of 73 GHz 4-dipole antenna arrays have been used to realize OAM modes ±1 at 73 GHz to demonstrate corporate and series feed networks. The mode is generated as evidenced by the null in the measured radiation patterns and the helical phase distributions. It is believed that using a series feed will reduce interactions between the antennas and distribution network without the need for a two-layer board.

(a)   (b)
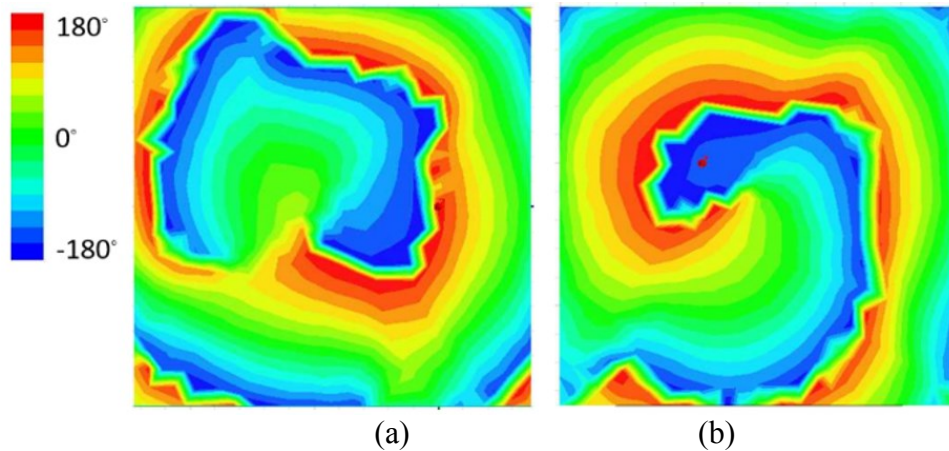
Figure 3.24. The simulated phase distribution of the two arrays: (a) Corporate feed array; (b) Series feed array.

3.5 Dipole OAM-UCA backward radiation elimination [38], [39]

As illustrated in the previous sections, the dipole has a large bandwidth and high radiation efficiency, which makes it suitable for wideband mm-wave communication such as E-band systems (71-76 GHz and 81-86 GHz). However, planar dipole UCAs will radiate in both the forward and backward directions, which will reduce the gain and power efficiency in the forward direction. The unwanted backward radiation may also cause electromagnetic compatibility (EMC) issues in the entire RF system. OAM based wireless communication mainly

55

works for the point to point (P2P) and line of sight (LOS) scenario, and hence only the forward radiation is typically utilized.

This section highlights a simple solution of adding a planar metallic reflector at the backside of the dipole OAM-UCA to remove the backward radiation and enhance the array gain in the forward direction. Starting from the OAM-UCA factor, and combining with image theory and MATLAB simulation, the correct OAM mode can be achieved in the UCA. To improve the performance of the dipole UCA, the principle of the dipole OAM-UCA with a planar reflector was included. The 8-dipole OAM-UCA used here is the one in Figure 3.15 (a), the planar reflector is realized by removing the top metal of a double-sided Rogers RT/duroid 5880 board with relative permittivity of 2.2 and loss tangent of 0.0009. Figure 3.25 shows the structure of the 8-dipole UCA with the planar reflector.

A. The design theory

The OAM mode generated by a dipole UCA radiates in both hemispheres and produces forward and backward radiation in the opposite directions. As an example, the 8-element dipole UCA produces a clockwise or OAM mode +1, for the forward radiation in simulation, and the backward radiation produces a counter-clockwise or OAM mode -1 (Figure 3.26). [40, 41] indicated that the reflected radio beam will be the opposite OAM mode to the incident wave, and by adding a reflector at the backside of the dipole UCA, can convert the backward OAM -1 mode to +1 and reflect it back to the forward direction. Based on image theory, a single element gain can be increased by placing a reflector 0.25λ away from the antenna [42]. Another consideration for planar antenna reflector design is the reflector material should not possess a relatively high permittivity, otherwise, the electromagnetic field will be held between the planar

antenna and ground and will not radiate. Based on these two considerations, RT/duroid 5880 was chosen as the reflector board, since it has relatively low and stable permittivity. The dielectric thickness should be 0.64 mm, which is approximately 0.25λ at 73 GHz. Taking the bottom copper (Cu) clad thickness into consideration, the whole thickness should be 0.64 + 0.017 = 0.657 mm.

The 0.64 mm thickness RT/duroid 5880 reflector was fabricated using the LPFK® ProtoMat S62 milling machine. Standard RT/duroid 5880 board thickness is 0.8 mm with 0.017 mm top and bottom cladded copper. The substrate height was reduced to 0.64 mm by carefully adjusting an end mill depth to remove the top metal in addition to 0.147 mm of the dielectric. The entire structure of the dipole array with reflector is illustrated in Figure 3.27. The antenna array is attached to the reflector using double-sided tape.
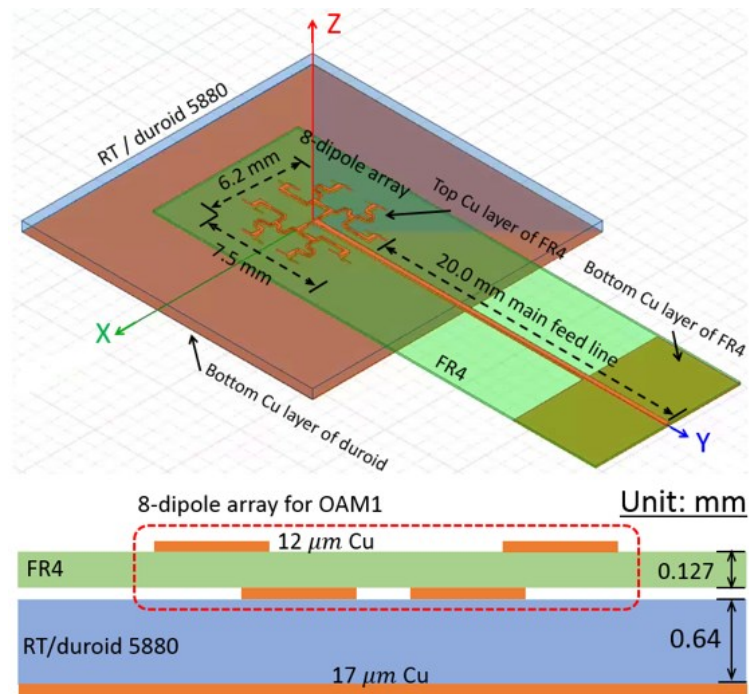
Figure 3.25. Isometric view and cross-section of proposed dipole array with reflector.
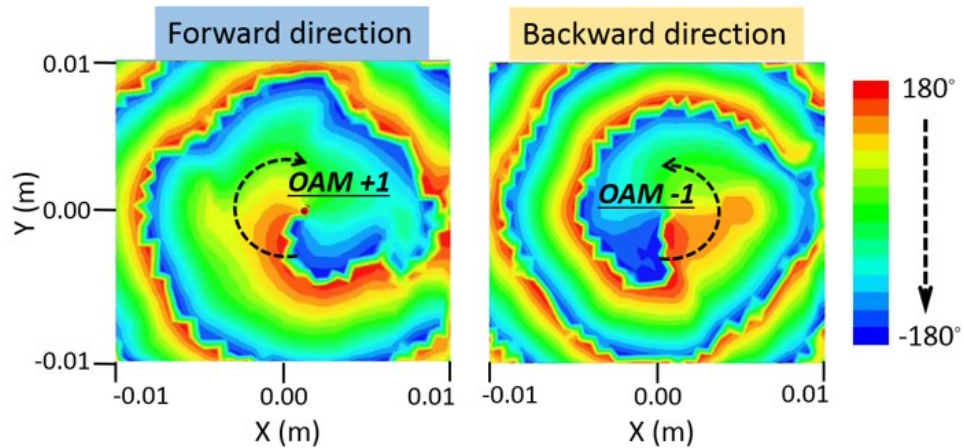
Figure 3.26. The forward and backward phase distribution of the 8-element dipole array without the reflector.

B. Input return loss

The antenna arrays' input return loss (RL) and radiation patterns were simulated using ANSYS HFSS. Figure 3.28 shows the simulated return loss result for an individual patch, dipole and the arrays with and without the reflector. The single element simulation shows that the dipole has a wider bandwidth than the patch, where the RL of the array at 73 GHz is 30 dB. Over the frequency band, the RL is better than 15 dB for the arrays, but this is due to the loss tangent of the FR4 and the feed line length (20 mm). The feed line length is used to acquire phase information during the near-field scan, but contributes to the loss, and hence the UCA gain would be reduced. The ANSYS HFSS simulation with no loss tangent and no reflector indicates that the RL is 13 dB at 73 GHz. The reflector does shift the resonance of the single dipole lower, which should be considered when designing the UCA.
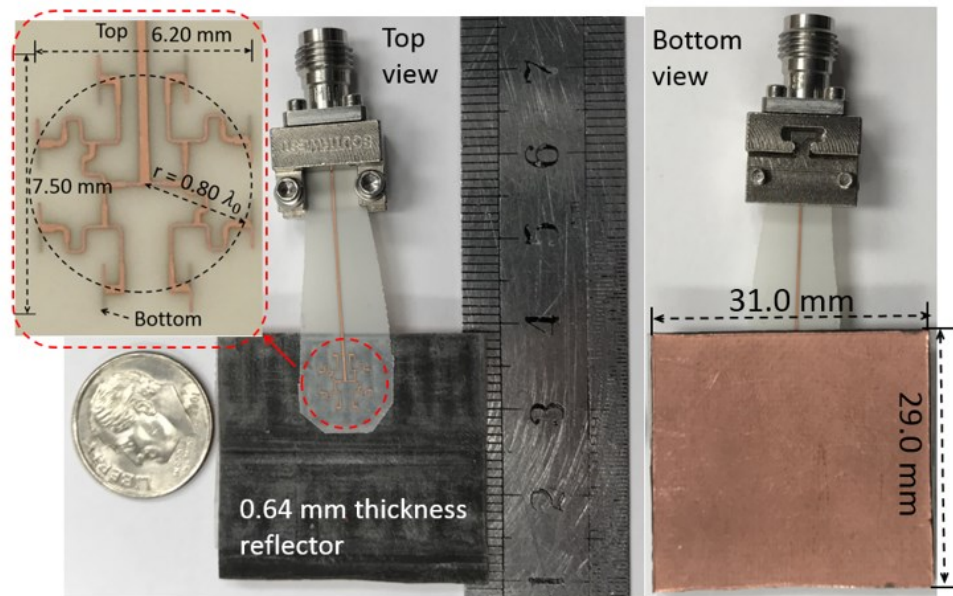
Figure 3.27. The fabricated dipole array with the attached reflector and end launch connector.
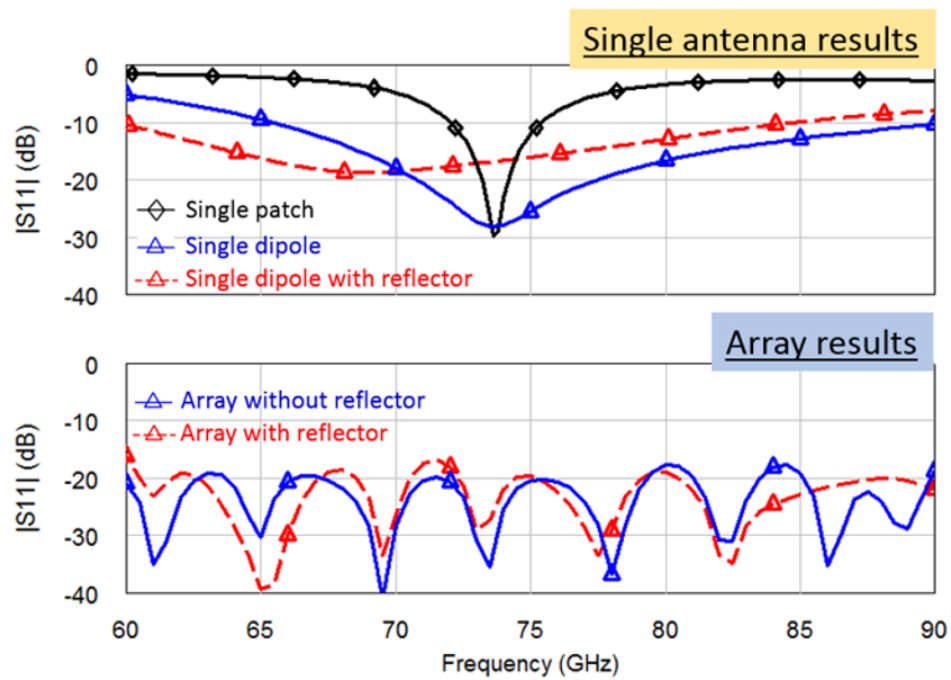
Figure 3.28. The simulated input return loss results of the single dipole, 8-element dipole array with and without the reflector.

C. Radiation pattern

The radiation patterns of the UCA with and without the reflector were taken over multiple frequencies from 68 to 75 GHz. Figure 3.29 shows the HFSS simulation and measurement results of the radiation pattern cuts ($\varphi=0°$) for each array at 73 GHz. One of the features of the higher-order OAM mode ($\pm l$) is the center null in the radiation pattern. The simulation and measurement radiation patterns are in good agreement, except for a few differences due to variations in fabrication and the presence of the AUT stand. The measurement center null is -10 dB for the UCAs with and without reflector, while the simulation results show the center null is better than -20 dB for both of the UCAs. The backside radiation is significantly reduced by adding the reflector.

Figure 3.30 shows the measured radiation pattern of the UCA with and without the reflector at 68 GHz and 75 GHz, respectively. The center nulls exist in both UCAs, which is a key property of non-zero OAM mode. The measured nulls for both arrays are not exactly in the center, which may be due to the sample surface not being parallel to the receiver horn of the scanner and the thickness variations of the reflector. This also may be due to not placing the sample directly in the center of the sphere for radiation pattern characterization.

At 73 GHz, the simulated UCAs in ANSYS HFSS have a gain of 5.2 dB for the UCA without the reflector, and 7.4 dB gain for the UCA with reflector, and the simulated efficiency is 73.3 % and 68.5 %, respectively. An additional 2.2 dB gain is achieved by adding the reflector, however, ideally, one would expect an extra 3 dB gain. This is mainly caused by the reflected power not only going to the forward direction to enhance the main lobe radiation, but also going to increase sidelobes. In Figure 3.29 (b), the simulated radiation pattern shows some radiation in

+/- 90° range. The chamber measured gain at 73 GHz is 1.62 dB for the UCA without the reflector, and 4.48 dB for the UCA with reflector. Compared to the simulated gain, the measured one was reduced by 2.9 – 3.6 dB, this is mainly caused by the existence of the 20 mm feedline in the sample for the gain measurement, which cannot be avoided and will introduce an extra 3 dB loss in power fed into the UCA, and hence the decrease in the measured gain is observed.

(a)   (b)
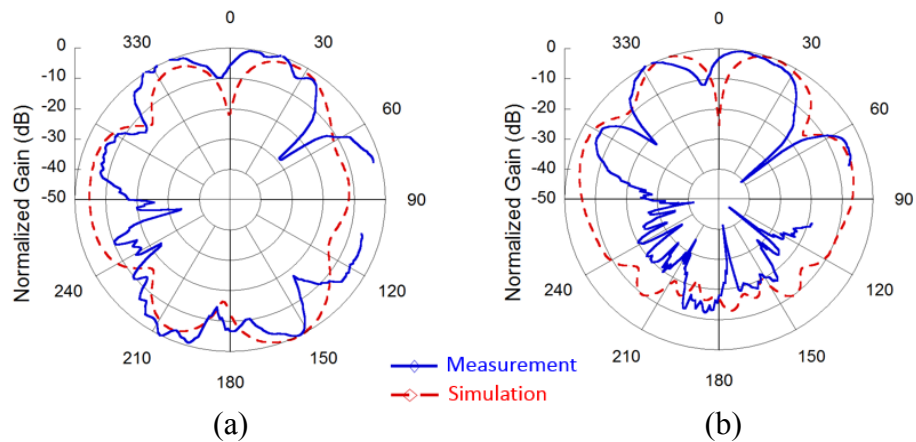
Figure 3.29. 73 GHz simulated and measured radiation pattern cut at Phi = 0 degree: (a) Array without reflector. (b) Array with reflector.

(a)   (b)
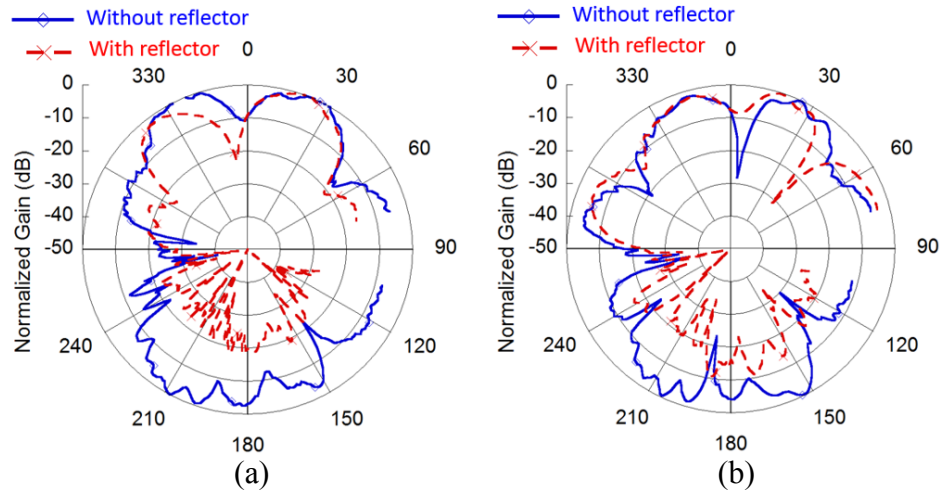
Figure 3.30. The measured radiation pattern comparison results between the array with and without reflector at Phi = 0 degree: (a) 68 GHz; (b) 75 GHz.
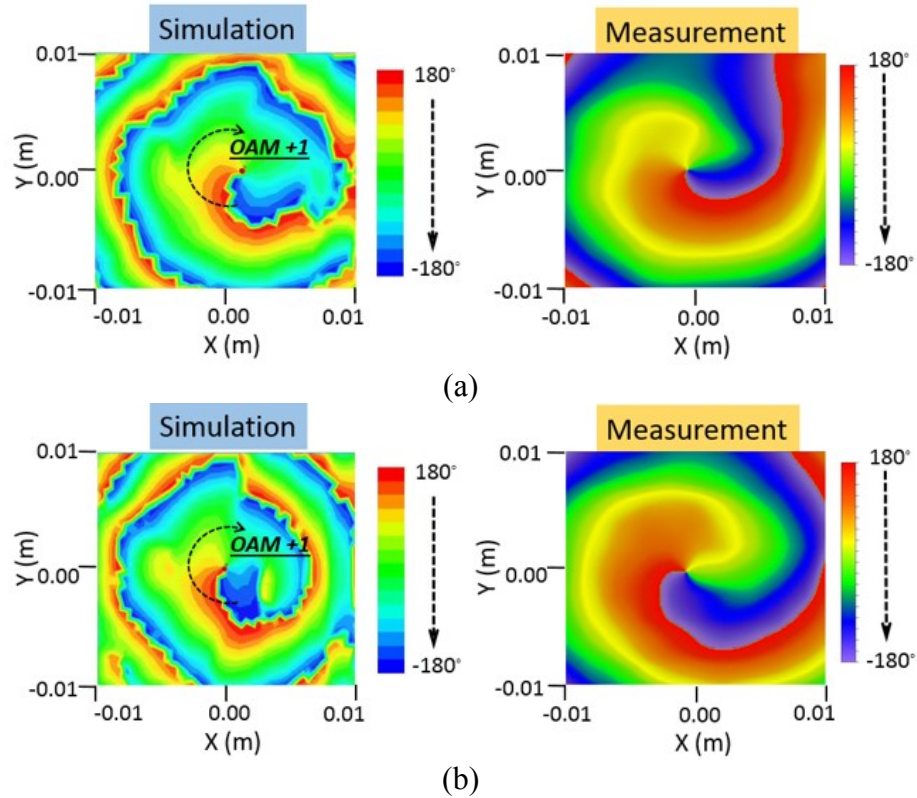
Figure 3.31. 73 GHz simulated and measured phase distribution: (a) Array without reflector. (b) Array with reflector.

D. Phase Distribution

The phase distribution is achieved by measuring the antenna with a 20 mm feed line as shown in Figure 3.20, the probe antenna should face in the direction of the AUT radiation plane in order to obtain the OAM twisted phase distribution. Figure 3.31 shows the simulated and measured results for the phase distribution of each UCA, where the results are taken from a plane 5 mm away from the array in simulation. In measurement, it is based on the fixed distance of the AUT with respect to the phi arm of the system. Both results with the reflector can generate OAM mode 1, as verified by the theory in section A. The reflector does not affect the OAM mode

phase. Figure 3.32 shows the measured phase distribution of the UCA with the reflector over a 6 GHz band.
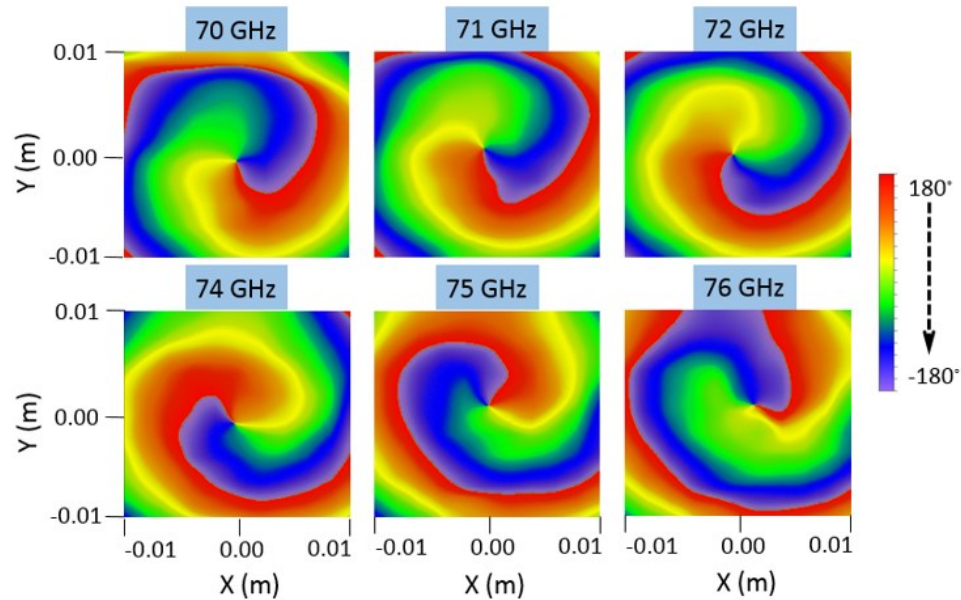
Figure 3.32. The measured phase distribution of the UCA with the reflector from 70 to 76 GHz.

E. Summary

A reflector has been included with an 8-element dipole UCA for generating OAM mode 1 at 73 GHz to increase the dipole array gain and remove the backside radiation. This method adds approximately 2.20 dB of gain to the OAM beam in simulation, and 2.86 dB in measurement, while not perturbing the phase distribution. The null in the radiation pattern has a shift in position. This is the first time that a backside reflector has been used in an OAM planar dipole UCA. The measured radiation patterns and phase distributions indicate the structure with dipole array and reflector can generate OAM mode 1 successfully in the upper E band (71 GHz to 76 GHz). The OAM mode will not be affected by the reflector although there is a shift in center frequency, efficiency and radiation pattern, which can be optimized in simulation. The

additional gain is critical for mm-wave designs where the free space path loss will impact the system budget. The measured gain of the UCA was achieved using the gain comparison method where the reference antenna was a standard horn antenna with a 10 dB gain. At 73 GHz, the measured gain with and without reflector are 1.62 dB and 4.48 dB.

3.6 OAM mode purity

To check the purity of the OAM mode 1 generated by the 8-dipole UCA, the OAM mode purity verification method, which is illustrated in chapter 2, is applied to the samples of the 8-dipole UCA with and without the planar reflector respectively. Figure 3.33 shows the simulation setup, simulation results and the purity verification result of the 8-dipole UCA without the planar reflector, the field plane (checking area) is 40 mm × 40 mm plane at 27 mm away from the UCA surface. The 27 mm spacing between the UCA plane to the field plane is making it satisfy the electromagnetically long antennas far-field condition [45], which is shown in 3.11, where D is the largest dimension of the UCA, which is 7.5 mm, and λ is the wavelength, which is 4.1 mm of 73 GHz, therefore it is about 27 mm.

$$d_F = \frac{2D^2}{\lambda} \tag{3.11}$$

The electrical field magnitude and phase information in that field plane were used here to verify the mode purity, as shown in Figure 3.33, 8-dipole UCA without the reflector gives a 60.45% mode purity, while the same sample with the planar reflector will give 65.63% mode purity, which is shown in Figure 3.34. Besides the gain enhancement, a 5% increase in OAM mode purity is also achieved by adding the planar reflector to the 8-dipole UCA.
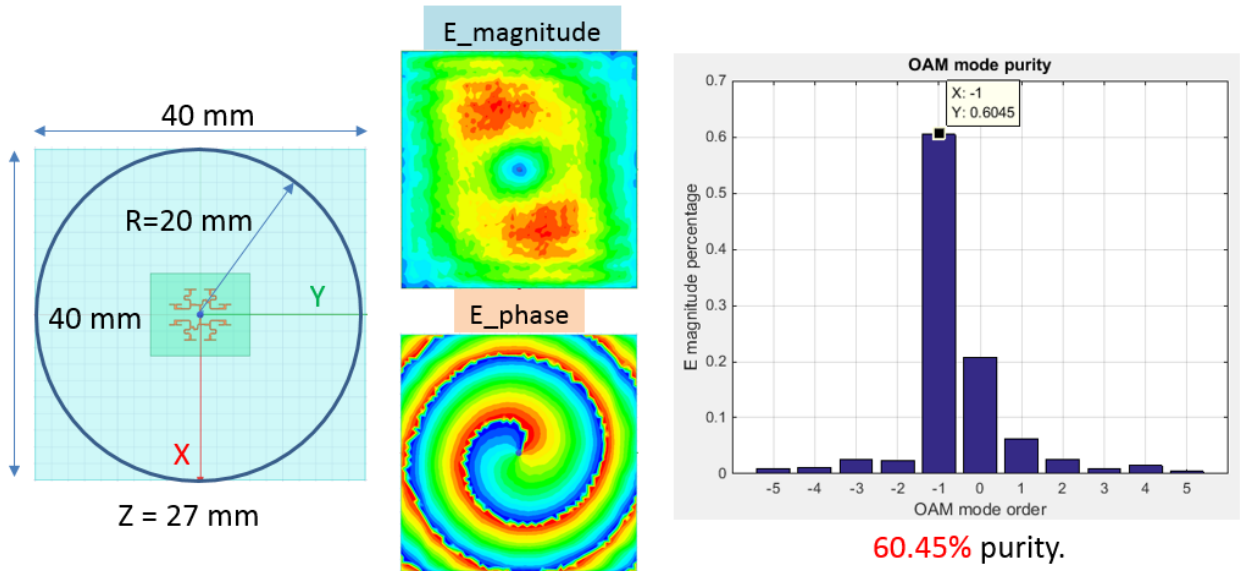
Figure 3.33. The simulated 8-dipole UCA without the reflector for OAM mode 1 purity checking result.
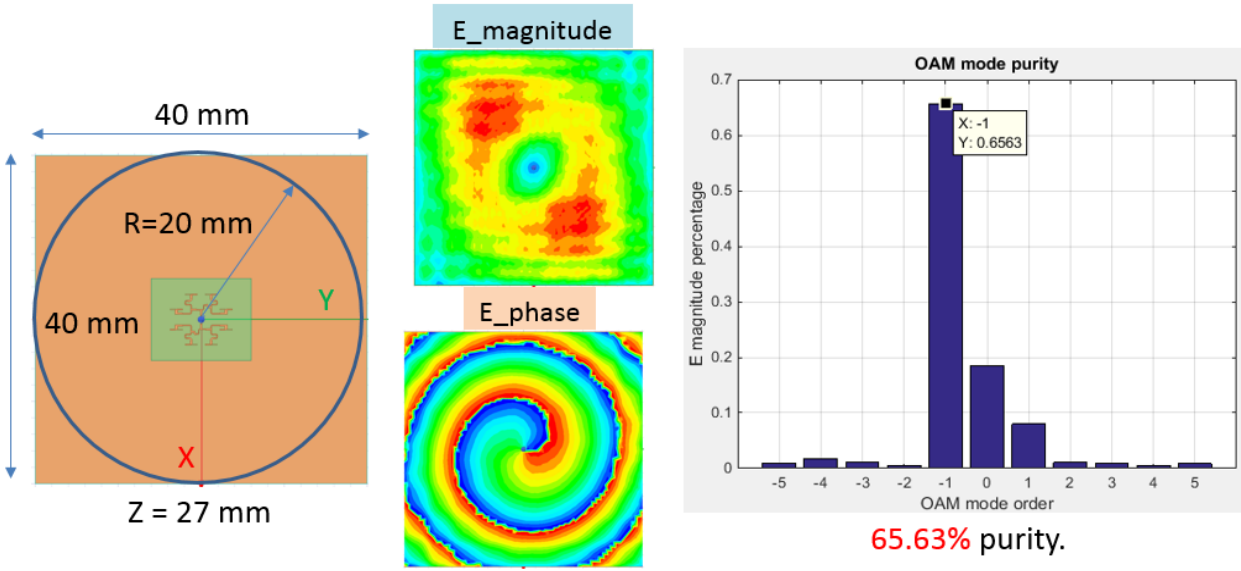
Figure 3.34. The simulated 8-dipole UCA with the reflector for OAM mode 1 purity checking result.

3.7 Summary

In this chapter, the dipole antenna theory was studied, and a new planar dipole antenna structure was proposed to realize the OAM-UCAs. The first section explained the purpose to use the dipole antenna to build the OAM-UCAs, and illustrated the substrate material used. The second section gave the theory of dipole radiation, which starts from the current distribution along the dipole arm, and to the far-field radiation pattern derivation. Section 3 gave the structure of the dipole antenna, the feed with transition structure and the different types of OAM-UCAs, the measured and simulated input return loss, radiation patterns and phase distribution were given, which illustrated that the correct OAM modes are generated by those UCAs. The fourth section gave a simple method to eliminate the dipole backward radiation by adding a planar reflector, which would make the UCA gain higher and keep the same OAM mode in the forward direction. The OAM mode purity verification method was applied to the ANSYS HFSS simulation results in the far-field condition, which showed a 5% mode purity increase by adding the reflector to the 8-dipole UCA.

CHAPTER 4

PATCH UCA FOR OAM MODE GENERATION

4.1 Introduction

As illustrated in the third chapter, the patch antenna performance suffers due to the substrate loss tangent, but it radiates in one direction and has higher gain than the dipole. The patch also is a good option for millimeter-wave (mm-wave) point-to-point communication. The cleanroom fabrication process for the microstrip patch UCA is also much simpler than that of the dipole. As indicated in Appendix D, compared with the dipole fabrication process, there is no backside alignment required or first layer protection for the patch, and only one mask is needed, therefore, the fabrication accuracy can be well-controlled. On the other hand, the improvement in substrate material properties enables us to have a stable and low loss option, which would mitigate the decrease in radiation efficiency of the patch caused by loss tangent. Figure 4.1 shows the properties of TerraGreen® substrate provided by Isola Group over frequency and temperature [43]. At room temperature, the loss tangent is 0.0055 at 60 GHz, 77 GHz, and 81 GHz, compared to FR408 (loss tangent = 0.018 @ E-band), this value is three times smaller.

TerraGreen® – Temperature Dependent Material Characteristics

Frequency	ε_r, tan(δ) @ 25°C	ε_r, tan(δ) @ 75°C	ε_r, tan(δ) @ 125°C	ε_r, tan(δ) @ 150°C
24 GHz	3.71 / 0.0060	3.71 / 0.0075	3.71 / 0.0085	3.71 / 0.0094
60 GHz	3.59 / 0.0055	3.59 / 0.0065	3.59 / 0.0070	3.59 / 0.0085
77 GHz	3.64 / 0.0055	3.58 / 0.0060	3.62 / 0.0070	3.72 / 0.0095
81 GHz	3.62 / 0.0055	3.62 / 0.0060	3.67 / 0.0085	3.62 / 0.0095
125 GHz	3.67 / 0.0030	3.68 / 0.0045	3.70 / 0.0060	3.70 / 0.0060

Figure 4.1. TerraGreen® substrate material temperature-dependent characteristics [43].

4.2 Microstrip patch antenna design theory

Microstrip patch antenna theory has been well studied, especially for the rectangular patch, and in this chapter, all of the patch OAM-UCAs are realized using it. Figure 4.2 illustrates the structure and field distribution. To analyze the patch antenna, there are two classical methods: transmission-line model and cavity model, where both are relatively accurate for the electrically thin substrate, which is also the most general case for the patch antenna design. Between them, the transmission-line model is simpler and can give good physical insight, but it is less accurate. However, the cavity model is more accurate but also more complex at the same time [28]. The analysis below uses the transmission-line model.

First of all, the dominant mode of a patch antenna is TM_{010}, which has the field distribution illustrated in Figure 4.2. The microstrip patch length (L) determines the resonating frequency, however, since the field is not only concentrated exactly under the area of the patch, fringing fields at the edges will extend the length of the patch. The extended length is denoted as ΔL, which is a function of the substrate material effective permittivity ε_{eff}, the patch width W and the substrate height h, as described by 4.1.

$$\Delta L = 0.412 \cdot h \cdot \frac{(\varepsilon_{eff}+0.3)(\frac{W}{h}+0.264)}{(\varepsilon_{eff}-0.258)(\frac{W}{h}+0.8)} \tag{4.1}$$

For $W > h$, which is the most general case in the patch design, the ε_{eff} equation is shown in 4.2.

$$\varepsilon_{eff} = 0.5 \cdot (\varepsilon_r + 1) + 0.5 \cdot (\varepsilon_r + 1) \cdot (1 + 12 \cdot h/W) \tag{4.2}$$
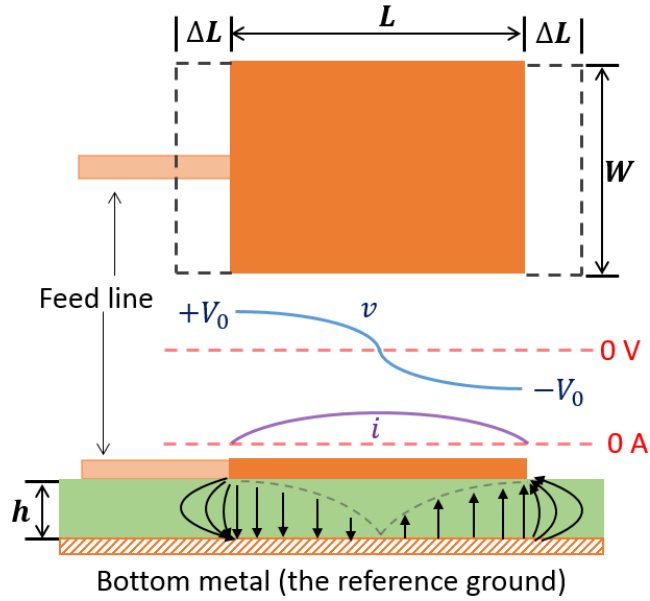
Figure 4.2. The rectangular patch antenna and the corresponding voltage, current, and field distribution.

Herein, the effective length of a patch L_{eff} could be defined as 4.3:

$$L_{eff} = L + 2 \cdot \Delta L \tag{4.3}$$

So the resonating frequency of a patch f_r, will be a function of L_{eff} and ε_{eff}, which is given in 4.4:

$$f_r = \frac{1}{2 \cdot L_{eff} \cdot \sqrt{\varepsilon_{eff} \cdot \varepsilon_0 \cdot \mu_0}} \tag{4.4}$$

Where, ε_0 and μ_0 are the vacuum permittivity and permeability.

For the radiation efficiency consideration, the width of a patch can be defined as shown in 4.5. In the real case, W will affect the radiation beamwidth, and a wider W will give narrower beamwidth, and slightly higher radiation gain at the same time [28].

$$W = 0.5 \cdot \lambda_0 \cdot \sqrt{\frac{2}{\varepsilon_r + 1}} \tag{4.5}$$

Where λ_0 is the wavelength of the resonating frequency in the vacuum.

The patch design process is based on 4.5, deciding the patch width at first, then one can determine ε_{eff} based on 4.2, and finally, by combining 4.1, 4.3 and 4.4, one can calculate the physical length of the patch. This design process is the simplest one, and the substrate loss tangent effect is not taken into consideration, but its result would provide us the initial design parameters when doing the optimization using EM simulation tools, such as ANSYS HFSS.
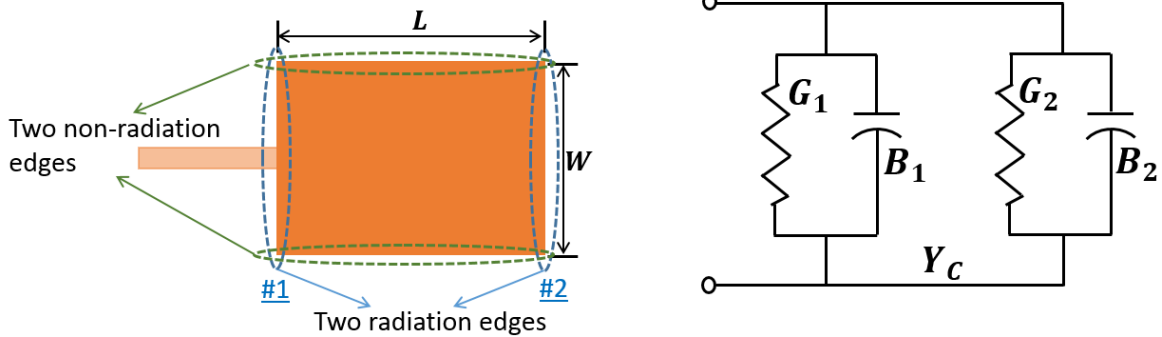
Figure 4.3. The rectangular patch and its equivalent circuit model.

The patch antenna impedance can also be analyzed using the transmission line model, which considers the patch as two radiation slots, where Figure 4.3 shows the equivalent circuit of a patch. The patch can be modeled as if it has edge-slot radiation. As shown in Figure 4.3, the edge which is perpendicular to the input transmission line is the radiating slot (blue dash circle), and correspondingly, the edge that is in parallel with the transmission line is the non-radiating slot (green dash circle). Each radiating slot is modeled as an admittance, which contains a conductance G and susceptance B. Since the slots of the patch have the same shape, so $G_2 = G_1$ and $B_2 = B_1$. And for the single slot radiation, its conductance is given in 4.6:

$$G = \frac{2P_{rad}}{|V_0|^2} \tag{4.6}$$

Where, P_{rad} is the radiated power from the slot, and V_0 is the voltage across it. The radiated power of the slot is determined by 4.7:

$$P_{rad} = \frac{|V_0|^2}{2\pi\eta_0} \int_0^\pi \left[\frac{\sin(0.5k_0 \cdot W \cdot cos\theta)}{cos\theta}\right]^2 sin^3\theta \, d\theta \tag{4.7}$$

So the slot conductance would be:

$$G = \frac{1}{120\pi^2} \int_0^\pi \left[\frac{\sin(0.5k_0 \cdot W \cdot cos\theta)}{cos\theta}\right]^2 sin^3\theta \, d\theta \tag{4.8}$$

The two radiating slots are separated by the patch length, L, therefore, except for the slot intrinsic conductance, there exists mutual conductance, which is defined as G_{12}:

$$G_{12} = \frac{1}{|V_0|^2} Re \oiint \vec{E_1} \times \vec{H_2^*} \cdot d\vec{s} \tag{4.9}$$

Where E_1 is the electric field radiated by slot 1, H_2 is the magnetic field radiated by slot 2, by applying the field equation into 4.9, the mutual conductance can be determined by 4.10:

$$G_{12} = \frac{1}{120\pi^2} \int_0^\pi \left[\frac{\sin(0.5k_0 \cdot W \cdot cos\theta)}{cos\theta}\right]^2 J_0(k_0 \cdot L \cdot sin\theta)sin^3\theta \, d\theta \tag{4.10}$$

At the resonating frequency, there should be $B_2 = -B_1$, which means that the resonating input admittance only has the real part, which is denoted as R_{in}. Figure 4.4 shows the typical input impedance vs. frequency curve of a rectangular patch antenna.

$$R_{in} = \frac{1}{2(G_1 + G_{12})} \tag{4.11}$$

Usually, the patch input resistance at the edge is between 150 to 300 ohms, which makes it difficult to realize impedance matching with the low characteristic impedance feed line, such

as the standard 50 Ω line. However, noticing the voltage and current distribution in Figure 4.2, the impedance is zero in the patch center intrinsically, which means the input impedance between the patch radiating edge and the center is varying. This impedance variation allows one to use the inset-feed method to realize impedance matching. Figure 4.5 illustrates the outlook of the patch antenna with inset feed and the impedance variation over the inset feed depth (y_0), and the impedance variation equation is given in 4.12.
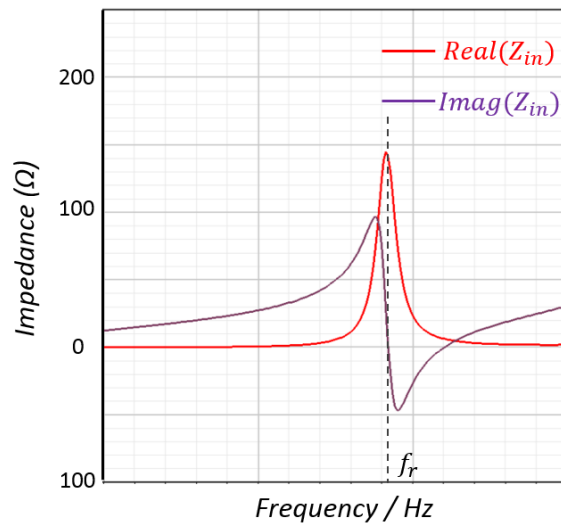
Figure 4.4. A typical rectangular patch antenna input impedance variation over frequency.

$$R_{in}(y = y_0) = R_{in}(y = 0)cos^2\left(\frac{\pi}{L}y_0\right) \qquad (4.12)$$

(a)   (b)
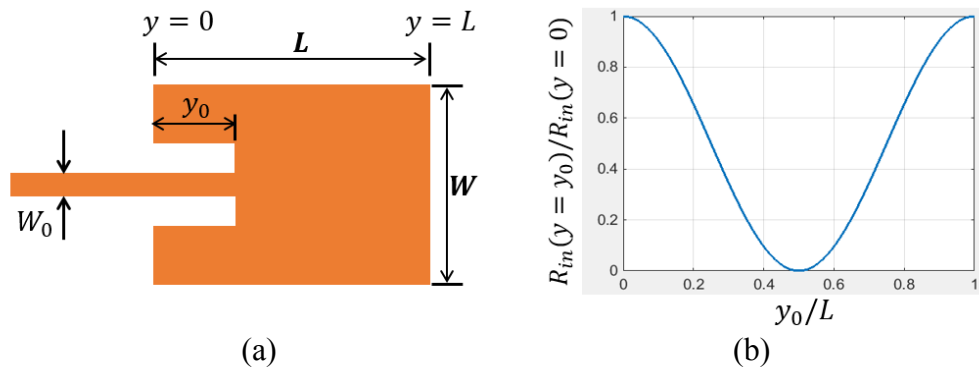
Figure 4.5. The illustration of the patch antenna with the inset-feed: (a) The structure; (b) impedance variation over the inset-feed depth (y_0).

72

There are other matching techniques that are usually used in impedance matching a patch antenna, like the backside direct feed using a connector, aperture feed, the $\lambda/4$ line, etc. However, they all have some limits in mm-wave design. For the backside direct feed with a connector, it should be the ideal case and usually used in low-frequency design, but it is impossible to utilize in the scenario with the electrically thin substrate and mm-wave designs, since the antenna size is tiny. The aperture feed method requires multilayer substrates, which is difficult to fabricate and align the different layers. For the $\lambda/4$ line, it would occupy more area. Therefore, in this chapter, all the 67 GHz patch antenna and its arrays are realized using the in-set feed technique.

Figure 4.6 shows the patch geometry and its typical radiation pattern. In (a), along with the patch length direction, the E-plane indicates the major E field radiation plane. Correspondingly, in parallel with the patch width, the H-plane, indicates the H field radiation direction. By observing the radiation in the E-plane and H-plane, one can evaluate the radiation performance. Ideally, the E-field of this type of patch antenna only radiates in ϕ direction, and in the E-plane, where it can be written as 4.13, and the H-plane can be expressed using 4.14.

In 4.14, the last term is a 'sinc' function of the product of the patch width and the cosine value of θ angle. As the patch width increases, the function's value will decrease faster with θ angle, which is the reason why the width of the patch controls the beamwidth. The maximum radiation is in $\theta = 90°$, and the directivity of a patch antenna can achieve 8 dB ideally.

<center>(a)   (b)</center>
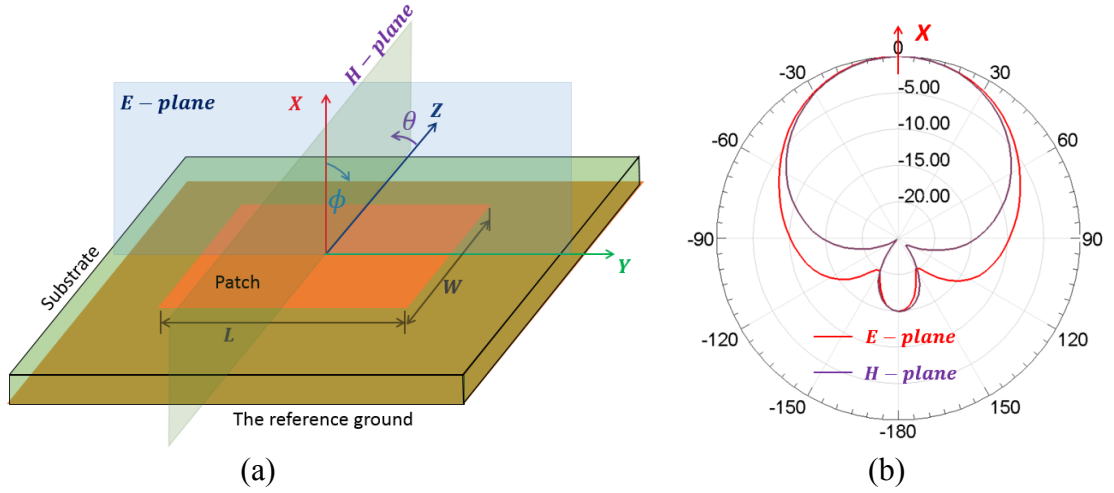
Figure 4.6. Patch geometry and radiation pattern: (a) patch geometry illustration; (b) The ANSYS HFSS simulated normalized radiation pattern.

$$E_{\phi\_E} = +j \frac{k_0 W V_0 e^{-ik_0 r}}{\pi r} \left\{ \frac{\sin(0.5 \cdot k_0 h \cdot \cos\phi)}{0.5 \cdot k_0 h \cdot \cos\phi} \right\} \cos(0.5 \cdot k_0 L_{eff} \cdot \sin\phi) \qquad (4.13)$$

$$E_{\phi\_H} = +j \frac{k_0 W V_0 e^{-ik_0 r}}{\pi r} \left\{ \sin\theta \cdot \frac{\sin(0.5 \cdot k_0 h \cdot \sin\theta)}{0.5 \cdot k_0 h \cdot \sin\theta} \cdot \frac{\sin(0.5 \cdot k_0 W \cdot \cos\theta)}{0.5 \cdot k_0 W \cdot \cos\theta} \right\} \qquad (4.14)$$

4.3 The patch and its UCAs realization on TerraGreen®

A. The substrate material

TerraGreen® substrate material from Isola Group is chosen to realize my designs. As shown in Figure 4.7, the material thickness is 0.127 mm, and the copper-clad thickness is 0.017 mm with 2-μm very low profile (VLP-2) foil treatment, which can make the surface roughness smaller than 2.5 μm [43].

The main reason that TerraGreen® was chosen is because the substrate has a low loss tangent, which is only 0.0055 at 60, 77 and 81 GHz. Based on [44], for microstrip lines, the attenuation factor caused by dielectric loss tangent can be expressed as 4.15:

<center>74</center>

$$\alpha_d = \frac{k_o \varepsilon_r (\varepsilon_{eff} - 1) tan\delta}{2\sqrt{\varepsilon_{eff}(\varepsilon_r - 1)}} \, Np/m \qquad (4.15)$$

17 µm copper clad with
VLP-2 foil treatment

$\varepsilon_r = 3.61$
$tan\delta = 0.0055$

127 µm
TerraGreen
Substrate
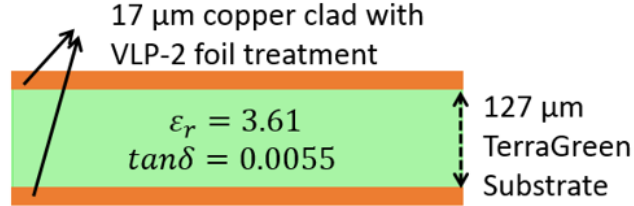
Figure 4.7. The illustration of the TerraGreen® substrate material from Isola Group.

Equation 4.15 indicates the dielectric loss is in a linear relationship with the frequency, and as the frequency increases, the loss will also be higher. In the mm-wave range, dielectric loss is the dominant loss in the microstrip line. Based on transmission line measurements, which are shown in Appendix E, the 50 Ω microstrip line on TerraGreen® has a loss of 0.082 dB/mm @ 67 GHz.

 B. 67 GHz patch antenna and OAM-UCAs.

The single 67 GHz patch was studied at first, and then the three UCAs with 4, 8 and 16 patches to generate OAM mode 1, 2 and -3 respectively. Simulation and measurement results will be given. Table 4.1 lists comparison results between the theoretical minimum requirement for the correct mode. The work presented herein on the UCA element number (N) and phase difference ($\Delta\varphi$) between adjacent elements is also included.

Table 4.1. The comparison results of minimum requirement and my work for OAM modes generation based on UCAs

OAM mode	Minimum		This work	
	N	$\Delta\varphi$	N	$\Delta\varphi$
±1	3	120°	4	90°
±2	5	144°	8	90°
±3	7	154°	16	67.5°

1). 67 GHz patch antenna

Figure 4.8 illustrates the structure of the 67 GHz patch antenna on the TerraGreen®️ substrate. To make it resonate at 67 GHz, the length, L_1 = 1.11 mm and the width, W_1 = 1.50 mm. To make the impedance match, the in-set feed is used here, and the in-set feed depth, L_2 = 0.33 mm, and the gap width W_2 = 0.15 mm, so that the input impedance of the patch equals to 75 Ω. The width W_0 of the microstrip feed line is set as 0.12 mm, which would make its characteristic impedance equal to 75 Ω too.

Structure	Size / mm
W_1	1.50
L_1	1.11
W_2	0.15
L_2	0.33
W_0	0.12
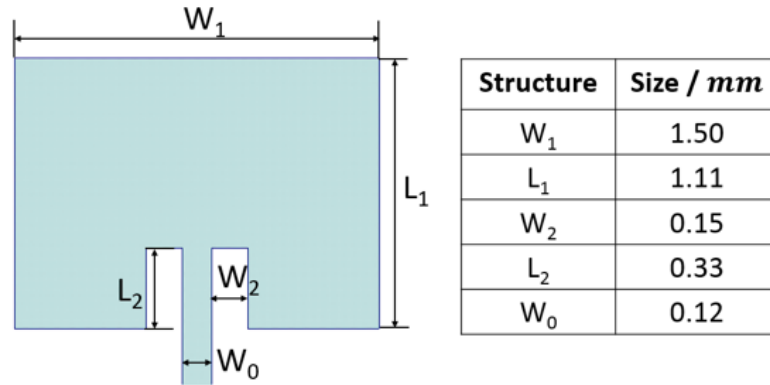
Figure 4.8. The proposed structure of 67 GHz patch antenna and its size.

The reason for using the 75 Ω microstrip line to feed the patch and its UCAs is from the consideration of the UCA feed network realization. If using the 50 Ω microstrip feed line, the width should be 0.27 mm, which will be difficult to make for a compact feed network for the arrays.

2). 4-patch UCA for OAM mode 1 generation

Based on the patch structure in section 1), the OAM mode 1 UCA is realized using 4 patches, where the structure is shown in Figure 4.9. The array size is 6.0 mm × 5.6 mm, with 3.0

76

mm radius, which is approximately $0.67\lambda_0$ at 67 GHz, and the spacing between each antenna element is 3.0 mm too. To be excited by a single source, a feed network with T-junction dividers has been designed. A quarter wavelength transformer is used in each T-junction to realize impedance match.

The phase shift is achieved using different lengths of the 75 Ω microstrip line and by rotating the orientation of the patches accordingly. In Figure 4.9, element 2 has a 90° phase shift from element 1. This is realized by the longer feed line of element 2, while elements 1 and 3 are fed using the same length feed line, but with the patches facing on the opposite directions, a 180° phase shift between them. To excite the individual element, the input power needs to pass through two T-junctions for this array.
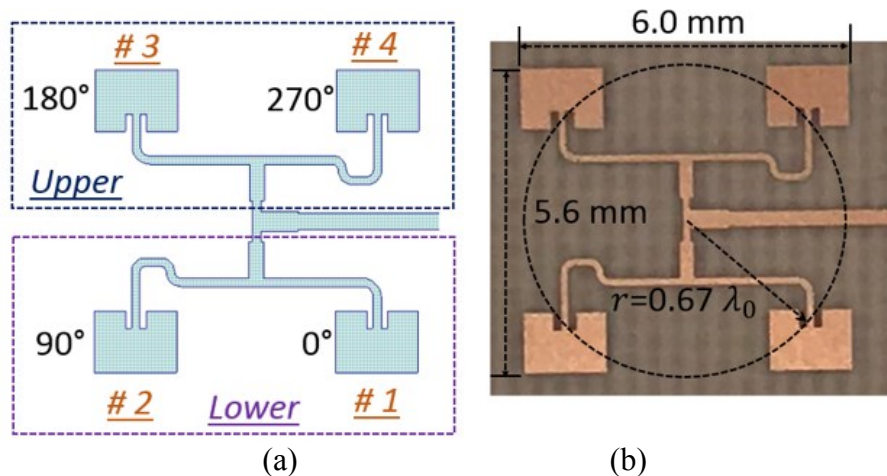
(a)   (b)
Figure 4.9. OAM +1 4-patch circular phased array: (a). Element number and phase illustration; (b). Sample size illustration.

3). 8-patch UCA for OAM mode 2 generation

Based on part 2), an 8-patch UCA for OAM 2 generation is realized, as shown in Figure 4.10. The size of the UCA is 11.8 mm×12.5 mm, with a radius of 5.6 mm, which is

approximately $1.25\lambda_0$ at 67 GHz. The phase difference between adjacent elements is 90°. For the lower part of Figure 4.10, the 90° phase shift is realized by longer 75 Ω microstrip lines for each element, while the upper part can be simply achieved by copying and rotating the lower part, with an extra 180° phase shift, which is realized by a longer feedline too. To excite the individual element, the input power needs to pass through three T-junctions for this UCA.

4). 16-patch UCA for OAM mode -3 generation

For OAM mode negative 3 (-3) generation, a 16-patch UCA was selected, which makes the phase shift between adjacent elements 67.5°. By using the same technique in parts 2) and 3), the structure realized is shown in Figure 4.11. Its size is 19.2 mm × 20.0 mm, with 9.0 mm radius, which is $2.0\lambda_0$ at 67 GHz. To excite the individual element, the input power needs to pass through four T-junctions for this array.

All the UCAs' sizes were optimized using ANSYS HFSS to balance the amplitude and phase along with the radiation pattern of the arrays structures. The UCAs were fabricated in the UT Dallas clean room where photolithography steps are used to etch 17 μm of Cu to define the patches, and the cleanroom fabrication process is given in Appendix D.
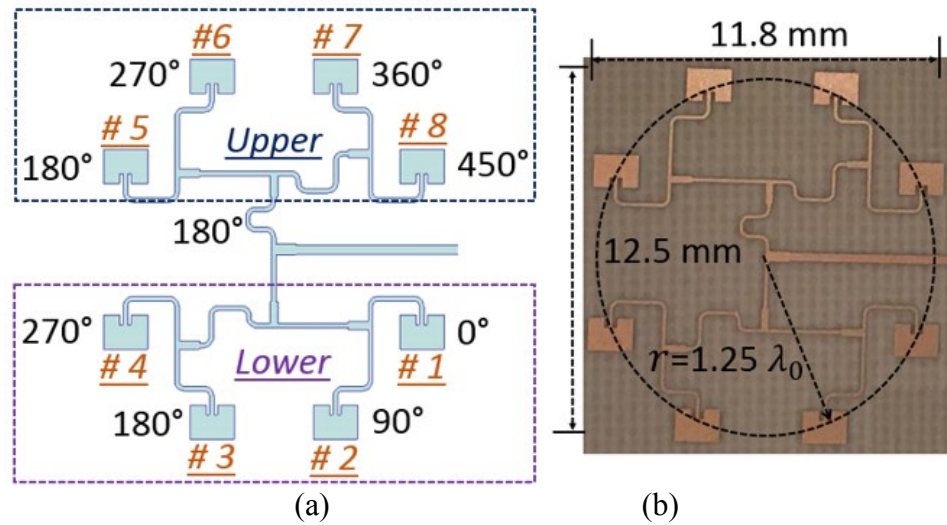
Figure 4.10. OAM +2 8-patch circular phased array: (a). Element number and phase illustration; (b). Sample size illustration.
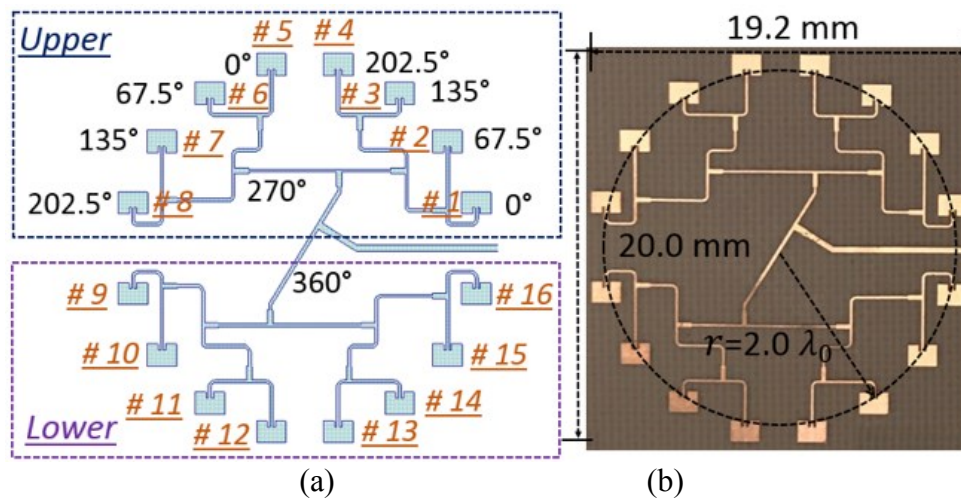
Figure 4.11. OAM -3 16-patch circular phased array: (a). Element number and phase illustration; (b). Sample size illustration.

C. Input return loss

A 1.85 mm end launch connector (1892-04A-6, from Southwest Microwave Inc.) is used here to measure the return loss from 0 to 67 GHz, due to the VNA and connector limitation. The simulated data goes to 70 GHz.

1). Single Patch Antenna

Since the patch antenna was designed with a 75 Ω feed line, to use this 50 Ω connector for measurement, a quarter wavelength transformer is added here to realize the impedance match, which has a width of 0.188 mm and the length of 0.670 mm. Figure 4.12 (a) shows the structure of the 67 GHz patch with the quarter wavelength transformer, the feed length is 9 mm in total. Figure 4.12 (b) shows the simulated and measured results, the simulated and measured return loss are both greater than 20 dB at 67 GHz, and the 10 dB bandwidth is from 65.9 GHz to 68.2 GHz, with 3.4% fractional bandwidth.

(a)   (b)
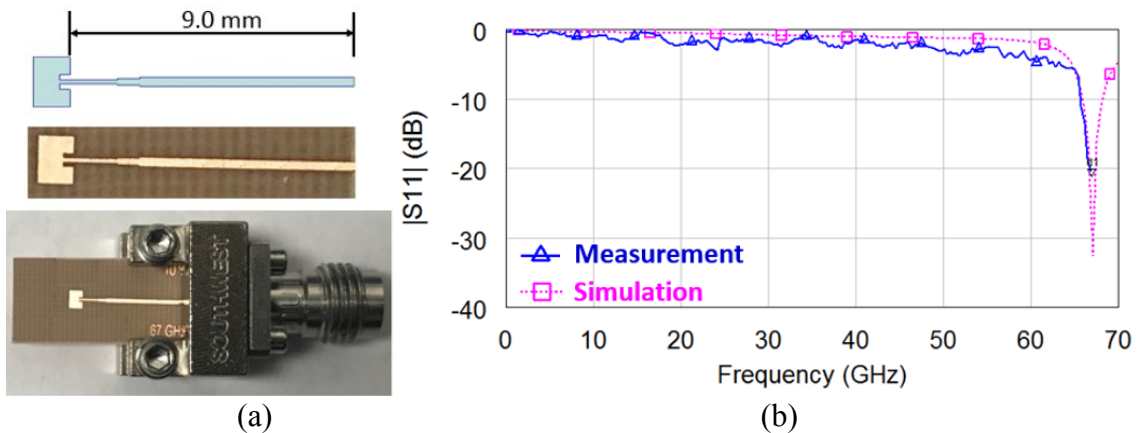
Figure 4.12. OAM -3 16-patch circular phased array: (a). Element number and phase illustration; (b). Sample size illustration.

In Figure 4.12, there exists a gap between the simulation and the measurement results, especially at the higher frequency range. This is caused by the end launch connector insertion loss, which was not included in the simulation. For example, at 60 GHz, the measured return loss is 4.26 dB, while the simulated result is 1.74 dB, the difference is 2.52 dB, based on its datasheet and the measurement result of the end-launch connector (Appendix E), the insertion loss is about

1.0 dB at 60 GHz. If taking it into consideration, there will be a 2.0 dB decrease in the simulated S11 curve, which will mitigate the gap between the simulation and measurement.

2). OAM-UCAs

As shown in Figure 4.13, each array's 50 Ω main feed line was extended to 24.0 mm (refer to the edge of the UCA) so that they can be bent to enable the phase measurement in the spherical chamber. Figure 4.13 also shows the simulated and measured return loss of the samples.

(1). Generally, the simulation and measurement results are in good agreement.

(2). Compared to the single patch antenna, the UCAs'10 dB bandwidths were extended. This is due to the extra loss from the 24.0 mm 50 Ω main feed line and the connector.

(3). The more elements in the array, the more variation on the S11 curve, this is caused by the reflection from individual patch and T-junctions of the feed network. To excite each element, the 4-patch UCA only needs two T-junctions, then three T-junction for the 8-patch UCA, while for the 16-patch UCA, it needs four T-junctions. Using a two-layer board where the feed line is on a lower level along with the dividers could eliminate this issue. In that case, the patches could be fed using aperture coupling.
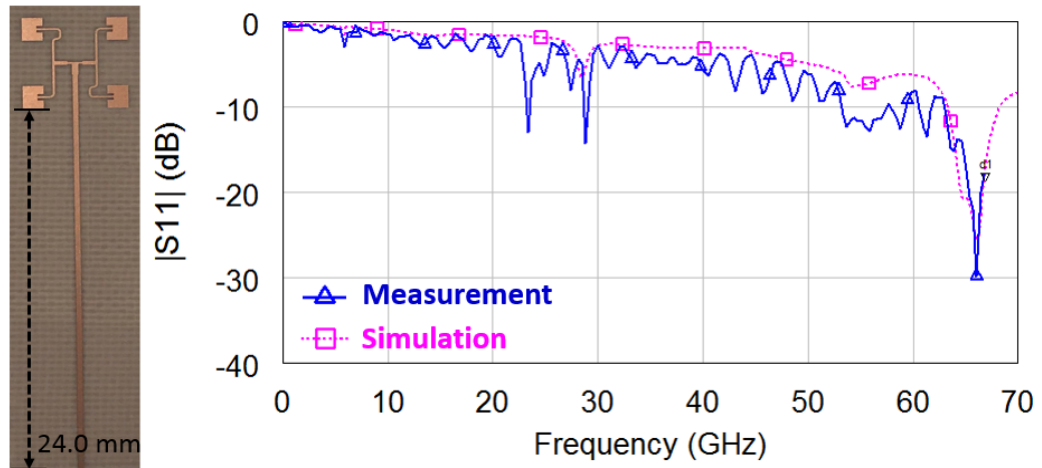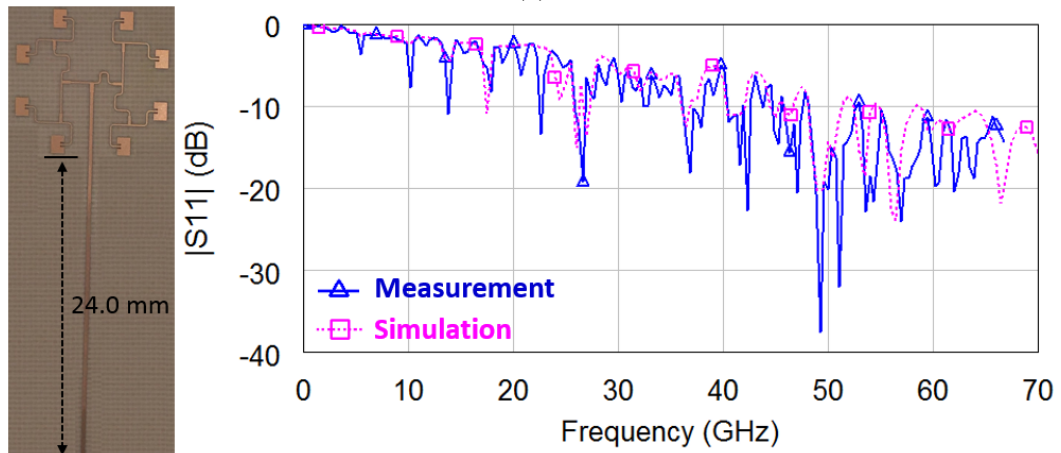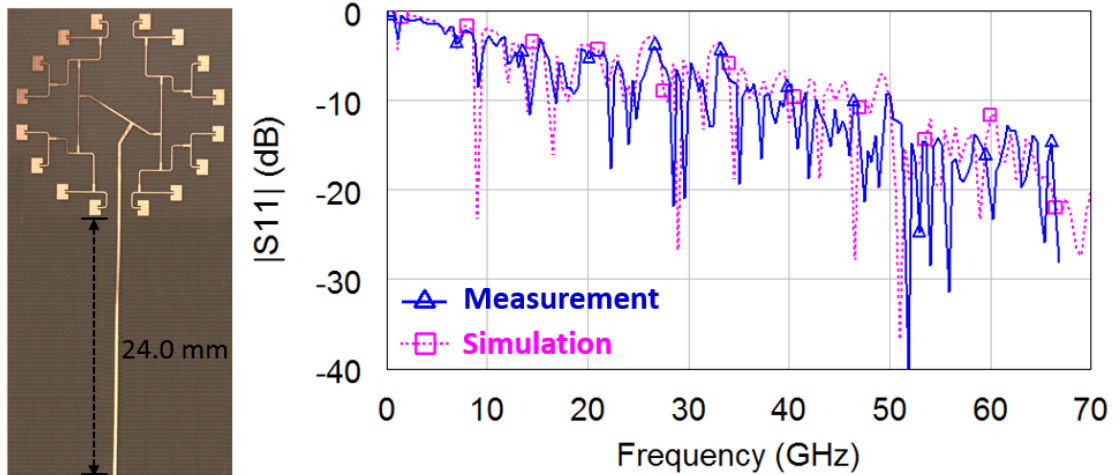
Figure 4.13. The three Samples' return loss simulation and measurement results:
(a). OAM +1 4-patch UCA; (b). OAM +2 8-patch UCA; (c). OAM -3 16-patch UCA.

D. Radiation Pattern and Phase Distribution

For radiation measurement purposes, the connector used for measuring |S11| was used to measure the three UCAs' radiation performance, with a Keysight PNA (E8361A) and Oleson Microwave Labs' OML module extenders up to 110 GHz. The chamber setup was the same as the one in Figure 3.20, and the near field scan was taken to capture the phase distribution and the normalized radiation pattern.

One of the features of the higher-order OAM mode ($l\neq0$) is the center null existence in the radiation pattern. Figure. 4.14 shows the HFSS simulation and measurement results of the radiation pattern cuts (H and V cuts) for each of the UCAs.

(1). The simulation and measurement radiation patterns are in good agreement, except for a few differences due to variations in fabrication and the presence of the AUT stand. The beamwidth is narrower in measurement compared to simulation.

(2). The larger the array radius is, the more side lobes in the radiation pattern. This is expected and cannot be avoided, since for generating higher OAM modes, more antenna elements should be involved to form the UCA.

(3). Based on the OAM-UCA factor in Chapter 2, the term, $J_l(ka \cdot sin\theta)$, determines the radiation peak position. Figure 4.15 gives the first peak position of the first kind Bessel function $J_l(x)$. Table 4.2 lists the comparison results of the radiation peak angle among the OAM–UCA factor calculation results, ANSYS HFSS simulation results, and the measurement results. The slight differences are caused by the existence of the feed network.

Figure 4.14. The 3 Samples' radiation pattern simulation and measurement results: (a). OAM +1 4-patch UCA; (b). OAM +2 8-patch UCA; (c). OAM -3 16-patch UCA.
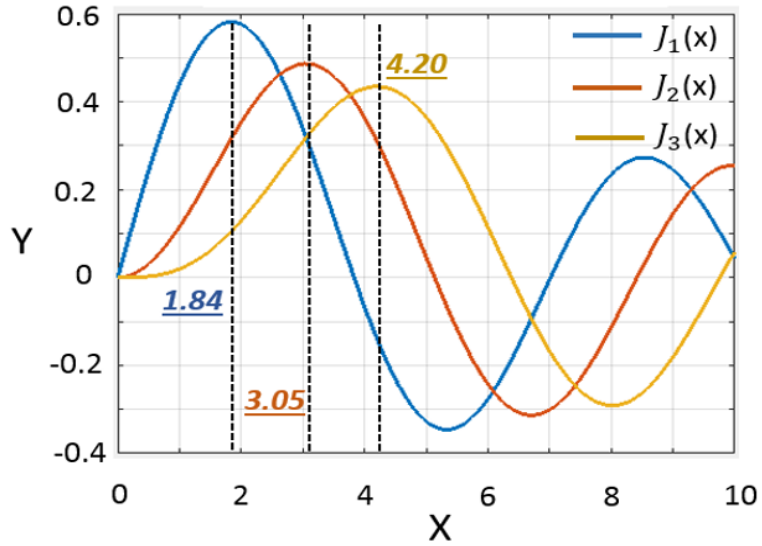
Figure 4.15. Illustration of the first 3 order of the first kind Bessel function curve peak positions, $J_1(x)$'s peak at x=1.84, $J_2(x)$'s peak at x=3.05, and $J_3(x)$'s peak at x=4.20.

Table 4.2. The comparison results of radiation peak positions of the three samples

Sample structure	OAM-UCA factor	HFSS		Measurement	
		H cut	V cut	H cut	V cut
4-patch UCA	25.8°	30°	26°	26°	25°
8-patch UCA	22.7°	22°	20°	22°	20°
16-patch UCA	19.3°	18°	18°	18°	18°

Figure 4.16 shows the simulated and measured results for the phase distribution of each UCA. The measurement results are taken from a plane 12 cm away from the UCA plane, which is $27\lambda_0$ at 67 GHz and is in the far-field range. Both simulation and measurement results show that the designed OAM-UCA can generate OAM mode of +1, +2 and -3 correctly. The three patch OAM-UCAs are all linearly polarized, as illustrated in Chapter 1, their SAM = 0, which

makes their observed phase distributions are the property of the OAM rather than the AM [24]. By simply mirroring the -3 OAM UCA structure, the OAM +3 mode can be achieved.

E. Conclusion

The three 67 GHz patch UCAs with the fixed feed network are realized on the TerraGreen® substrate material from Isola Group. The return loss simulation and measurement results indicate the arrays are working at the designed frequency. The radiation pattern and phase distribution are all simulated and measured. Due to the feed network effect, the measured radiation peak positions are slightly different with theoretical calculations, but still matched in general, and the phase distribution measurement results in the far-field indicate the three OAM-UCA generate the correct OAM modes successfully. In future work, these arrays will be utilized to conduct OAM based wireless communication experiment.

4.4 Summary

In this chapter, patch antennas were presented, and utilized with a high-performance mm-wave substrate material to realize three OAM-UCAs. The first section explained the motivation to use the patch antenna and the TerraGreen® substrate to build the OAM-UCAs. The second section gave the theory of patch radiation, which starts from the classical transmission line model and two-slot model, to the far-field radiation pattern derivation. Section 3 detailed the structure of the patch, the feed structure of the three OAM-UCAs, the measured and simulated input return loss. The measured radiation patterns and phase distributions were given, and compared with the simulation, which illustrated that the correct OAM modes can be generated by those UCAs.
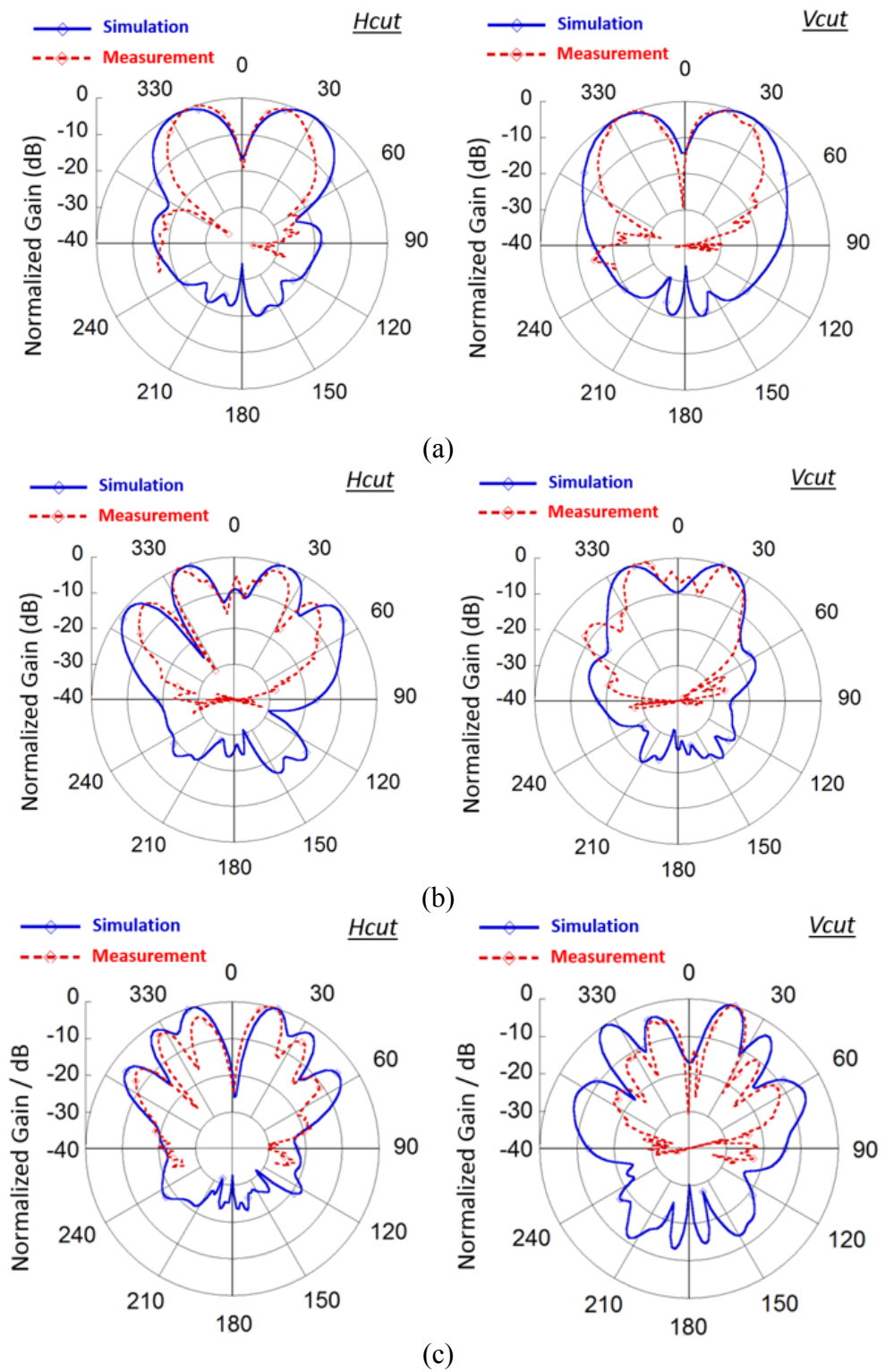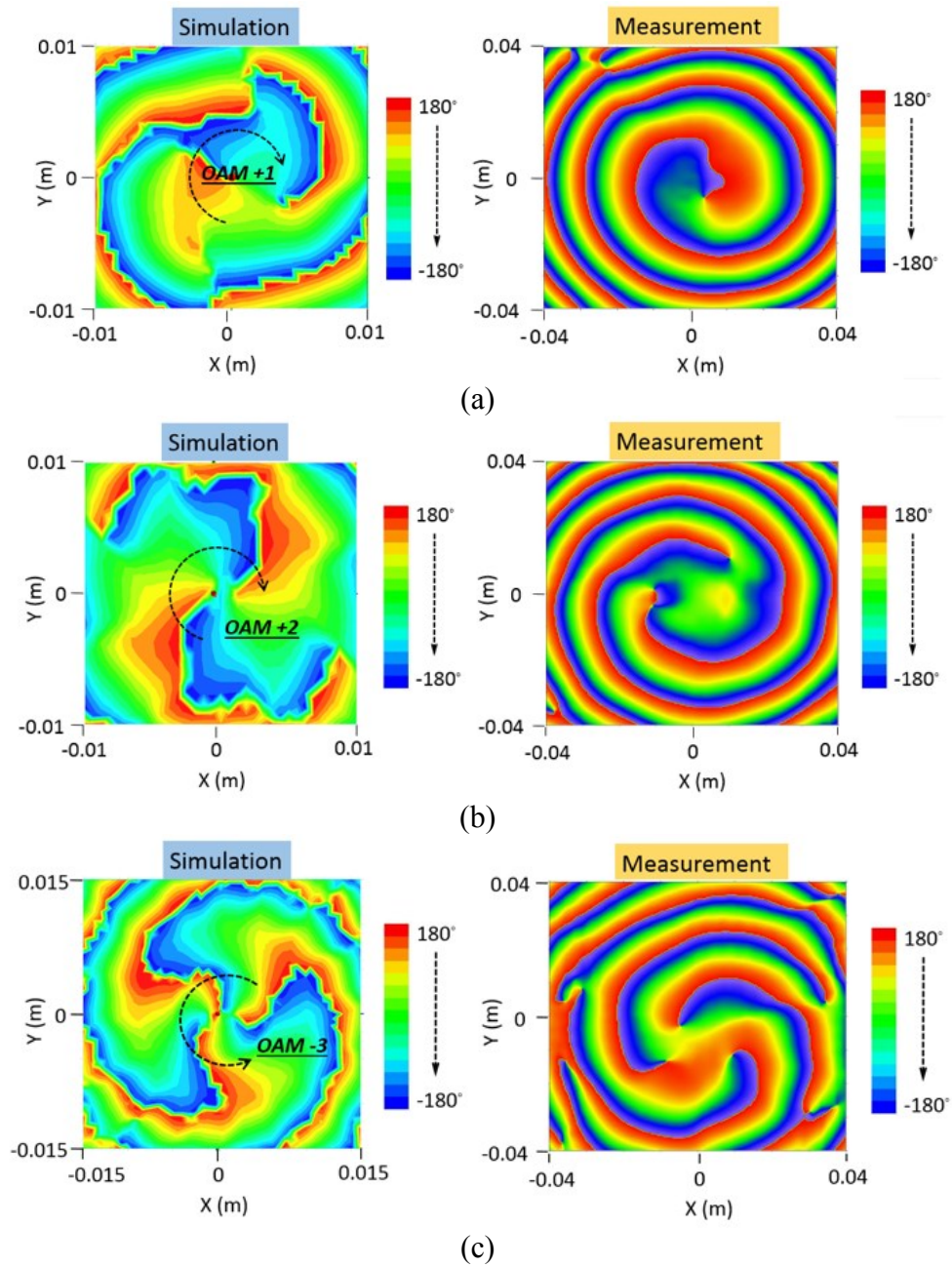
Figure 4.15. The 3 samples' phase distribution simulation and measurement results: (a). OAM +1 4-patch UCA; (b). OAM +2 8-patch UCA; (c). OAM -3 16-patch UCA.

CHAPTER 5

2.4 GHZ OAM-UCA BASED WIRELESS COMMUNICATION

5.1 Introduction

As illustrated in Chapter 1, the OAM wireless communication is based on orthogonality among different OAM modes. In Chapter 3 and 4, generating OAM modes using UCAs for mm-wave realization was introduced. At the mm-wave frequency, demonstrating communication links is difficult and many issues arise. The antenna arrays are less than 30 mm × 30 mm, and it is difficult to align the transmitter and receiver arrays over some distance. Besides, due to the measurement instruments limitation, the received signal could not be accurately detected at 67 or 73 GHz. A down-conversion can be used but has the extra loss, which would make the experiment results less accurate. To avoid this problem and to verify the OAM based wireless communication at the same time, a communication system based on 2.46 GHz patch antenna UCAs was designed. This chapter details the design, fabrication, and measurement of OAM-UCAs that operate at 2.46 GHz.

5.2 OAM wireless communication based on 2.46 GHz patch UCAs

5.2.1   Patch UCA for OAM mode 1

A. Substrate material

For the 2.46 GHz patch antenna and its OAM-UCA designs, the traditional 0.5 oz double-sided copper cladded FR4 board is used, which has 1.5 mm thickness, $\varepsilon_r = 4.15$, $tan\delta =$

0.012. The entire board size is 304.8 mm × 228.6 mm, which is suitable for the 4- and 8-patch UCA designs.

B. 2.46 GHz patch antenna design

Following the patch antenna design steps in Chapter 4, the optimization of the arrays is done using ANSYS HFSS. The patch resonates at 2.46 GHz. Figure 5.1 shows the patch size and the simulation setup in ANSYS HFSS. The patch length is 28.6 mm, and the width is 40.0 mm, to make the input impedance match with the 50 Ω SMA connector (901-9892-RFX from Amphenol Corporation), the backside feed position is 7.6 mm from the edge. Figure 5.2 shows the simulated and measured input return loss, which indicates the patch resonates at 2.46 GHz, and the 10 dB bandwidth is from 2.435 to 2.487 GHz.
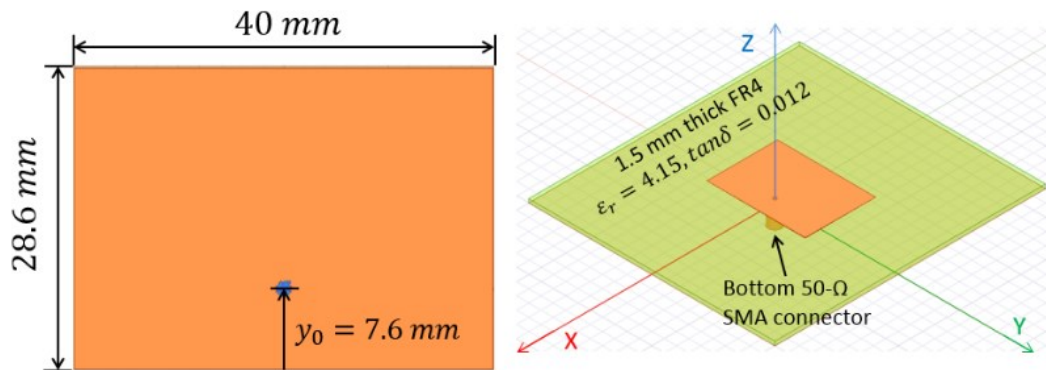
Figure 5.1. Illustration of the 2.4 GHz patch size and simulation setup.

According to ANSYS HFSS, the simulated gain of the single patch is 4.86 dB. The comparison method was utilized here to capture the single patch antenna gain [46], and the reference antenna is a commercial whip antenna (W1059) from PULSE LARSEN ANTENNAS® with 5 dB gain at 2.46 GHz [47]. Figure 5.3 shows the reference antenna size, geometry and the gain vs. frequency result from its datasheet. In order to make its gain to be 5

dB at 2.46 GHz, the bending setup was taken (the red line in Figure 5.3). Using the UTD planar chamber to take the measurement, the scanner used is the NSI2000 planar scanner from NSI-MI technologies, and the setup is shown in Figure 5.4. More details on the setup can be found in Appendix F. To capture the radiated power from the antenna, an open-ended waveguide (OEWG) is used to serve as the receiver probe, and it is a WR340 structure, which works from 2.2 to 3.3 GHz. The planar chamber measured result indicates the gain of the single patch antenna is 4.87 dB at 2.46 GHz, which is close to the simulated result.

Figure 5.5 shows the measured radiation pattern of the reference whip antenna at 2.46 GHz. The 3-dB beamwidth in the horizontal direction is about -40° to +40°, while in the vertical direction is about -15° to +15°. The polarization isolation is larger than 17 dB, as shown by the blue cross-pol plots. For comparison, Figure 5.6 shows the measured radiation pattern of the patch antenna at 2.46 GHz, the 3-dB beamwidth in the horizontal and vertical direction are both about -30° to +30°, and the polarization isolation is larger than 20 dB.
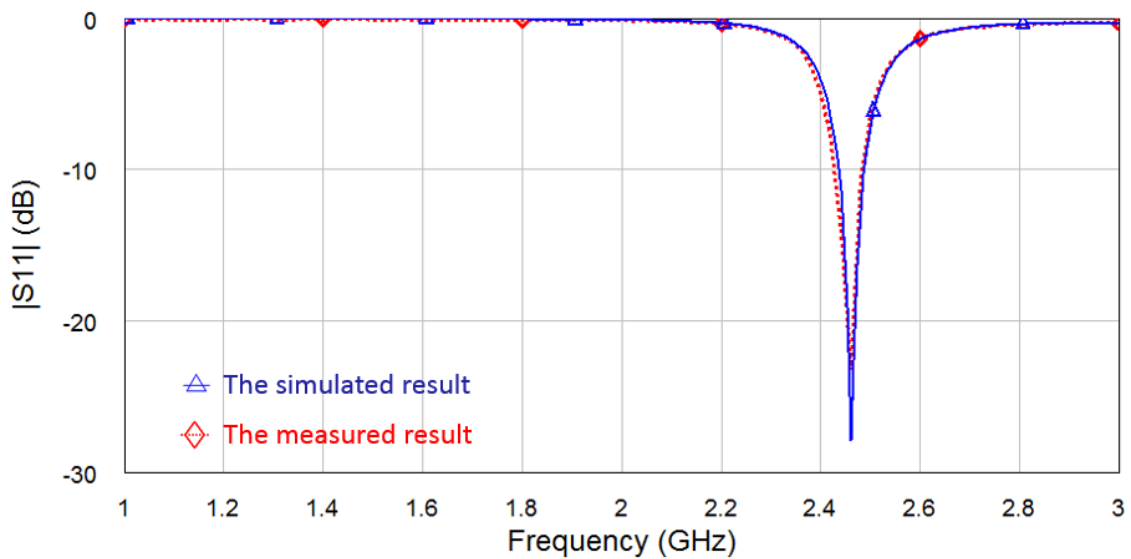
Figure 5.2. The input return loss of the designed 2.4 GHz patch.

172 ± 2.0 mm

36.7 ± 0.5 mm

Gain = 5 dBi @ 2.46 GHz
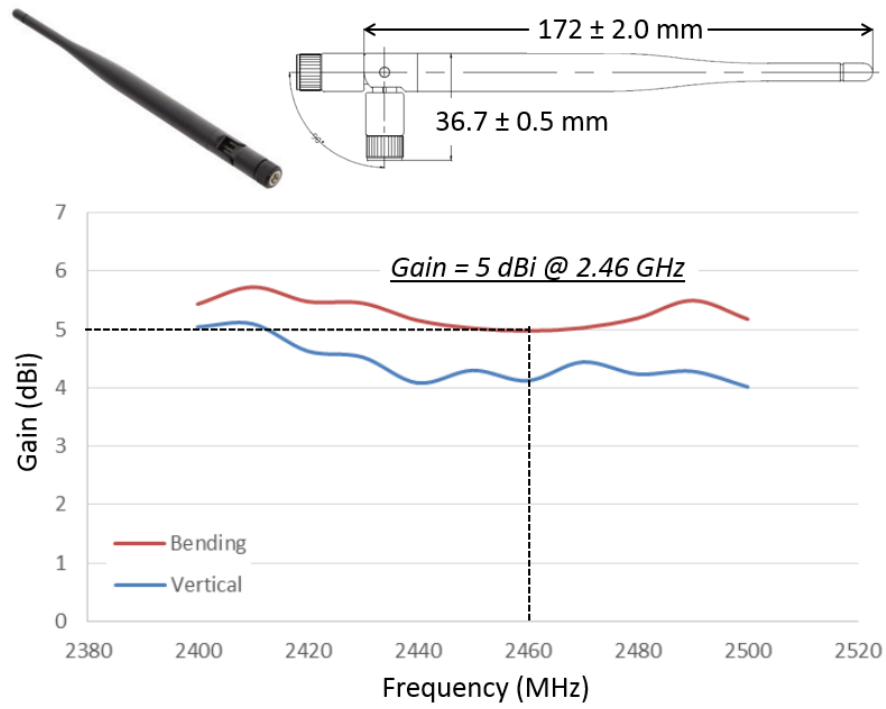
Figure 5.3. The reference whip antenna size and gain result [47].

Open-ended
waveguide
(OEWG): WR 340

H cut

Antenna under
test (AUT)
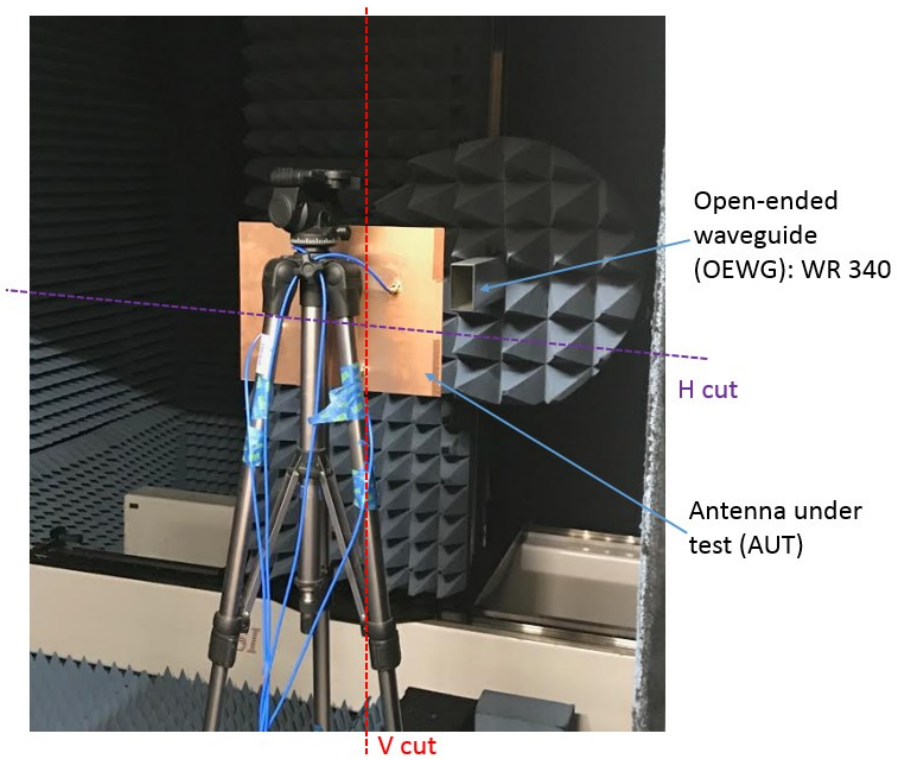
V cut

Figure 5.4. NSI2000 planar chamber measurement setup.
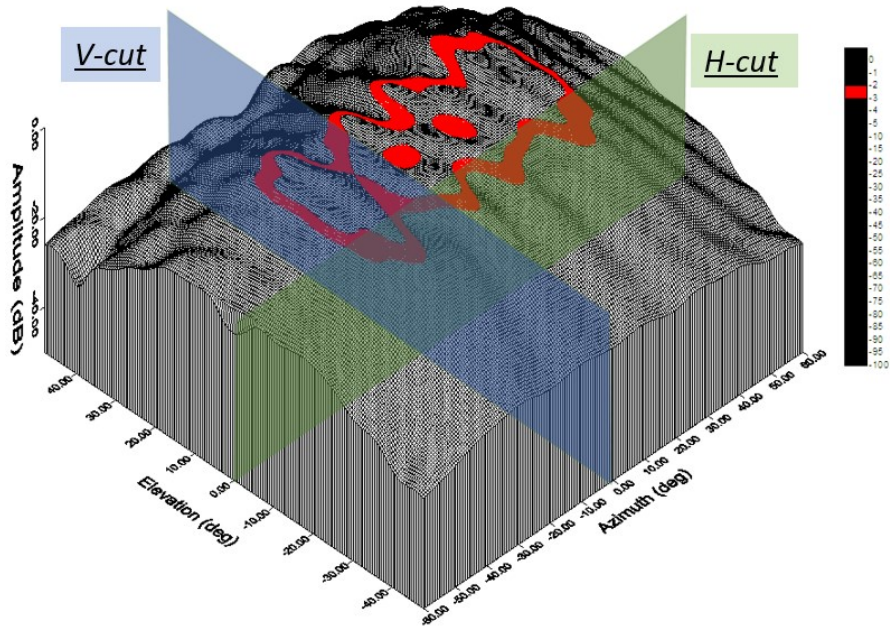
(a)
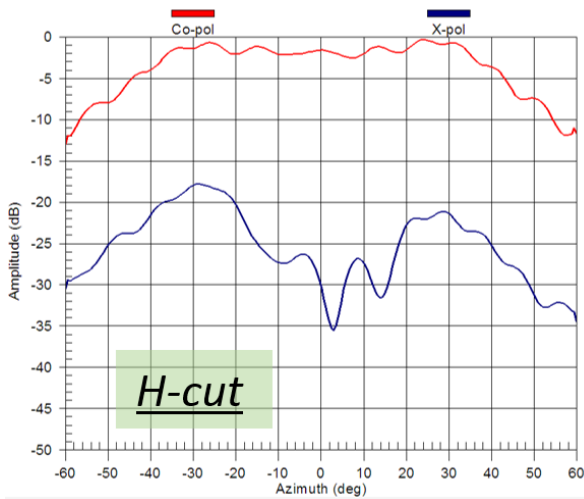
(b)
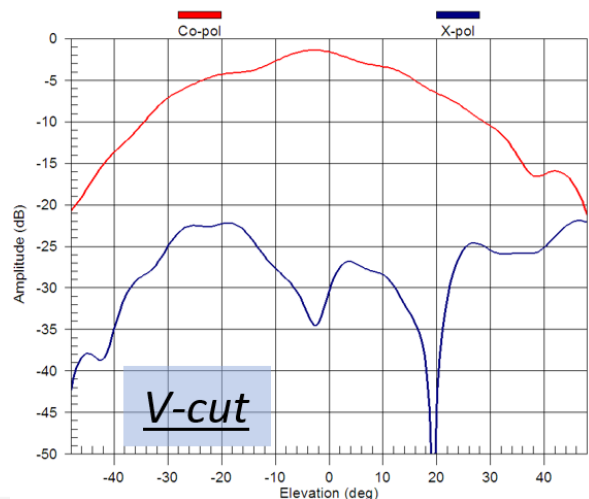
(c)

Figure 5.5. The reference whip antenna radiation pattern at 2.46 GHz: (a) 3D radiation pattern;
(b) H-cut; (c) V-cut.

(a)

(b)

(c)
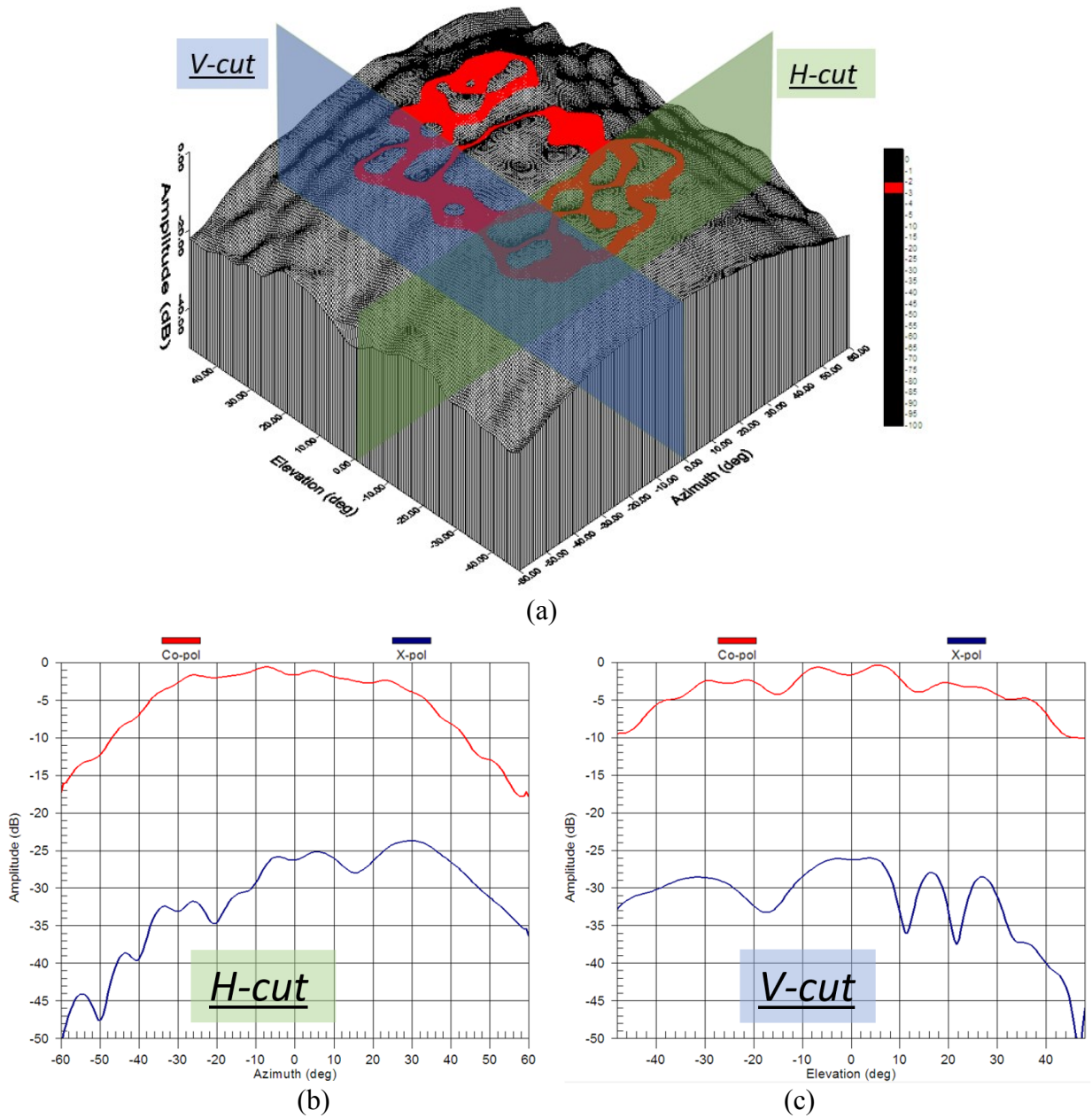
Figure 5.6. The rectangular patch antenna radiation pattern at 2.46 GHz: (a) 3D radiation pattern; (b) H-cut; (c) V-cut.

C. 8-patch OAM UCA design

An 8-patch UCA is utilized to generate OAM mode -1 and +1 using different feed networks. Since the FR4 board used is 304.8 mm × 228.6 mm, the 8-patch UCA radius is kept as 88.5 mm, which is about $0.73\lambda_0$ at 2.46 GHz, and based on Chapter 2, the divergent angle for OAM mode +1 and -1 would be 22°. Figure 5.7 illustrates the UCA size and geometry.

D. 8-patch OAM UCA feed network design

The feed network was designed for OAM mode +1 and -1 generation, and correspondingly, the phase shift between the adjacent elements should be ±45°, based on the patch UCA element feed positions. Those feed networks are realized using the same board material. Figure 5.8 shows the top view and the bottom view of the feed networks, where three T-junctions are involved in the feed networks to provide the correct phase shift and equal power distribution. The center connector (# 0 in Figure 5.8 (a)) is connected to an RF cable and then connected to the RF sources. The same backside feed connector with the UCA board is used here, and to connect with the UCA board, the adapter – 'ADP-SMAM-SMAM male to male' from Linx Technologies® is utilized. The feed network board and the 8-patch UCA board are back-to-back (B2B) connected, and the OAM-UCA module is configured as shown in Figure 5.9, whose thickness is about 30 mm.

In Figure 5.8 (a), No. 0 is the center pin position, which should be connected with the RF source. From the center pin to each feed point, the average length is about 140 mm, which will introduce an extra 1- dB loss due to the feedline loss. Ideally, each feed point will have a power level of 10 dB lower than the input power.

94

(a)

901-9892-RFX from
Amphenol Corporation
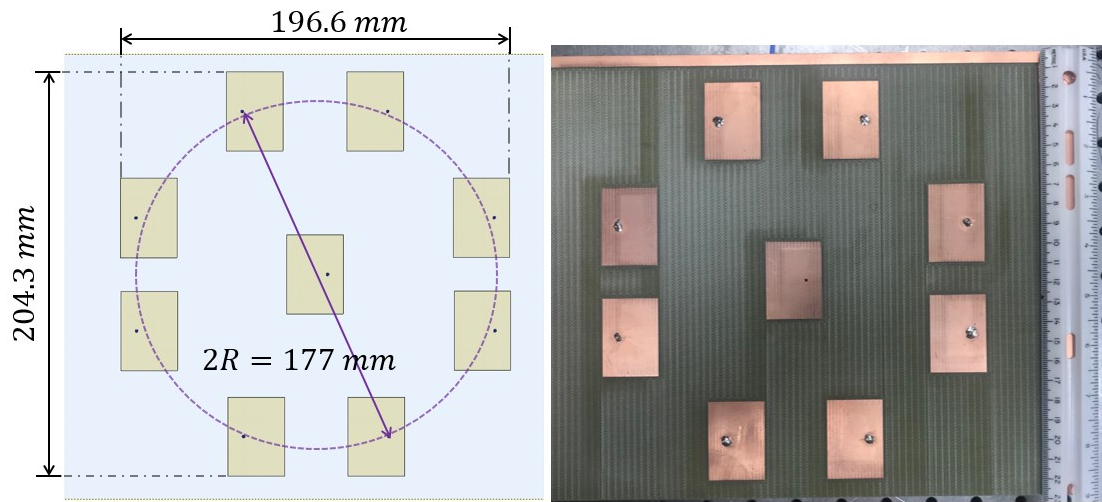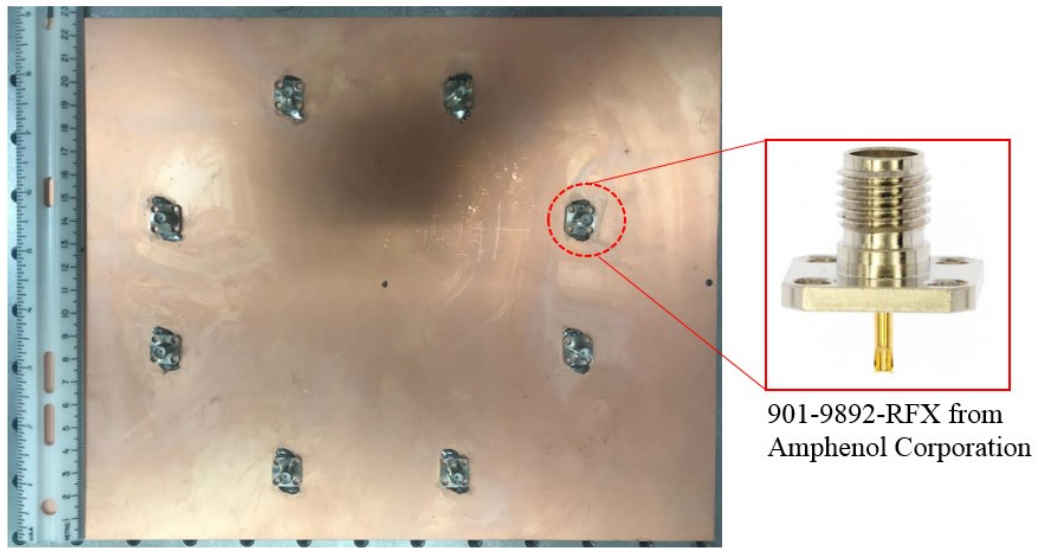
(b)

Figure 5.7. The illustration of the 8-patch UCA: (a) Size and the top view; (b) The bottom view and the 50 Ω connector.
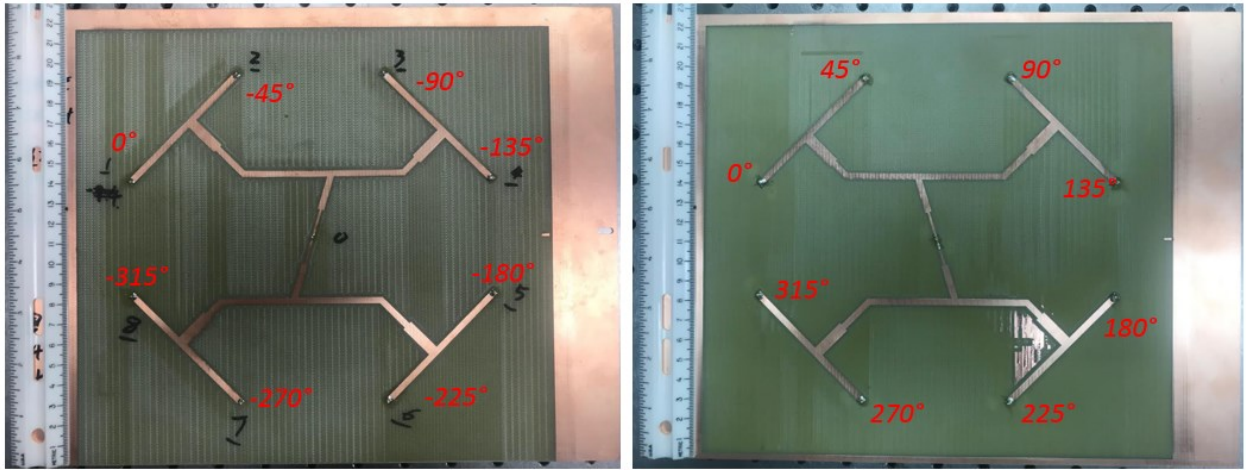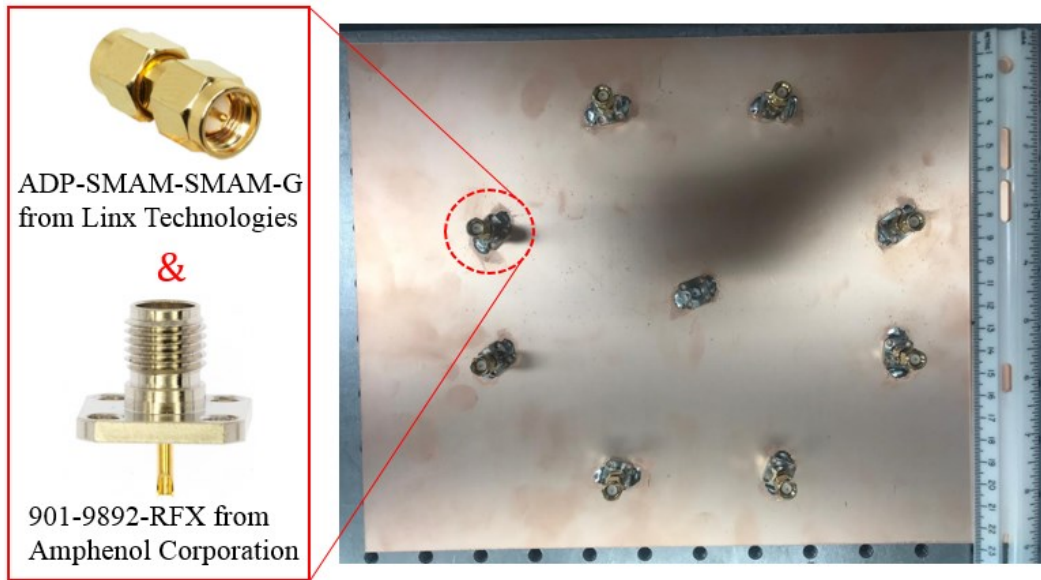
Figure 5.8. The illustration of the 8-patch UCA feed network: (a) The top view of OAM mode +1 feed network; (b) The top view of OAM mode -1 feed network; (c) The bottom view of the feed network.
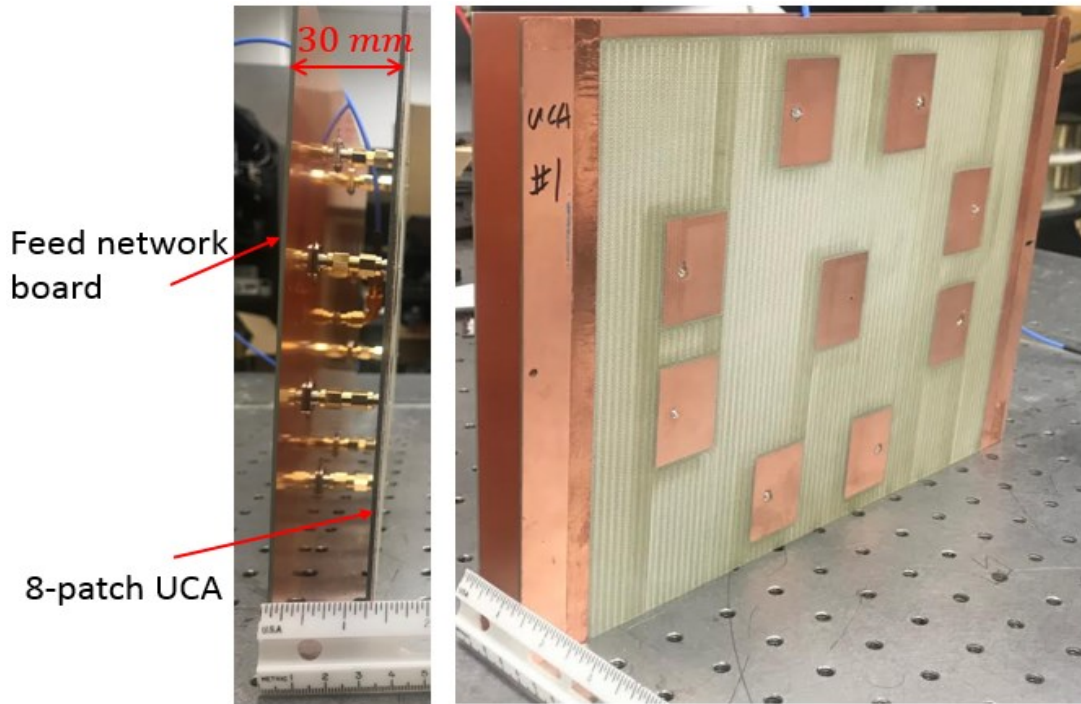
Figure 5.9. The entire OAM-UCA configuration, the total thickness is approximately 30 mm.
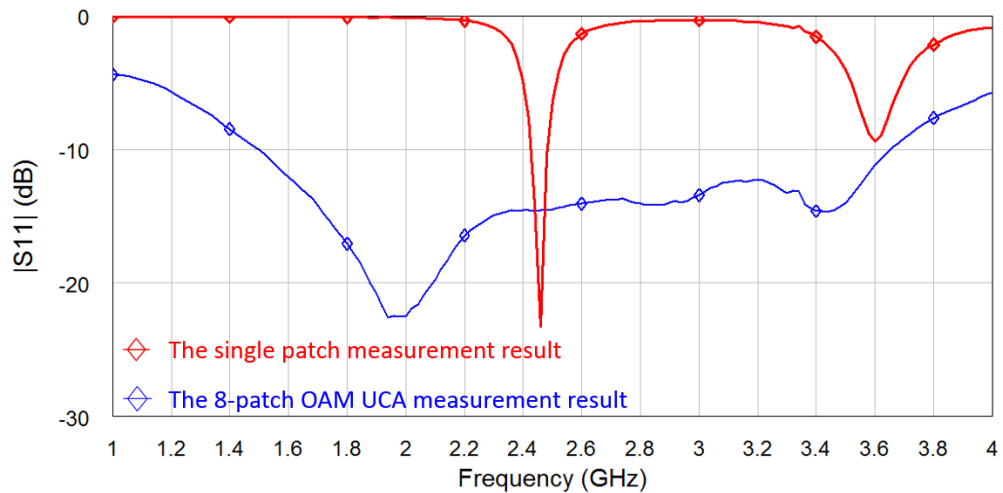
Figure 5.10. The input return loss comparison between the single patch and the 8-patch OAM-UCA module.

Figure 5.10 shows the input return loss comparison between the single patch and the OAM-UCA module for mode 1 generation. At 2.46 GHz, the return loss is 14 dB, and the whole S11 curve moves lower, which is mainly caused by the feed network loss. Figure 5.11 and 5.12

show the measured radiation pattern and phase distribution in the far-field range respectively, which indicates the correct mode is generated, and the measured gain is 4.66 dB.

(a)

(b)

(c)
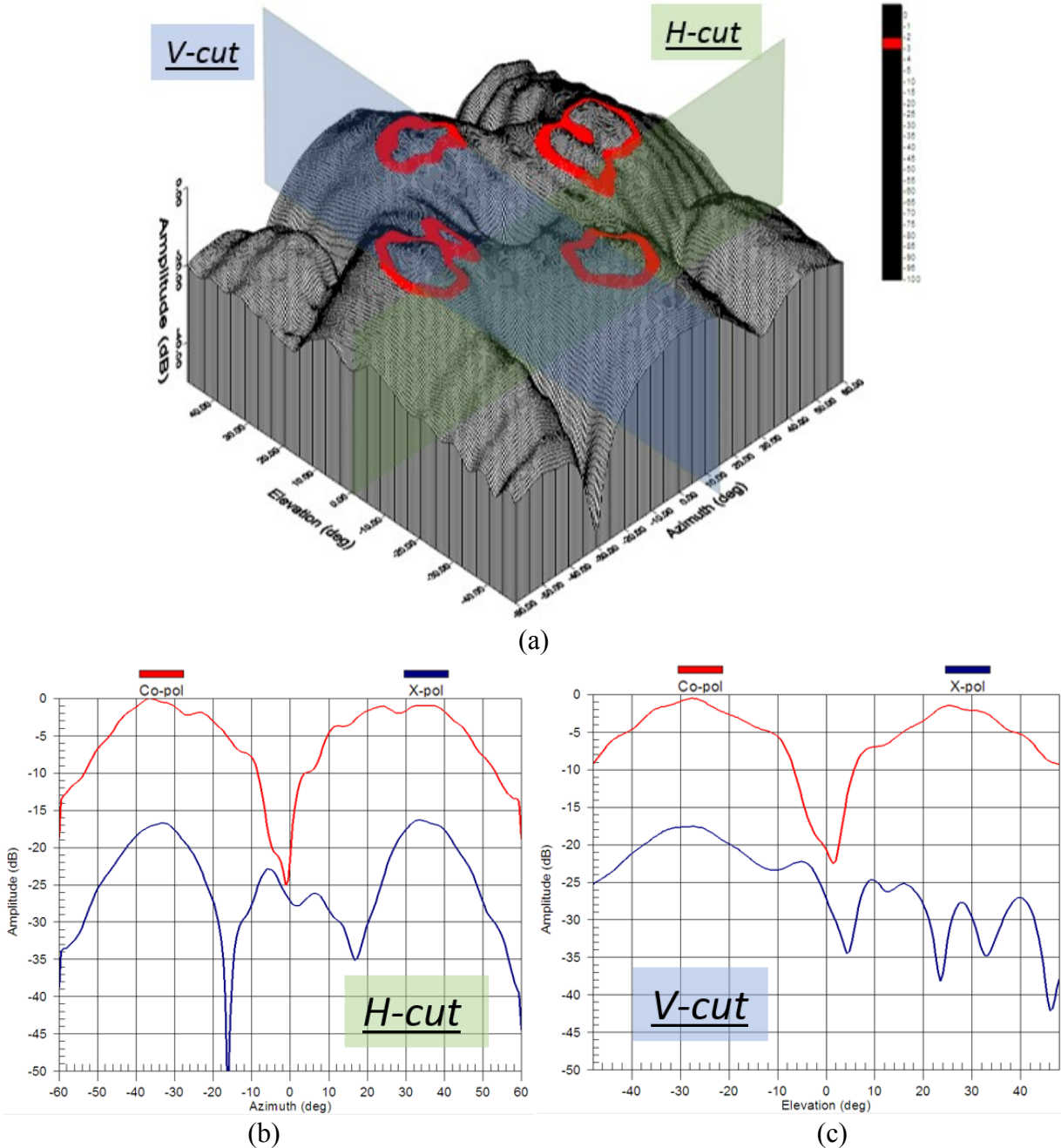
Figure 5.11. The radiation pattern of the OAM-UCA module for mode 1 generation: (a) 3D radiation pattern; (b) H-cut; (c) V-cut.
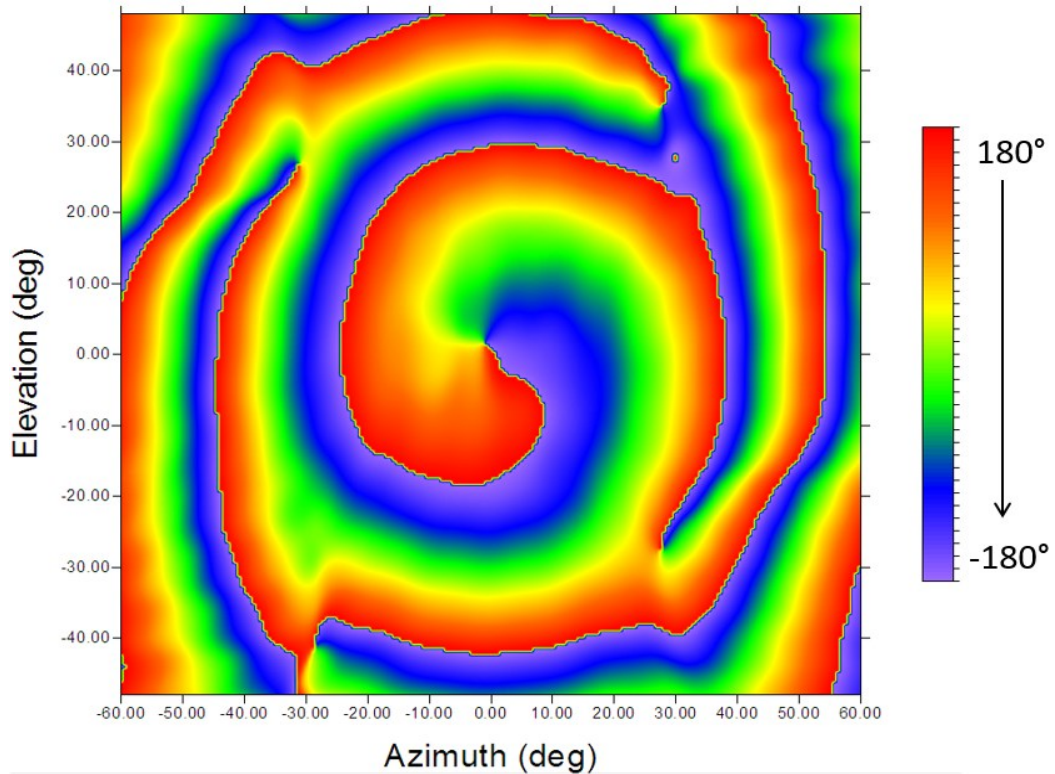
Figure 5.12. The phase distribution of the OAM-UCA module for OAM mode +1 generation at 2.46 GHz.

5.2.2 Link setup and experiment results

Figure 5.13 is the sketch of the communication link setup, where the signal generator works as the source, which has 10 dBm output power at 2.46 GHz. The spectrum analyzer works as the receiver to check the received power level, and its resolution bandwidth (RBW) and the video bandwidth (VBW) are both set at 10 kHz, and no attenuation is applied, which provides a -90 dBm noise floor. Both TX and RX UCA are the 8-patch UCA modules for OAM mode +1 or -1. Two isolations are checked here, one is the OAM mode isolation, which is verified by the power level difference of the received signal when TX and RX UCAs are in the different OAM modes but with the same polarization. The other is the polarization isolation, which is verified by

the power level difference of the received signal when TX and RX UCAs are in the different polarizations but with the same OAM modes. Figure 5.14 is a photo of the experimental link demo manually realized in the lab. Table 5.1 lists the test conditions and results. Group #1 is the ideal case, where the polarization is the same and mode is the same. Compared to group #2 and #3, the polarization isolation can achieve 24 dB, the OAM mode isolation between +1 and -1 can be 18 dB (1-m separation). As the TX-RX separation increases, there exists a multipath effect, which will decrease the accuracy of the experiment, such as the 3-m separation case. This multipath effect can be mitigated by using a larger UCA radius, which will make the divergent angle smaller. In the NTT case [27], its 16-element UCA with a radius of $28\lambda_0$ at 28 GHz can give a smaller than 1-degree divergent angle, while this work is 22-degree in theory. In addition, lots of other instruments and furniture surround the experiment link, which is affecting the results, by placing the whole link in a chamber would lead to an improved result.

Except for the multipath effect, another reason decreasing the OAM mode isolation is that the UCA module with the current feed network cannot distribute the equal power and provide the exact phase shift to each element perfectly. This would make the wrong modes still have some power left in the receiver. The third reason is the alignment, this experimental demo is not using a professional alignment tool but the manual adjustment. At 2.46 GHz, using the UCA with OAM modes ±1, the divergent angle is 22-degree in theory, even in a 1-m separation, the received power at the RX UCA is already over 15 dB lower than the peak radiation. In 1-m separation, 1-cm center shift between TX and RX UCAs would cause the power imbalance in the RX UCA's elements, therefore the mode isolation would degrade.

Using the wireless lab of Dr. Murat Torlak (UT Dallas, ECE department) and software-defined radio (USRP 2901 from National Instruments®) to transmit and receive QPSK and 16 QAM signals produced similar issues mentioned previously. In that experiment, even using the wrong OAM modes between TX and RX UCAs, the receiver could still decode the message signal correctly with nearly the same bit error rate (BER). Since the receiver's sensitivity is high, even with 18 dB OAM mode isolation, the signal could still be decoded correctly. This indicates leakage of the signal due to the poor mode isolation and better efforts to improve the demo setup.

The traditional antenna gain concept is not suitable for the of OAM-UCA based communication link, since its radiation pattern has a center null. As the transition distance increases, the TX UCA gain seen at the receiver side decreases. The gain is not a fixed number as the traditional case, it is distance-dependent.
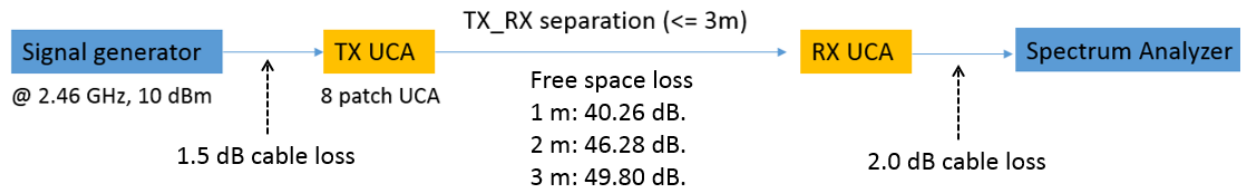
Figure 5.13. OAM communication link demo at 2.46 GHz.

Table 5.1. The communication link configuration and results

Group number	TX mode	RX mode	TX & RX polarization	The RX power at different separation (dBm)		
				1 m	2 m	3 m
#1	+1	+1	Same	-31	-48	-38
#2	+1	+1	Different	-55	-62	-52
#3	+1	-1	Same	-49	-56	-49
#4	+1	-1	Different	-53	-67	-55
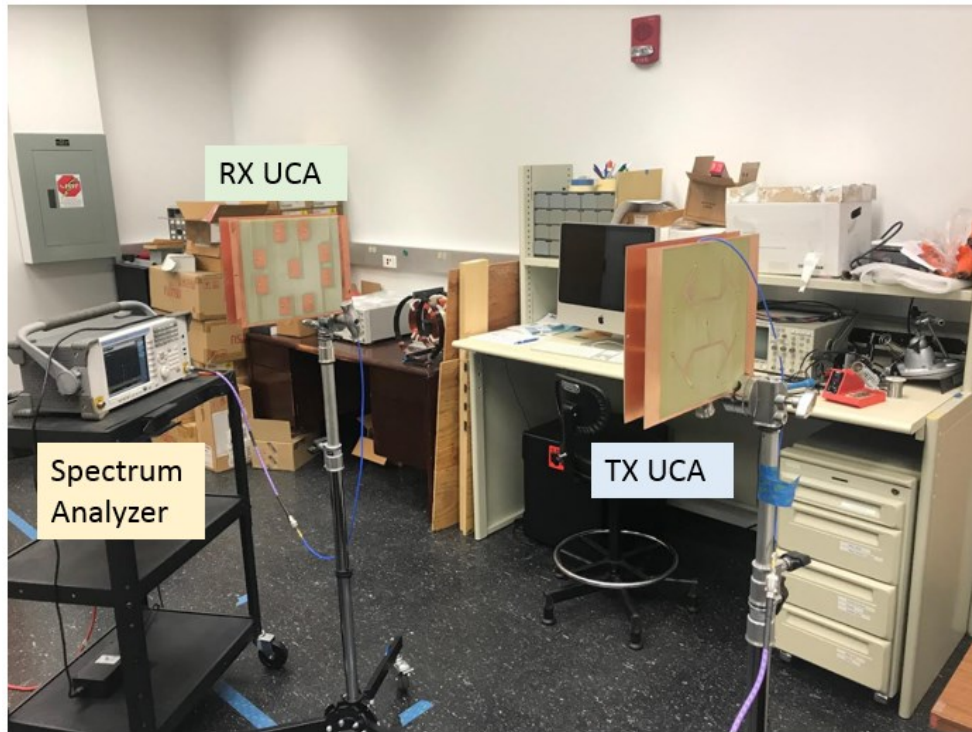
Figure 5.14. The realized experimental OAM communication link in our lab.

5.3 Summary

In this chapter, two 2.4 GHz OAM-UCAs were realized by using the traditional FR4 substrate material to generate the OAM mode +1 and -1. Both the simulation and measurement results indicate the correct modes are generated. A communication link based on the OAM-UCA modules was realized in the lab, which illustrated that OAM mode isolation is the key to successfully communicate at 2.4 GHz. The multipath effect, the non-perfect UCA feed network design, TX-RX alignment all affected OAM mode isolation, and degraded the performance of the OAM based communication link. More work needs to be done for OAM to be utilized in this lab-based wireless communication demonstration.

CHAPTER 6

SUMMARY AND FUTURE WORK

6.1 Summary

This dissertation has presented efforts on the generation of radio beams carrying non-zero OAM modes using the UCA method. A dipole antenna was applied from 71 to 76 GHz to build the OAM-UCA, and demonstrated the UCA's performance with different OAM modes. Two different types of feed networks, and a method to remove backside radiation of the dipole UCA to improve gain were also demonstrated. Secondly, a 67 GHz patch has been used to realize the OAM-UCAs for modes +1, +2, and -3, and the OAM-UCA factor has been used here to verify its correctness. All the 73 GHz and 67 GHz samples were fabricated in the cleanroom of UT Dallas, and Appendix G gives all the masks designed for this work. In chapter 5, A 2.4 GHz patch was used to build an 8-patch UCAs to demonstrate the OAM radio communication link. This research achieved the following results:

- Developed OAM-UCA factor under the cylindrical coordinate system, and based on it, developed a method to verify the purity of the OAM mode generated by UCAs.

- Generated OAM modes 1 and 3 using 8- and 12-dipole UCA at the lower E-band (71-76 GHz).

- Generated OAM mode 1 using 4-dipole UCA with series and corporate feed networks at the lower E-band.

- Without disturbing the OAM mode in the forward direction, developed a simple method to remove the backside radiation of the 8-dipole UCA for OAM mode 1 and enhance the radiation gain at the same time.

- Generated OAM mode +1, +2, and -3 at 67 GHz on TerraGreen® substrate using 4-, 8-, and 16-patch UCA respectively to reduce power division loss to the antennas.

- Demonstrated the OAM based radio communication link using 2.4 GHz 8-patch UCAs. Developed a better understanding of the OAM mode isolation and the obstacles of the OAM radio communication link.

6.2 Future work

The work presented herein shows the potential for verifying the OAM modes generated using UCAs and characterizing the array gain. This is an important first step in estimating path loss for a wireless communication system. Although not discussed in this dissertation the challenges associated with OAM communication are being considered from the software and modeling perspective [34].

In Chapter 5, 2.4 GHz patches were used to build the OAM-UCA and performed the demo for OAM radio communication verification. However, due to the fact that the frequency is 2.46 GHz, and correspondingly, the UCA radius to the wavelength ratio is only $0.73\lambda_0$ at 2.46 GHz, the radiation divergent angle is large, which would cause serious multipath effects even in a short distance. Secondly, the divergent angle is 22° in theory, but over 30° is observed in the H-cut (Figure 5.11). This is probably caused by the 2.46 GHz patch size on FR4 board is relatively large for the UCA radius (40 mm / 88.5 mm = 0.45). So the individual patch in the

UCA cannot be taken as an ideal radiating point as the one in theory. Future work can include shifting the demo to higher frequencies to reduce the patch size and provide a larger radius to decrease patch size to the UCA radius ratio. The 5G WiFi band is a reasonable option.

Secondly, in Chapter 2, a method for the OAM mode purity verification was developed, and some of the samples' OAM mode purity were also measured using the method. The accuracy is highly dependent on the resolution of the measurement phase and amplitude result exported from the chamber. Also, the algorithm cannot locate the radiating center automatically, and for now, the center has to be located manually. For example, Figure 6.1 shows the mode purity verification results using the chamber measurement data for the 8-dipole UCA with the reflector. The center is off from the field plane center, it needs manually locate the radiation center and only gives 14.5% mode purity. Figure 6.2 shows the OAM mode purity verification result by using the chamber measurement data for the 16-patch UCA for OAM mode -3. It also suffers from the issue of locating the radiation center, and only gives 26.2% mode purity. Therefore, I propose to develop a code that can locate the center automatically and be less dependent on the resolution of the exported data. Then one can check all current samples for the OAM mode purity.
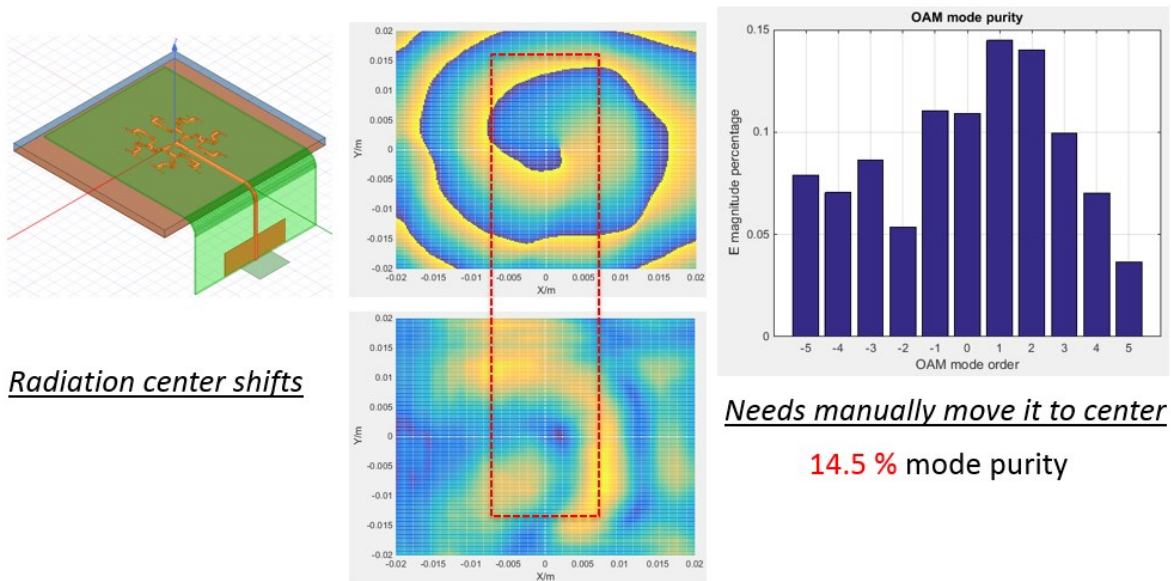
Figure 6.1. The OAM mode purity verification results using the chamber measurement data for the 8-dipole UCA with the reflector.
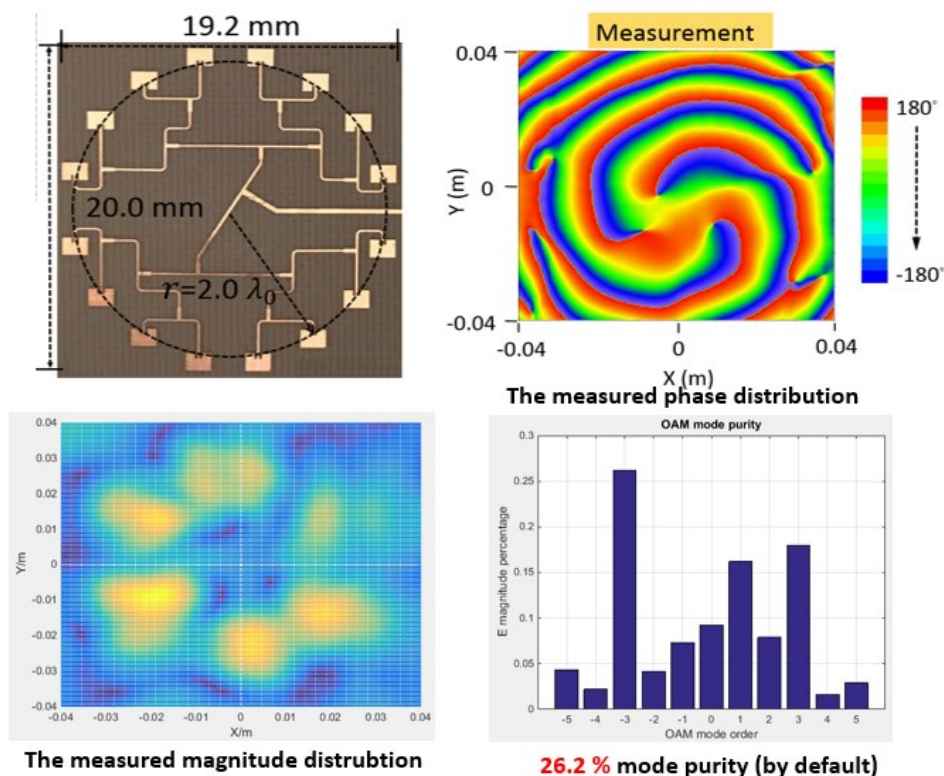
Figure 6.2. The OAM mode purity verification results using the chamber measurement data for the 16-patch UCA for OAM mode -3.

In summary, there are two major future works:

1. Design a 5.3 GHz or 5.6 GHz (WiFi 5G band) patch antenna on FR4 board, and build the same radius OAM-UCA and the feed network with the 2.4 GHz one, which would provide us the UCA radius to wavelength ratio of 1.65 and the patch size to UCA radius ratio of 0.19 @ 5.6 GHz. By doing that, the smaller divergent angle and less multipath effect can be expected, and then verify the link performance again.

2. Update the OAM mode purity verification algorithm to automatically center the measured phase and magnitude. Check the OAM mode purity of all the fabricated samples.

APPENDIX A

THE MATLAB CODE FOR OAM-UCA FACTOR UNDER THE CYLINDRICAL

COORDINATE SYSTEM

A.1. The summation form OAM-UCA factor

```matlab
%function OAM_UCA_factor_cylindrical_sum_form
% this is using the initial summation form factor to calculate E
field
clear all;
close all;
clc;
double all;
freq=67;% in GHz.
WL=300/freq; % vacuum wavelength in mm.
a=2.0*WL; % UCA radius.
N=16; % elements number.
z=15*WL; % distance between the UCA to the field plane.
k=2*pi/WL; % wave number, 2*pi / wavelength.
phi=[0:1:360]*pi/180; % phi angle.
l=3; % OAM mode number;
r = linspace(0,40,length(phi)); % observation field plane
radius, in mm;
phi_p=linspace(0,360-360/N,N); % element position angle
phi_p=pi*phi_p/180; % convert it to radian.
phi_a=phi_p; % additive phase of each element.
X=r'*cos(phi);
Y=r'*sin(phi);
E=0;

for i=1:1:N
    R=sqrt(a^2+z^2+(r.^2)'*ones(1,length(phi))-2*a*(r'*cos(phi-
phi_p(i))));
    E=E+exp(1j*k*R)./R*exp(-1j*l*phi_a(i));
end
E=E/N; % to normalize the E field

figure; % plot phase
mesh(X,Y,angle(E)*180/pi);
xlabel('X (mm)');
ylabel('Y (mm)');
```

```matlab
set(gca,'FontSize',14);
colorbar;

EE=E.*conj(E);
figure; % plot the magnitude
mesh(X,Y,EE/max(max(EE)),'FaceAlpha',0.5);
xlabel('X (mm)');
ylabel('Y (mm)');
zlabel('Normalized Amplitude of E field')
set(gca,'FontSize',14);
colorbar;

figure; % plot the gain pattern
plot(r,10*log10(EE(:,floor(0.5*length(phi))+1)/max(max(EE))),'li
newidth',2,'color','b');
ylim([-50 0]);
set(gca,'FontSize',14);
xlabel('Observation plane radius / mm');
ylabel('Normalized Gain / dB');
grid on;

figure; % plot the normalized gain over the theta angle.
Theta = asin(r./sqrt(r.^2+z^2))*180/pi;
plot(Theta,10*log10(EE(:,floor(0.5*length(phi))+1)/max(max(EE)))
,'linewidth',2,'color','b');
hold on;
plot(-
Theta,10*log10(EE(:,floor(0.5*length(phi))+1)/max(max(EE))),'lin
ewidth',2,'color','b');
set(gca,'FontSize',14);
xlabel('Theta / degree');
ylabel('Normalized Gain / dB');
ylim([-50 0]);
grid on;
```

A.2. The integral form OAM-UCA factor

```matlab
%function OAM_UCA_factor_cylindrical_integral_form
clear all;
close all;
clc;
double all;
freq=73;% in GHz.
```

```matlab
WL=300/freq; % vacuum wavelength in mm.
a=0.8*WL; % UCA radius, for 8 elements UCA;
N=8; % elements number.
z=6.57*WL; % far field range.
k=2*pi/WL; % wave number, 2*pi / wavelength.
phi=[0:1:359]*pi/180; % phi angle.
l=1; % OAM mode number;
r = linspace(0,20,length(phi)); % observation field plane
radius, in mm;
% convert to X,Y coordinates
X=r'*cos(phi);
Y=r'*sin(phi);
D=sqrt(z^2+r.^2);
E=-(1j)^l*(exp(-1j*k*D)./D.*besselj(l,k*a*r./D))'*exp(-
1j*l*phi); % UCA array factor divide by N.

E=E/max(max(abs(E))); % normalize E field

figure; % plot phase
mesh(X,Y,angle(E)*180/pi);
xlabel('X (mm)');
ylabel('Y (mm)');
set(gca,'FontSize',14);
colorbar;

figure; % plot magnitude
mesh(X,Y,E.*conj(E)/max(max(E.*conj(E))));
xlabel('X (mm)');
ylabel('Y (mm)');
zlabel('Normalized Amplitude of E field')
set(gca,'FontSize',14);
```

THE ANSYS HFSS SIMULATION SETUP IN FIGURE 2.9

The 73 GHz patch antenna on 0.127 mm FR408 material is used to simulate the UCA performance as the comparison of MATLAB UCA factor simulation. The patch is inset feed with the input impedance of 75 Ω, and a 75 Ω lumped port is used to excite it. Figure B.1 shows the single patch size, and Figure B.2 shows the patch UCA with the ideal feed setup for OAM mode 1 generation.
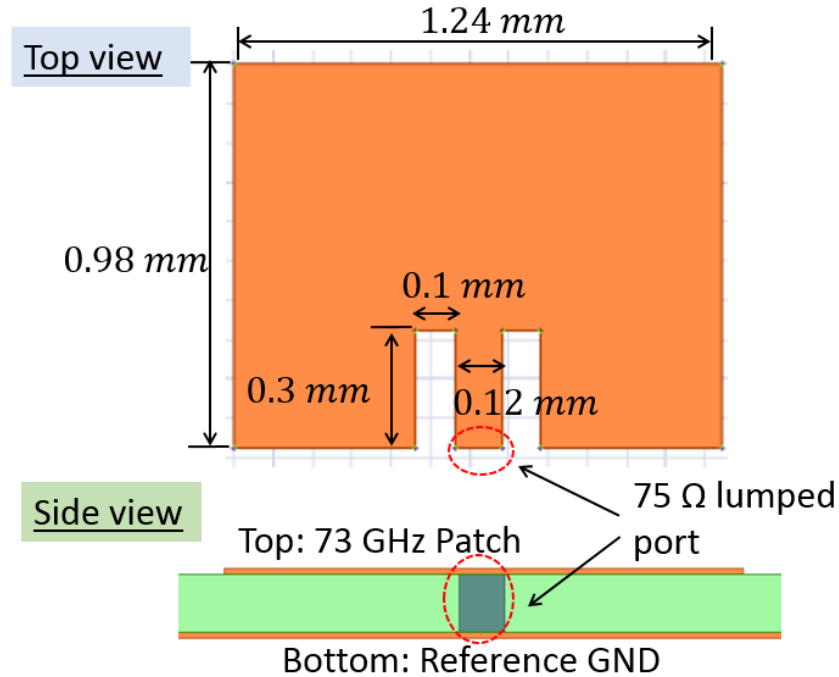
Figure B.1. The 73 GHz patch antenna size illustration on 0.127 mm FR408 substrate.
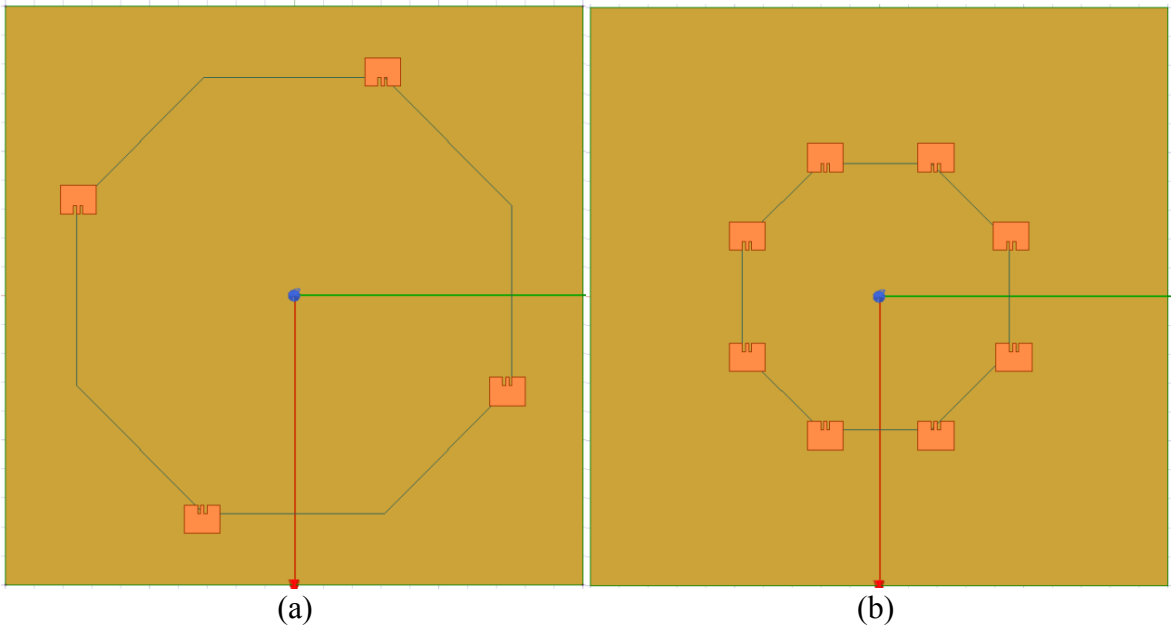
Figure B.2. The patch UCA with ideal feed setup for OAM mode 1 generation: (a) 4-patch UCA; (b) 8-patch UCA.

APPENDIX C

OAM MODE PURITY VERIFICATION MATLAB CODE

```matlab
clear all;
close all;
clc;
double all;
freq=67;% in GHz.
WL=300/freq; % vacuum wavelength in mm.
a=2.0*WL; % UCA radius.
N=4; % elements number.
z=15*WL; % distance between the UCA to the field plane.
k=2*pi/WL; % wave number, 2*pi / wavelength.
phi=[0:1:360]*pi/180; % phi angle.
l=1; % OAM mode number;
r = linspace(0,100,length(phi)); % observation field plane
radius, in mm;

phi_p=linspace(0,360-360/N,N); % element position angle
phi_p=pi*phi_p/180; % convert it to radian.
phi_a=phi_p; % additive phase of each element.

% convert to X,Y coordinates
X=r'*cos(phi);
Y=r'*sin(phi);
E=0;

% verification ends
for i=1:1:N
    R=sqrt(a^2+z^2+(r.^2)'*ones(1,length(phi))-2*a*(r'*cos(phi-
phi_p(i))));
    E=E+exp(1j*k*R)./R*exp(-1j*l*phi_a(i));
end
E=E/N; % to normalize the E field

figure;% plot phase
mesh(X,Y,angle(E)*180/pi);
xlabel('X (mm)');
ylabel('Y (mm)');
set(gca,'FontSize',14);
colorbar;
```

```matlab
EE=E.*conj(E);
figure;% plot the magnitude
mesh(X,Y,EE/max(max(EE)),'FaceAlpha',0.5);
xlabel('X (mm)');
ylabel('Y (mm)');
zlabel('Normalized Amplitude of E field')
set(gca,'FontSize',14);
colorbar;

figure; % plot the gain pattern
plot(r,10*log10(EE(:,floor(0.5*length(phi))+1)/max(max(EE))),'li
newidth',2,'color','b');
ylim([-50 0]);
set(gca,'FontSize',14);
xlabel('Observation plane radius / mm');
ylabel('Normalized Gain / dB');
grid on;

figure; % plot the normalized gain over theta angle.
Theta = asin(r./sqrt(r.^2+z^2))*180/pi;
plot(Theta,10*log10(EE(:,floor(0.5*length(phi))+1)/max(max(EE)))
,'linewidth',2,'color','b');
hold on;
plot(-
Theta,10*log10(EE(:,floor(0.5*length(phi))+1)/max(max(EE))),'lin
ewidth',2,'color','b');
set(gca,'FontSize',14);
xlabel('Theta / degree');
ylabel('Normalized Gain / dB');
ylim([-50 0]);
grid on;

%de-modulation or check the purity /Fourier transform to check
the purity.
ratio=[];
OAM_mode=[];
for i=-10:1:10
OAM_L=i;
Phase_2=ones(length(r),1)*OAM_L*[-360:1:0]*pi/180; % the OAM
phase mask.

delta=E.*exp(+1j*Phase_2); % the whole E field pass the mask
ratio_l=abs(sum(sum(delta))); % calculate the ratio of the
% total E_magnitude of field passing the mask over the total
E_mag of
```

```matlab
% original field.
OAM_mode=[OAM_mode i];
ratio=[ratio ratio_l];
end
ratio=ratio/sum(ratio); % normalize to the observation plane
raius, since the E_mag is integral over phi plane, if not
normalize the each r value will have
% one E_mag,

figure;
bar(OAM_mode,ratio);
title('OAM mode purity');
ylabel('E magnitude percentage');
xlabel('OAM mode order');
grid on;
set(gca,'FontSize',14);
```

APPENDIX D

UCA SAMPLE ETCHING PROCESS IN THE UTD CLEANROOM

D.1. Patch UCA fabrication process (Single side etching)

1. Clean the samples/substrates

   a. Rinse with acetone and IPA and dry with N2 at the solvent hood or use the automated program on the CPK Solvent Spinner.

   b. Dehydrate bake @ 130 °C for 2 min.

2. HMDS-Place the samples in the HMDS oven to apply the HMDS which is utilized to improve adhesion of photoresist to the sample.

3. Lithography

   a. Spin S1813 photoresist on the backside ground to achieve a thickness of 1.5 μm using the open-hood spinner @ 3000 RPM with 3000 RPM/s for 60 sec.

   b. Soft-bake on the hotplate at 115°C for 90 sec.

   c. Place the sample on a carrier wafer such as glass or silicon using tape at the corners.

   d. Spin S1813 photoresist on the topside ground to achieve a thickness of 1.5 μm using the open-hood spinner @ 3000 RPM with 3000 RPM/s for 60 sec.

   e. Soft-bake on the hotplate at 115 °C for 90 sec.

   f. Expose the topside of the substrates using a chrome mask on the Karl Suss with a dosage of 110mJ/cm^2.

   g. Remove the substrates from the carrier wafer.

   h. Hand-develop the resist using MF319 developer for 65 sec.

   i. RIE at 50 W,180m Torr,O$_2$ for 15 sec.

j. Hard bake on the hotplate at 130°C for 60 sec.

4. Examine the samples under the microscope. The photoresist should be present wherever the desired pattern is located. The lines should be sharp and the sample should be clean.

5. Etch the samples using MGC ferric chloride solution at room temperature in a beaker with constant steady motion until copper is removed in unwanted areas. This process takes approximately 5 min.

6. Rinse with DI water and N_2 dry.

7. Strip the PR using acetone or the automated spinner.

8. Rinse with DI water and N_2 dry.

9. Dehydrate bake at 130 °C for 5 min.

10. Examine the samples under the microscope and measure dimensions. Desired features/structures should be realized.

D.2. Dipole UCA fabrication process (Double-sided etching).

1. Clean the samples/substrates

    a. Rinse with acetone and IPA and dry with N2 at the solvent hood or use the automated program on the CPK Solvent Spinner.

    b. Dehydrate bake @ 130 °C for 2 min.

2. HMDS-Place the samples in the HMDS oven to apply the HMDS which is utilized to improve adhesion of photoresist to the sample.

3. Lithography

    a. Spin S1813 photoresist on the backside ground to achieve a thickness of 1.5 μm using the open-hood spinner @ 3000 RPM with 3000 RPM/s for 60 sec.

b. Soft-bake on the hotplate at 115°C for 90 sec.

c. Place the sample on a carrier wafer such as glass or silicon using tape at the corners.

d. Spin S1813 photoresist on the topside ground to achieve a thickness of 1.5 μm using the open-hood spinner @ 3000 RPM with 3000 RPM/s for 60 sec.

e. Soft-bake on the hotplate at 115 °C for 90 sec.

f. Expose the topside of the substrates using a chrome mask on the Karl Suss with a dosage of 110mJ/cm^2.

g. Remove the substrates from the carrier wafer.

h. Hand-develop the resist using MF319 developer for 65 sec.

i. RIE at 50 W,180m Torr,O_2 for 15 sec.

j. Hard bake on the hotplate at 130 °C for 60 sec.

4. Examine the samples under the microscope. The photoresist should be present wherever the desired pattern is located. The lines should be sharp and the sample should be clean.

5. Etch the samples using MGC ferric chloride solution at room temperature in a beaker with constant steady motion until copper is removed in unwanted areas. This process takes approximately 5 min.

6. Rinse with DI water and N_2 dry.

7. Strip the PR using acetone or the automated spinner.

8. Rinse with DI water and N_2 dry.

9. Flip the sample, repeat step 3 and 4 again, but this time one needs to make sure the bottom layer pattern should be aligned perfectly with the etched top layer, this can only be done by using the Karl Suss exposure machine with the corresponding handling plate.

10. Top layer (the etched layer) protection using Su8 photoresist

This step shall be done before etching.

a. Place the sample (the etched layer faces the top) on a carrier wafer such as glass or silicon, make sure Su8 will not get into the bottom layer, use tape to tape at all the edges to the carrier wafer.

b. Spin Su8-2075 on the etched top layer at 500 RPM for 10 seconds with the acceleration of 100 RPM/s at first, then spin at 1800 RPM for 30 seconds with the acceleration of 300 RPM/s, this is for forming a 125 um thickness Su8 protection layer (or spin Su8-2025 at 500 RPM for 10 seconds with the acceleration of 100 RPM/s at first, then spin at 3000 RPM for 30 seconds with the acceleration of 300 RPM/s, for forming a 25 um protection layer).

c. Planarization for 1 hr.

d. Soft bake 5 minutes at 65 °C and then soft bake 30 minutes at 95 °C (For the thinner protection layer, the bake time can be shortened to 5 minutes).

Note: baking is for hardening the Su8 protection layer, soft bake is enough, and it should not be too long, otherwise, the Su8 protection layer would be fragile, easy to break during the etching process.

e. Observe it using Microscope to check the bottom S1813 patter, make sure it is not melted. This is another consideration to use a time-limited soft bake to harden the Su8 layer.

11. Repeat step 5, and then check it using microscope. If there is still copper left in the gap of CPW structure (if one has), another 90 seconds are used to remove the metal there (30 s +30 s +15 s +15 s), and the sample size is about 2.0 cm × 2.0 cm.

12. Rinse with DI water and N_2 dry.

13. Strip the PR and Su8 protection layer using acetone or the automated spinner.

14. Rinse with DI water and N_2 dry.

15. Dehydrate bake at 130 °C for 5 min.

16. Examine the samples under the microscope and measure dimensions. Desired features/structures should be realized.

APPENDIX E

THE LOSS ANALYSIS OF 50-OHM MICROSTRIP LINE ON ISOLA TERRAGREEN® SUBSTRATE AND 1890-04-6 END-LAUNCH CONNECTOR FROM SOUTHWEST MICROWAVE INC.

To analyze the 50-ohm microstrip line loss on Isola TerraGreen® substrate, two 50-Ω microstrip lines were fabricated in UT Dallas cleanroom, one is with a length of 36.5 mm, and the other is 25.0 mm. Two end-launch connectors from Southwest Microwave Inc. (Model #: 1890-04-6) were utilized to take the measurement. Figure E.1 shows the two-port measurement result of the 36.5 mm microstrip line, and the 25.0 mm microstrip line result is shown in Figure E.2. With the two end-launch connectors, at 67 GHz, the insertion loss of the 36.5 mm microstrip line is 5.718 dB, and the 25.0 mm one has 4.776 dB loss. Therefore, for the 11.5 mm microstrip line, its loss is 0.942 dB, and correspondingly the unit length loss is 0.082 dB/mm at 67 GHz. For the 1890-04-6 end-launch connector, based on the measured results, the loss would be 1.36 dB at 67 GHz.
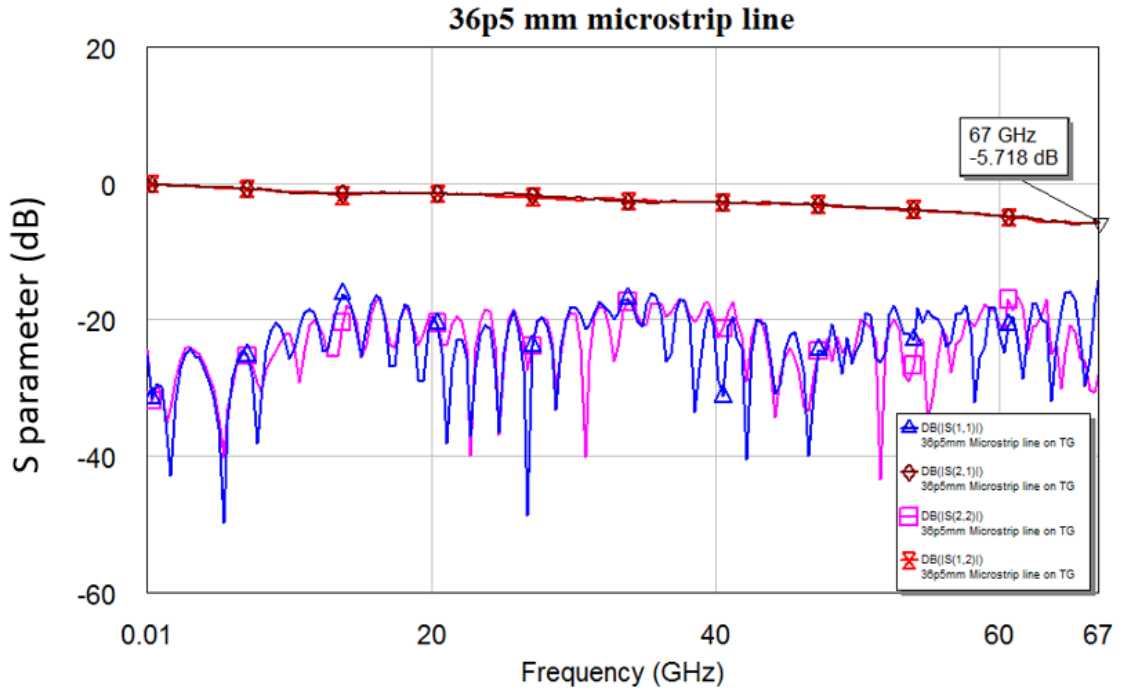
Figure E.1. The two-port measurement result of the 36.5 mm 50-ohm microstrip line on TerraGreen® substrate.
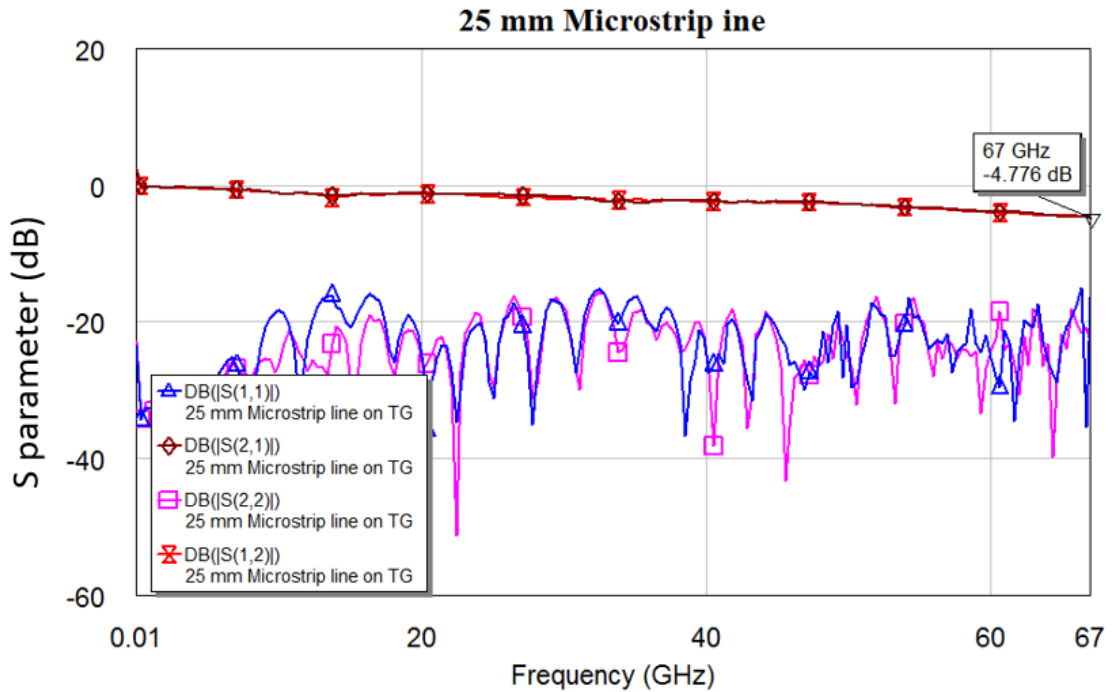
Figure E.2. The two-port measurement result of the 25.0 mm 50-ohm microstrip line on TerraGreen® substrate.

APPENDIX F

THE PLANAR CHAMBER MEASUREMENT SETUP

1. Open-Ended Wave Guide (OEWG) Selection:

The OEWG should be chosen based on the AUT working frequency. Here, in order to measure the horn antenna working at 9.2 GHz, the OEWG whose working frequency range from 8.2 GHz to 12.4 GHz was chosen, and it is shown in Figure F.1.

Figure F.1. 8.2 GHz to 12.4 GHz OEWG.

2. Install the OEWG:

Use hands and wrench to install the OEWG onto the scanner firmly (Figure F.2), and put the RF cable into the OEWG supporting structure, so that it will not touch the absorber's cone, or

it will cause unnecessary damage to the absorbers and the cable when the scanner moves up and down (Figire F.3).

Figure F.2. OEWG installation.

Figure F.3. Put the RF cable into the OEWG supporting structure.

3. Install OEWG absorber disc:

There are two absorber discs in our lab, choose the right disc based the OEWG size (working frequency). For low frequency, the absorber has larger cones and center hole, for

higher frequency, the cones and center hole are smaller. Figure F.4 shows the absorber disc working for higher frequency.
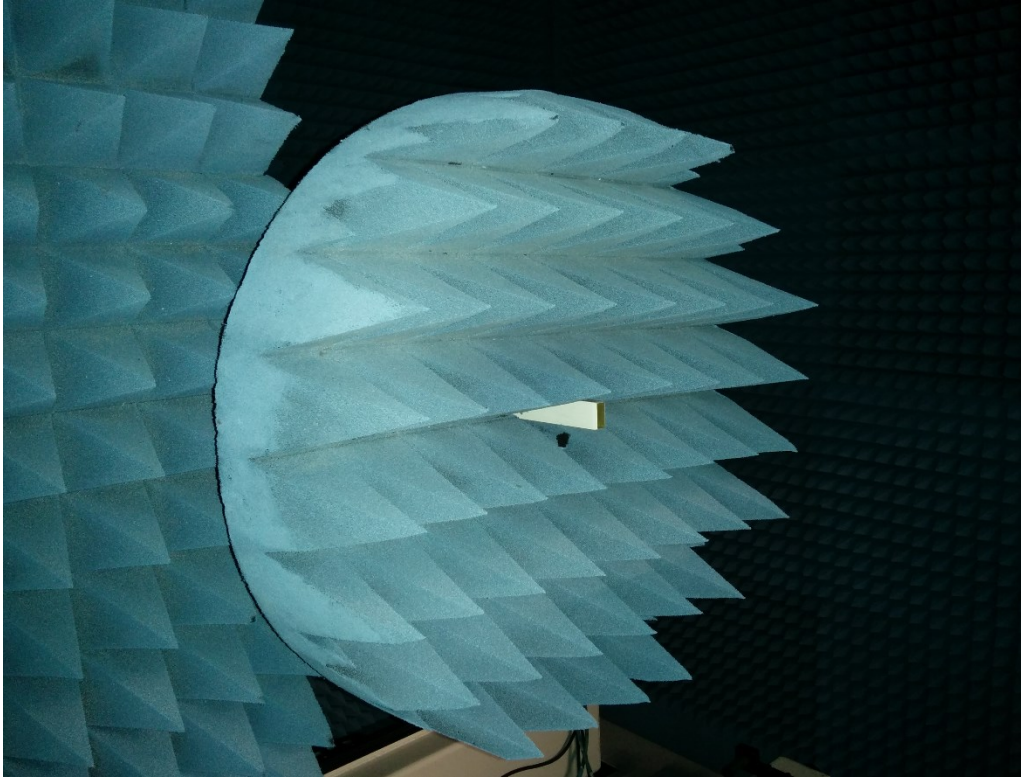
Figure F.4. Absorber disc working for higher frequency.

4. Mount the AUT onto the tripod:

Figure F.5 shows how to set up the AUT onto the tripod: Use tapes to make sure the AUT will 'sit' on tripod perfectly, and connect it to the RF cable with less bent.

5. Adjust the AUT location:

1>. Make sure the antenna main radiation direction (antenna aperture) face to the OEWG directly.

2>. Make sure the antenna polarization is the same or perpendicular to the OEWG polarization (Figure F.6).

3>. Make sure the initial height of the AUT is the same with OEWG (Figure F.6).

4>. Make sure the spacing between AUT and OEWG is 3 to 6 wavelengths (Figure F.7), to satisfy near field measurement requirement.
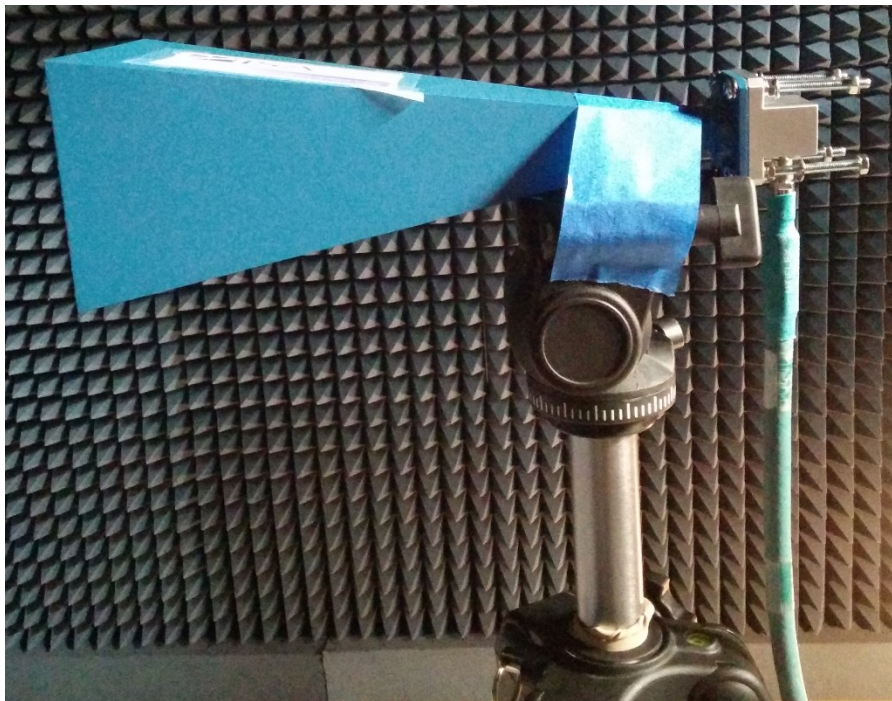
Figure F.5. AUT setup.
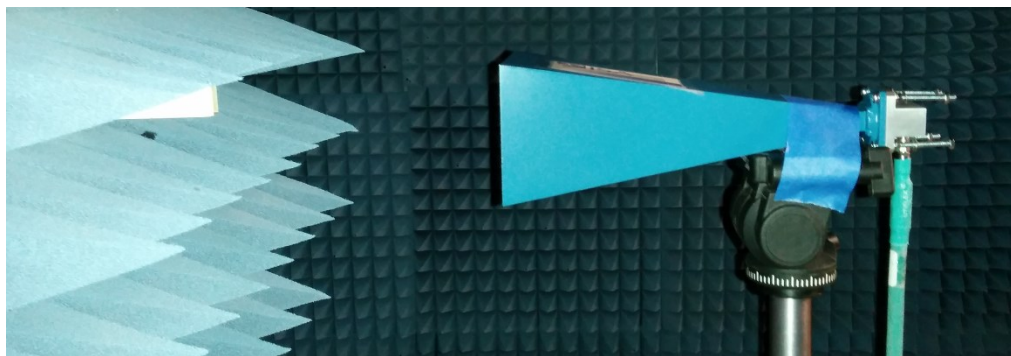
Figure F.6. Adjust the AUT height, polarization, and elevation angle.
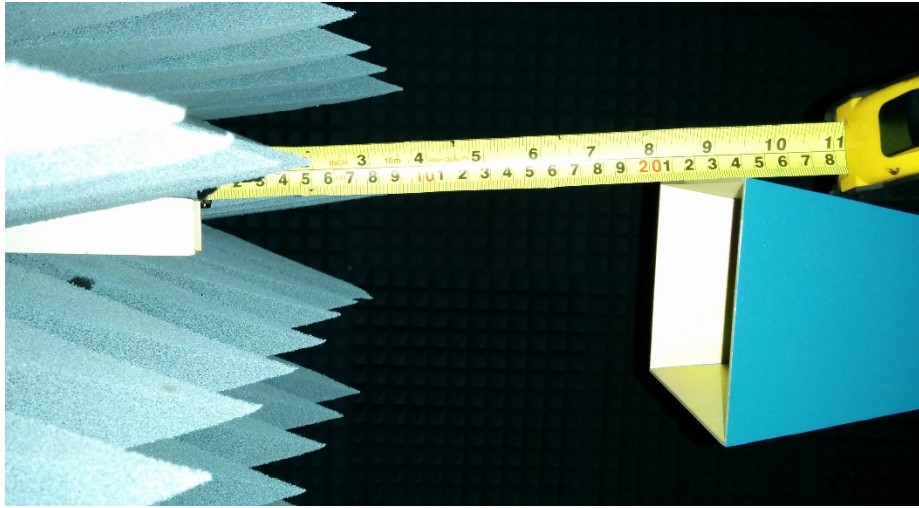
Figure F.7. Adjusting the spacing between OEWG and AUT, here is about 6 wavelength of 9.2 GHz.

APPENDIX G

THE MASKS DESIGNED FOR THE CLEANROOM FABRICATION

The first mask was designed by Chris Miller, a previous master student of our lab. This mask is realized in 2016, and the dipole antenna's top and bottom layer were realized in the center area with the alignment markers. This is mainly to verify the single 73 GHz dipole antenna performance on FR408 substrate material.
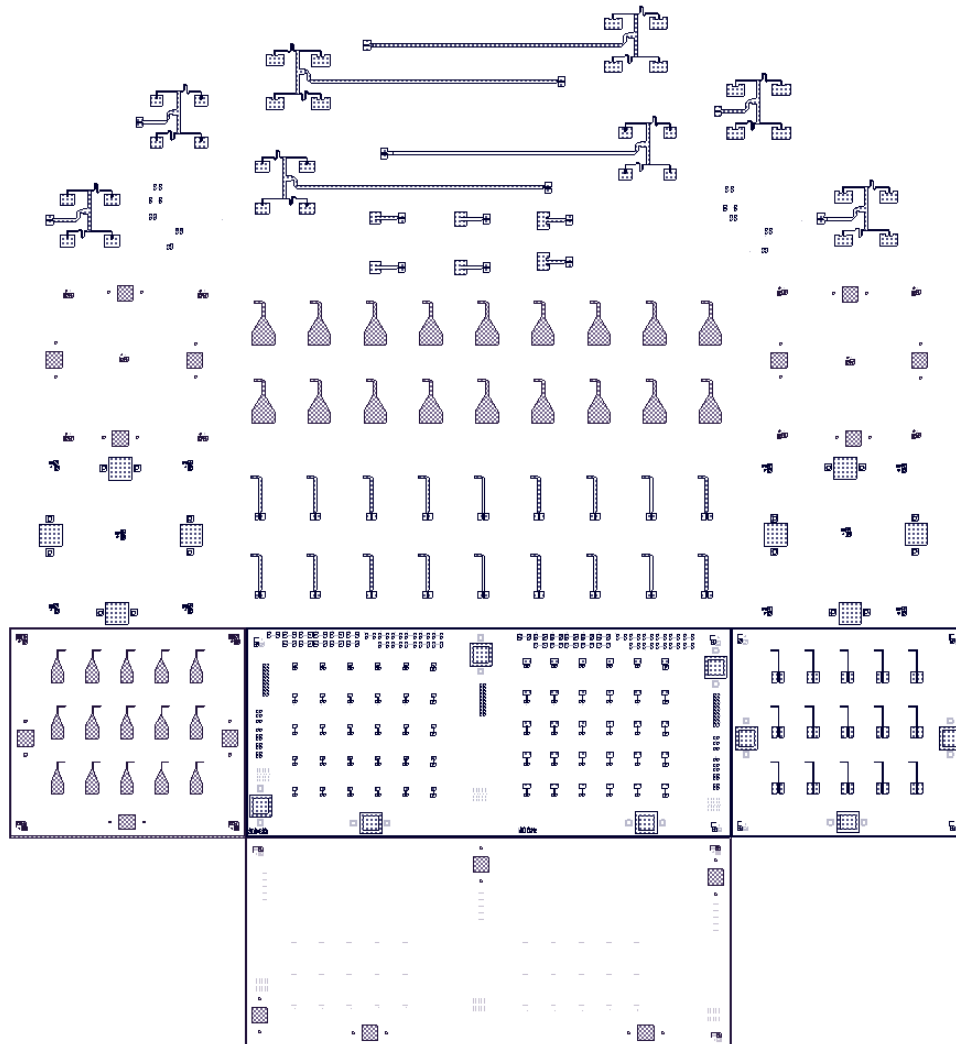
Figure G.1. The first mask for the single dipole antenna fabrication on FR408.

The second mask is designed by myself, which is for the 73 GHz 8-dipole UCA for OAM mode 1, and 12-dipole UCA for OAM mode 3. Two individual masks were utilized at that time: one is the bottom mask, which is shown in Figure G.2, the other one is the top mask, which is shown in Figure G.3. By horizontally flip the bottom mask, the two masks are aligned, and hence the correct sample would be realized. In these two masks, 3 levels of compensation for solving the over-etching issue were utilized, one is the 6 µm compensation, which is denoted as 0%. The second one is 8 µm compensation, which is denoted as 16 µm, and the last one is 12 µm compensation, which is denoted as 10%.
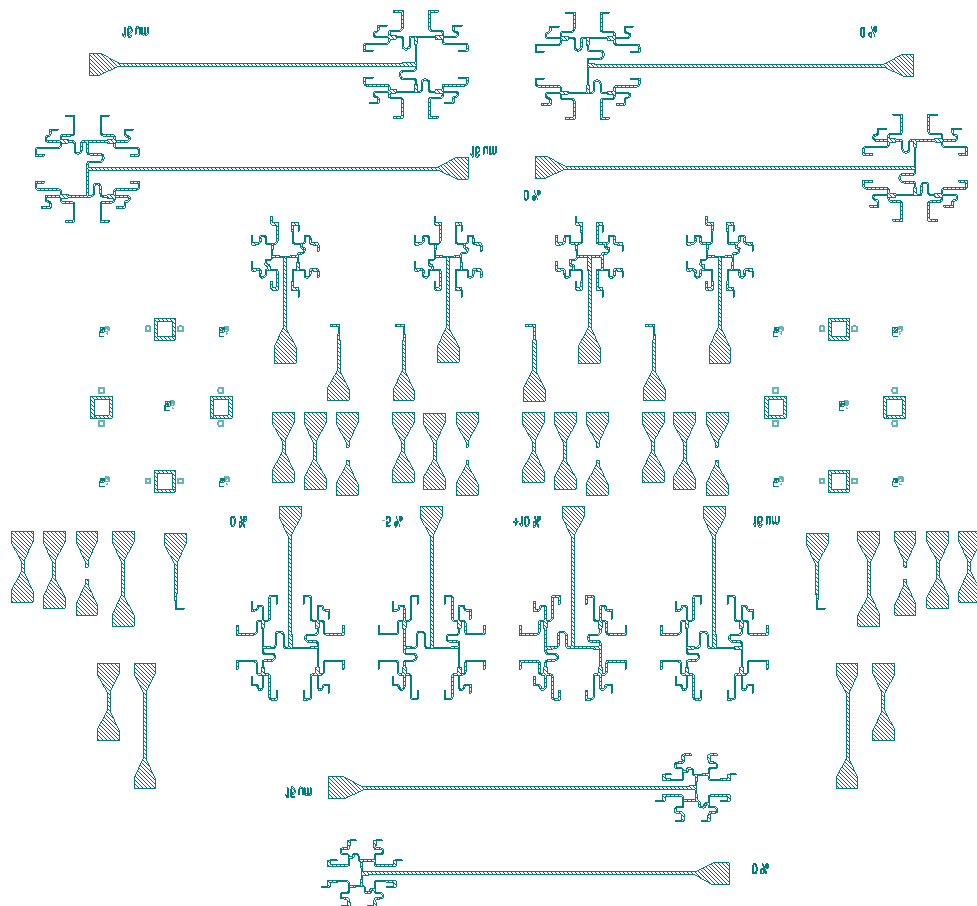
Figure G.2. The second mask (bottom) for the 73 GHz dipole UCA fabrication on FR408.
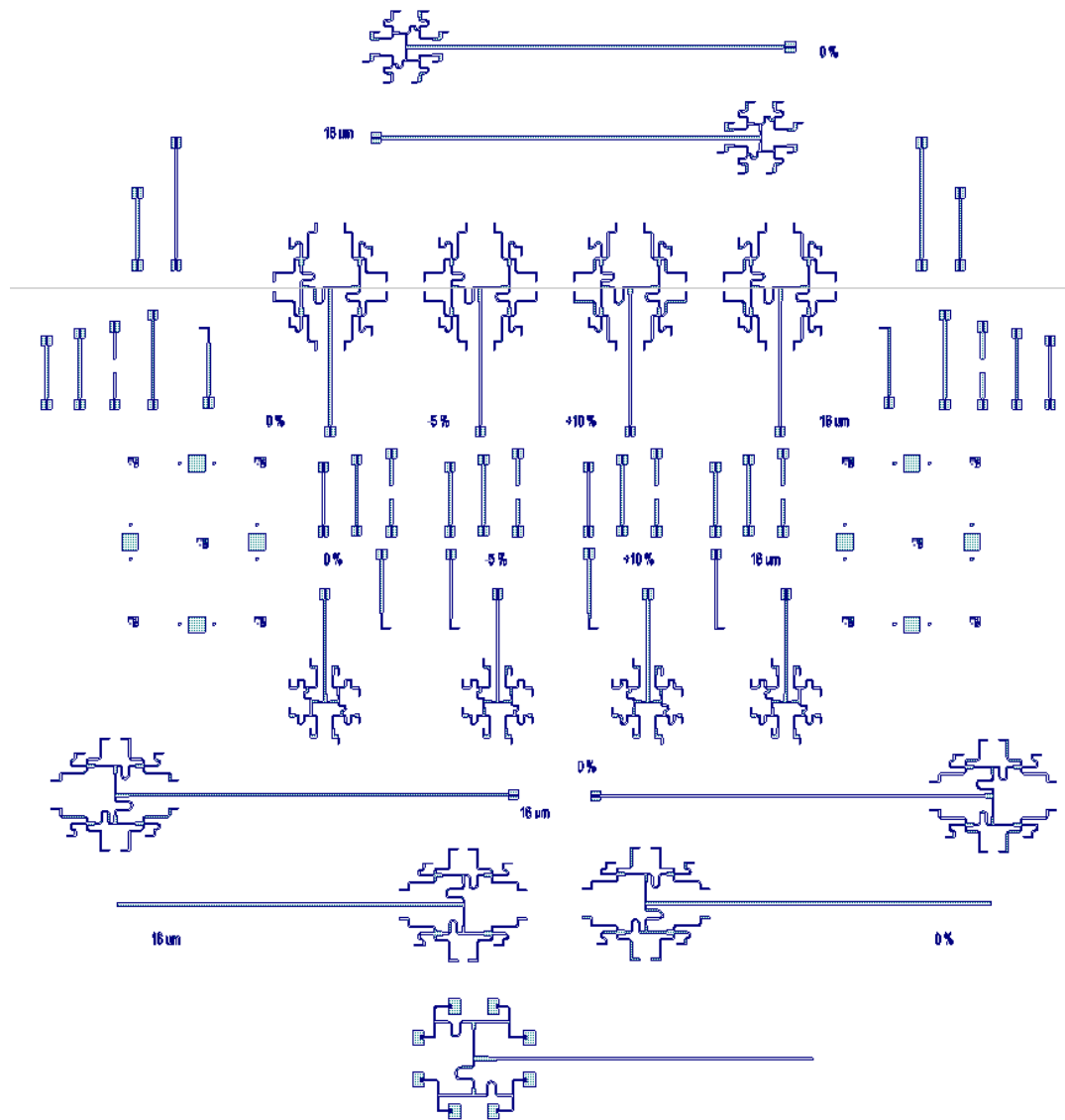
Figure G.3. The second mask (top) for the 73 GHz dipole UCA fabrication on FR408.

The third mask was also designed by myself, which was realized in 2017. This mask is for the verification of 73 GHz patch UCA on FR408 substrate. Secondly, the CBCPW top ground pad length effect was also investigated. Thirdly, the feed structure loss was investigated by using the back to back (B2B) structures.
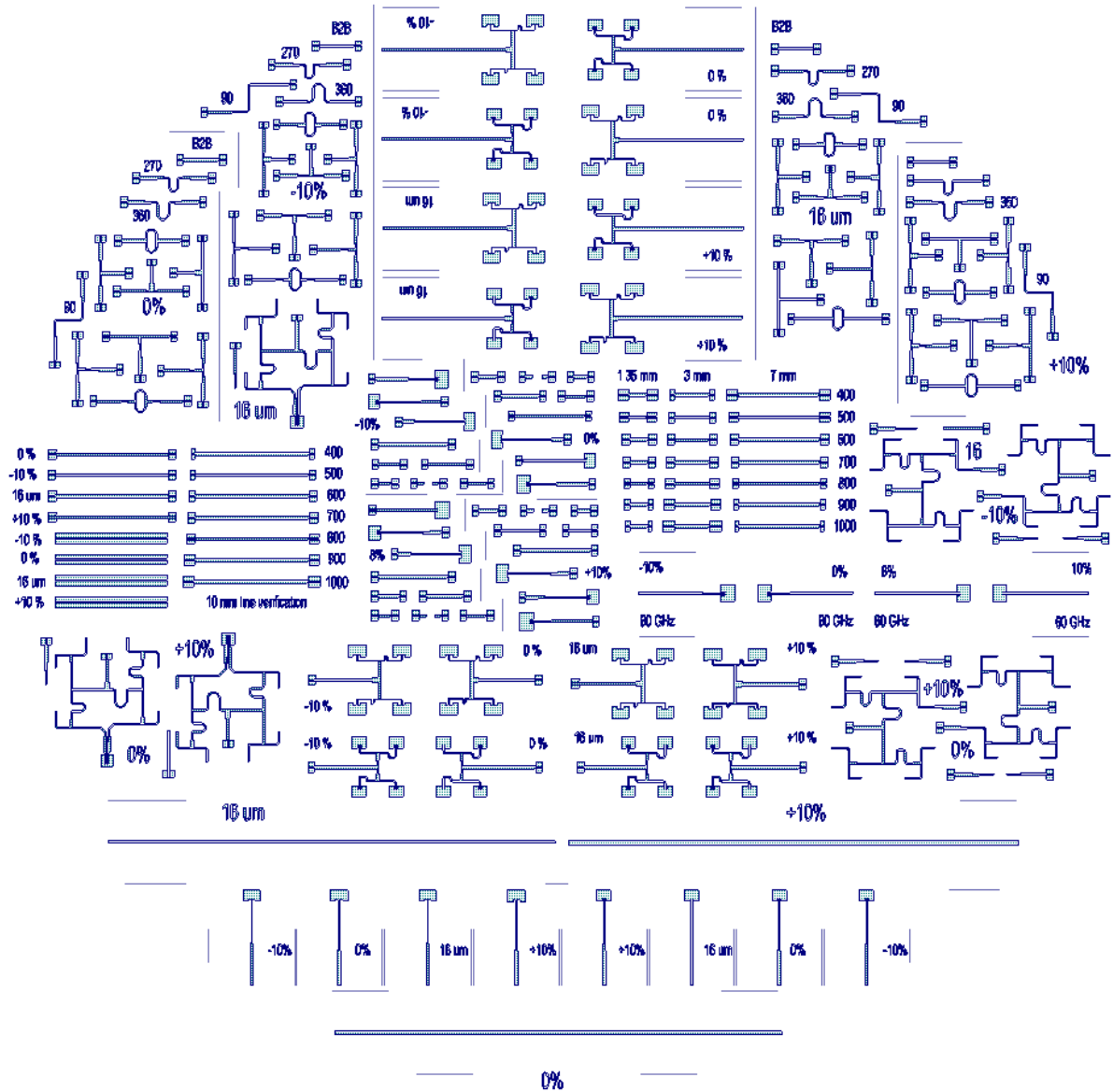
Figure G.4. The third mask for the 73 GHz patch UCA fabrication on FR408.

The fourth mask was designed by myself and realized in 2017 too. This was mainly for the 4-dipole UCA at 73 GHz with series and corporate feed network on FR408 substrate. Again, a bottom and a top mask are utilized, and the CBCPW to DSPSL transition structures and 73 GHz patch UCA were also included in this mask.
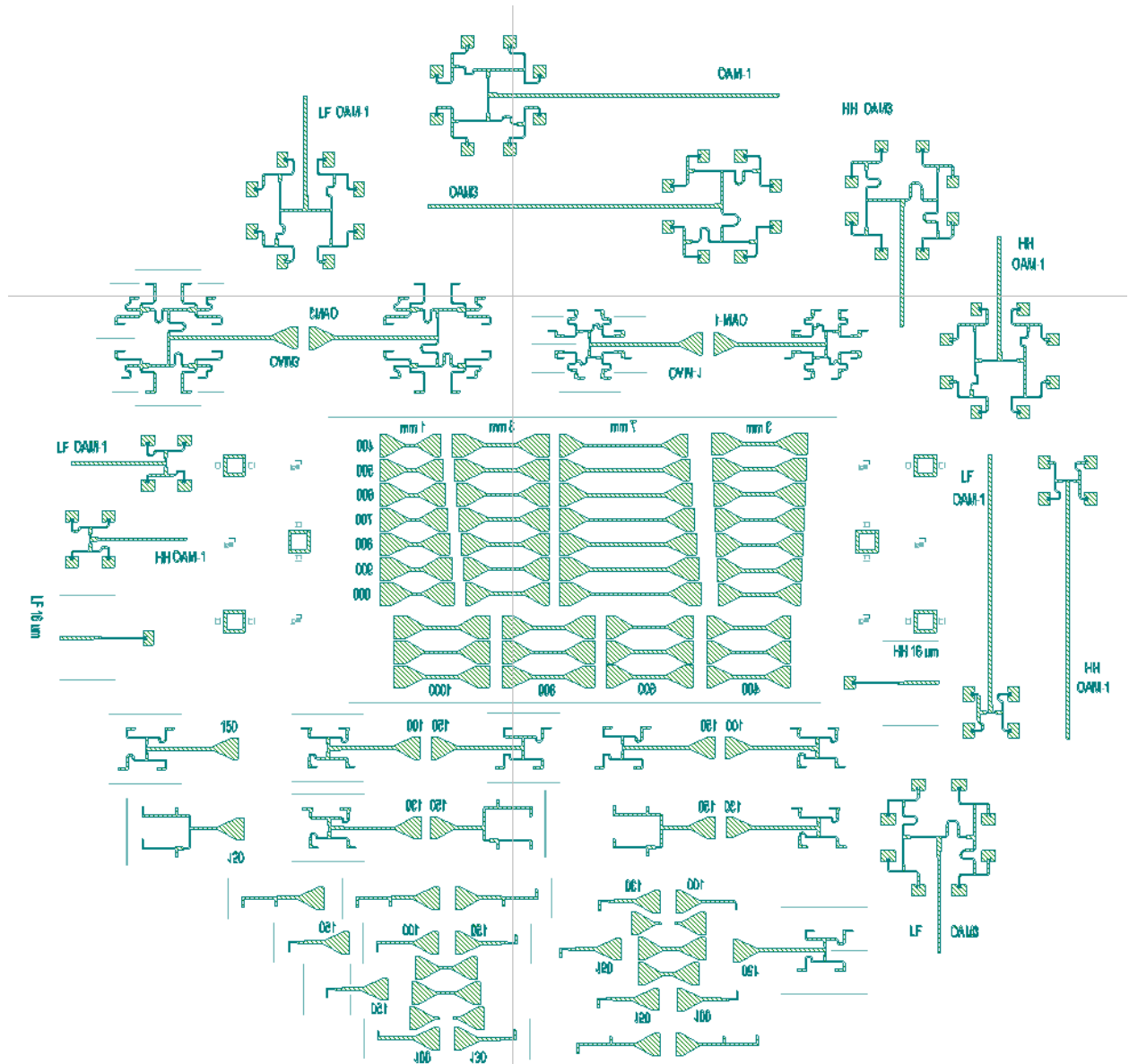
Figure G.5. The fourth mask (bottom) for the 73 GHz 4-dipole UCA fabrication on FR408.
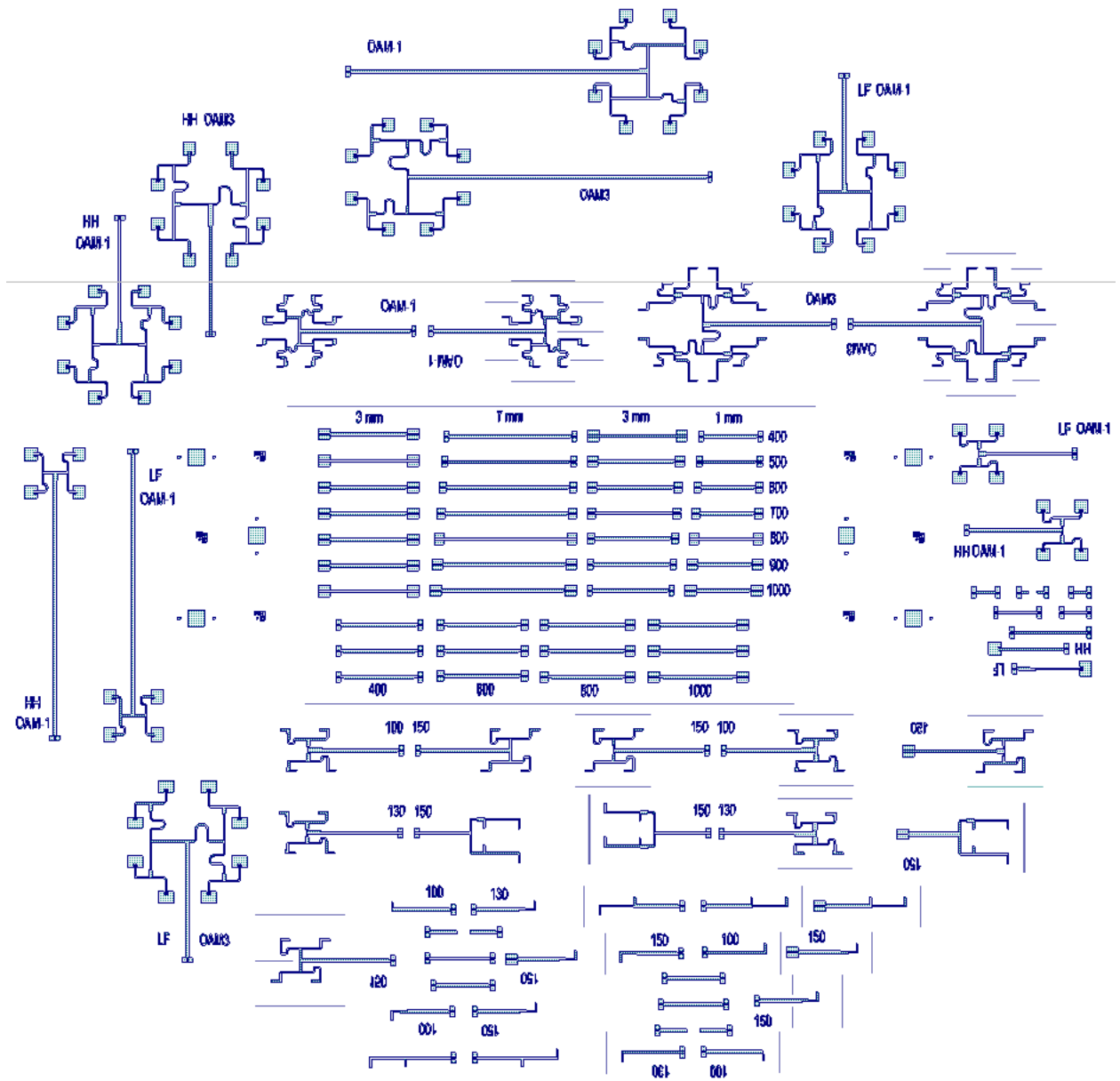
Figure G.6. The fourth mask (top) for the 73 GHz 4-dipole UCA fabrication on FR408.

The fifth mask was also designed by myself and realized in 2018. This was for the 67 GHz patch UCA on TerraGreen® substrate. Since TerraGreen® has 17μm copper clad, it needs more etching compensation, here 10% compensation stands for 24 μm compensation.
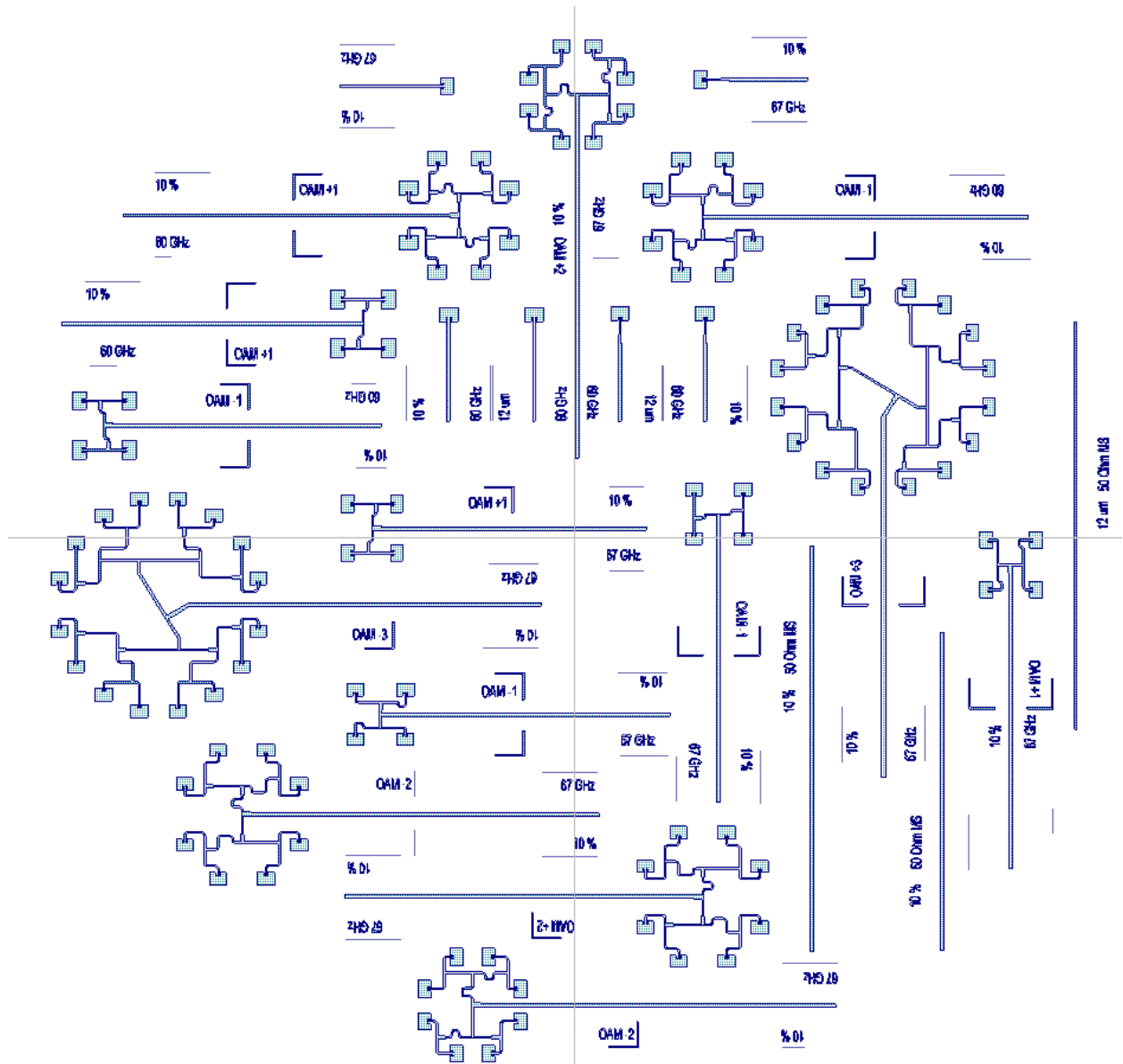
Figure G.7. The fifth mask for the 67 GHz patch UCA fabrication on TerraGreen® substrate.

REFERENCES

[1]   *What is 5G, Ericsson*, [Online]. Available: https://www.ericsson.com/en/5g/what-is-5g.

[2]   *The FCC's 5G FAST Plan*, Federal Communications Commission, [Online]. Available: https://www.fcc.gov/5G.

[3]   *70-80 GHz for 5G densification*, Nokia Corporation, Mar. 2019. [Online]. Available: https://ecfsapi.fcc.gov/file/1031939691008/Nokia%20FCC%20E-Band%20Preso%203-18-2019.pdf

[4]   A. E. Willner, et al. "Optical communications using orbital angular momentum beams," *Advances in Optics and Photonics*, 7(1), pp. 66-106, Mar. 2015.

[5]   Y, Yan, "High-capacity millimetre-wave communications with orbital angular momentum multiplexing," *Nature Communications*, vol. 5, Sep. 2014.

[6]   F. Tamburini, et al., "Encoding many channels on the same frequency through radio vorticity: first experimental test," *New Journal of Physics*, vol. 14, no. 3, Mar. 2012.

[7]   H. Sasaki et al., "Experiment on Over-100-Gbps Wireless Transmission with OAM-MIMO Multiplexing System in 28-GHz Band," *2018 IEEE Global Communications Conference (GLOBECOM)*, Abu Dhabi, United Arab Emirates, 2018, pp. 1-6.

[8]   D. Lee, H. Sasaki, H. Fukumoto, Y. Yagi, T. Kaho, H. Shiba, and T. Shimizu, "An Experimental Demonstration of 28 GHz Band Wireless OAM-MIMO (Orbital Angular Momentum Multi-input and Multi-output) Multiplexing," *Proc. of the 2018 IEEE 87th Vehicular Technology Conference (VTC 2018-Spring)*, Porto, Portugal, June 2018.

[9]   Pat Hindle, "Let's Talk 6G," *Microwave Journal*, Nov. 26, 2018. [Online]. Available: https://www.microwavejournal.com/blogs/9-pat-hindle-mwj-editor/post/31386-lets-talk-6g.

[10]   J. Sjöholm and K. Palmer, "Angular Momentum of Electromagnetic Radiation. Fundamental physics applied to the radio domain for innovative studies of space and development of new concepts in wireless communications," *M.S. thesis*, Dept. of Astronomy and Space Physics, Uppsala Univ., Uppsala, Sweden, 2007.

[11]   G. A. Turnbull, D. A. Robertson, G. M. Smith, L. Allen, and M. J. Padgett, "The generation of free-space Laguerre-Gaussian modes at millimeter-wave frequencies by use of a spiral phase plate," *Optics Communications*, 127, pp. 183-188, Jun. 1996.

[12]   C. Li, H. Wei. and ZC. Hao, "Generation of Electromagnetic Waves with Arbitrary Orbital Angular Momentum Modes," *Sci Rep 4*, 4814,2014.

[13]   H. Yao, et al., "Experimental Demonstration of a Dual-channel E-band Communication Link using Commercial Impulse Radios with Orbital Angular Momentum Multiplexing," *presented at the 2017 IEEE RWS*, Phoenix, AZ, Jan. 15-18, 2017.

[14]   A. Tennant and B. Allen, "Generation of OAM radio waves using circular time-switched array antenna," *Electronics Letters*, vol. 48, no. 21, pp. 1365-1366, Oct. 2012.

[15]   C. Sun, et al., "Realization of multiple orbital angular momentum modes simultaneously through four-dimensional antenna arrays," *Scientific Reports*, vol. 8, no. 1. Dec. 2017, 10.1038/s41598-017-18264-3.

[16]   X. Bai, et al., "Design of a horn lens antenna for OAM generation," *IEEE International Symposium on Antennas and Propagation & USNC/URSI National Radio Science Meeting*, Vancouver, BC, 2015, pp. 2081-2082.

[17]   W. L. Wei, et al., "Generation of radio orbital angular momentum (OAM) waves with circular metallic waveguide," *2015 Asia-Pacific Microwave Conference (APMC)*, Nanjing, 2015, pp. 1-3.

[18]   M. Huang, X, Zong, and Z, Nie, "Horn Antenna Generating Electromagnetic Field with Orbital Angular Momentum," *Progress In Electromagnetics Research M*, Vol. 60, 57–65, 2017.

[19]   W. Wei, et al., "Horn antennas for generating radio waves bearing orbital angular momentum by using spiral phase plate," in *IET Microwaves,* Antennas & Propagation, vol. 10, no. 13, pp. 1420-1427, 10 22 2016.

[20]   W. Wei, et al., "Horn antenna for generating Orbital Angular Momentum (OAM) waves," *2015 Loughborough Antennas & Propagation Conference (LAPC)*, Loughborough, 2015, pp. 1-3.

[21]   Z. G. Guo and G. M. Yang, "Radial Uniform Circular Antenna Array for Dual-Mode OAM Communication," in *IEEE Antennas and Wireless Propagation Letters*, vol. 16, pp. 404-407, 2017.

[22]   D. Liu, L. Gui and M. R. Akram, "Generation of OAM radio waves using slot antenna array," *2015 Asia-Pacific Microwave Conference (APMC)*, Nanjing, 2015, pp. 1-3.

[23]   T. Yang, et al., "Experimentally Validated, Wideband, Compact, OAM Antennas Based on Circular Vivaldi Antenna Array," *Progress In Electromagnetics Research C*. Vol. 80, pp. 211-219, Jan. 2018.

[24]   Y. M. Zhang and J. L. Li, "Comments on "Radial Uniform Circular Antenna Array for Dual-Mode OAM Communication," in *IEEE Antennas and Wireless Propagation Letters*, vol. 17, no. 4, pp. 719-721, April 2018. doi: 10.1109/LAWP.2018.2811978.

[25]   Q. Bai, A. Tennant, and B. Allen, "Experimental circular phased array for generating OAM radio beams," *Electronics Letters*, vol. 50, no. 20, pp. 1414-1415, Sep. 2014.

[26]   Z. Zhao et al., "A dual-channel 60 GHz communications link using patch antenna arrays to generate data-carrying orbital-angular-momentum beams," *2016 IEEE International Conference on Communications (ICC)*, Kuala Lumpur, 2016, pp. 1-6.

[27]   Nippon Telegraph and Telephone Corporation, "NTT successfully demonstrates 100 Gbps wireless transmission using a new principle (OAM multiplexing) as a world's first," Tokyo, Japan, [Online]. Available: http://www.ntt.co.jp-/news2018/1805e/180515a.html.

[28]   C. A . Balanis, "Microstrip Antennas" *in Antenna theory and analysis and design*, 3rd edition, Hoboken, NJ, USA:John Wiley & Sons, Inc. 2005.

[29]   S. M. Mohammadi, L. K. S. Daldorff, J. E. S. Bergman, et al., "Orbital angular momentum in radio—a system study," *IEEE Transactions on Antennas and Propagation*, vol. 58, no. 2, pp. 565–572, 2010.

[30]   L. Fang, R. M. Henderson, "Orbital Angular Momentum Uniform Circular Antenna Array Design and Optimization-Based Array Factor," *Paper presented at the 2019 Texas Symposium on Wireless and Microwave Circuits & Systems*, Waco, TX, March 2019.

[31]   A.K. Jha et al., "Fourier relationship between the angle and angular momentum of entangled photons,". *Physical Review A*, 78 (4). 2008.

[32]   Y. Yan et al., "High-purity generation and power-efficient multiplexing of optical orbital angular momentum (OAM) modes in a ring fiber for spatial-division multiplexing systems," *2012 Conference on Lasers and Electro-Optics (CLEO)*, San Jose, CA, 2012, pp. 1-2.

[33]   L. Fang, H. Yao, R. M. Henderson, "OAM Antenna Arrays at E-Band," *Paper presented at the 27th International Microwave Symposium (IMS2017)*, Honolulu, HI, June 2017.

[34]   Harald T. Friis, "A Note on a Simple Transmission Formula," *Proceedings of the I.R.E. and Waves and Electrons*, May, 1946, pp 254–256.

[35]   C. A. Balanis, "Linear Wire Antennas," in *Antenna theory and analysis and design*, 3rd edition, Hoboken, NJ, USA: John Wiley & Sons, Inc. 2005.

[36]   L. Fang, R. M. Henderson, "Broadband Conductor-Backed Coplanar Waveguide to Double-Sided Parallel Strip Line Transition at Millimeter Wave," *Paper presented at the 2017 Texas Symposium on Wireless and Microwave Circuits & Systems*, Waco, TX, April 2017.

[37]   L. Fang, H. Yao, R. M. Henderson, "Design and Performance of OAM Modes Generated using Dipole Arrays with Different Feeds," *Paper presented at the 2018 Radio & Microwave Week (RWW2018)*, Anaheim, CA, January 2018.

[38]   L. Fang, R. M. Henderson, "Orbital Angular Momentum Generation Using Dipole Array with Reflector," *Paper presented at the 2019 European Microwave Week (EuMW2019)*, Paris, France, September 2019.

[39]   L. Fang, R. M. Henderson, "Millimeter-Wave OAM Dipole Array with Reflector," *Paper presented at the 53rd IEEE International Conference on Communications (ICC2019)*, Shanghai, China, May 2019.

[40]   A. Thakur and J. Berakdar, "Reflection and transmission of twisted light at phase conjugating interfaces," *Opt. Express 20*, 1301-1307 (2012).

[41]   Y. Yan et al., "Multipath effects in millimetre-wave wireless communication using orbital angular momentum multiplexing," *Sci. Rep.*, vol. 23, no. 6, pp. 33482, September 2016.

[42]   W. L. Stutzman and G. A. Thiele, "Wire Antennas," in *Antenna Theory and Design*, 3rd ed. Danvers, MA, UCA, John Wiley & Sons, 2012, ch. 6, sec. 6, pp. 190-191.

[43]   *PCB Material Selection for RF, Microwave and Millimeter-wave Design,* Isola Corporation, [Online]. Available:https://www.isola-group.com/wp-content/uploads/PCB-Material-Selection-for-RF-Microwave-and-Millimeter-wave-Designs-1.pdf.

[44]   D. M. Pozar, "Transmission lines and waveguides," in *Microwave Engineering*, 4th ed. Hoboken, NJ, USA: Wiley, 2012, ch. 3, sec. 8, pp. 148–149.

[45]   C. A . Balanis, "Fundamental parameters of antennas" in *Antenna theory and analysis and design*, 3rd edition, Hoboken, NJ, USA: John Wiley & Sons, Inc. 2005.

[46]   H. Yao, "Radio-frequency communication using higher-order Gaussian beams," PhD dissertation, The University of Texas at Dallas, 2018.

[47]   PULSE LARSEN ANTENNAS, "Technical data sheet, description – WiFi antenna," W1059 datasheet, May 2013.

BIOGRAPHICAL SKETCH

Lei Fang was born in Qinhuangdao, P. R. China, in 1988. He received a BS in Optical Information Science and Technology from Dalian University of Technology, Dalian, P. R. China, in 2011, a master degree in Optical Engineering from Dalian University of Technology in 2013, and is currently working toward his PhD in electrical engineering. His current research is on millimeter-wave antenna array design, simulation, and characterization of high order Laguerre-Gaussian radio waves for wireless communication. He is currently a research assistant in the High-Frequency Circuits and Systems Laboratory (HFCSL) of the Electrical Engineering Department at The University of Texas at Dallas.

CURRICULUM VITAE

Lei Fang

8610 Southwestern Blvd. #113, Dallas, TX, 75206.

Email: lxf140130@utdallas.edu

Industrial Professional Experience

Jul. 2018—Dec. 2018

RF Engineer Co-op (RF switch and antenna tuner products), Skyworks Solution, Inc. (Woburn, MA).

Jul. 2013—Jul. 2014

RF R&D Engineer, SAMSUNG ELECTRONICS CHINA (Samsung Mobile R&D Center China –Tianjin, SRC-Tianjin, H/W 4 Dept. Position #: 13627996).

Education

Sep. 2014—Present

Ph.D, Electrical engineering (RF engineering concentration), Department of Electrical and Computer Engineering, The University of Texas at Dallas.

GPA:3.806/4.0

Coursework: RFIC Design, RF & Microwave Systems Engineering, RF & Microwave Amplifier Design, Microwave Design & Measurement, Advanced Topic on RF Power Amplifier, Antenna Engineering, Fields & Waves, RF & Microwave Circuits, Analog IC Design, Semiconductor Process Integration, Random Process, Introduction of Wireless Communication.

Sep., 2011—Jul. 2013

Master, Optics Engineering, School of Physics and Optoelectronics Engineering, Dalian University of Technology, P. R. China.

GPA: 3.50/4.0

Thesis title: Research on Transceiver Module of Radio over Fiber Link Based on Directly Modulated DFB Laser Device

Advisor: Mingshan Zhao, Prof.

Sep. 2007—Jul. 2011

BS, Optical Information Science and Technology, School of Physics and Optoelectronics Engineering, Dalian University of Technology, P. R. China.

GPA: 3.50/4.0

Ranking: Top 15% among 173 students.

Technical Skills

1. RFIC Front End Module (FEM) design, verification and measurement, especially on RF switch and antenna tuner products on SOI die.

2. Smartphone RF Connectivity (BT/WiFi/GPS) parts circuits design, conduction and radiation performance verification and optimization.

3. PCB layout tools: Mentor (based on Linux), Protel, Cadence APD.

4. RF & EM simulation tools: HFSS, AWR, ADS and Momentum.

5. IC design and layout tool: Cadence.

6. Programming language: MATLAB, C, Labview, Python.

7. Electronic equipments: NSI Antenna chamber, VNA, Probe station, Impedance

analyzer, Agilent N4010, Anritsu MT8860C, Agilent 8960, Oscilloscope, Spectrum analyzer, Noise meter, etc.

Honors & Awards

2014-2015   UT Dallas School of Engineering and Computer Science Graduate Student Scholarship

2013   Award for 2013 Excellent New Employee in the introduction education & training of Samsung Electronics (China)

2011- 2013 First Grade Scholarship for Excellent Academic Record

2011   Fellowship for Graduate Study in Optics Engineering

2009-2010 College award for Undergraduate Innovative Experimental Program

2007-2009 Second Grade Scholarship for the excellent academic record(twice)

Research Experience

1. Skyworks Solutions, Inc. (Woburn, MA) period

As a Ph.D. Co-op RF engineer, I participated in some RF switch and antenna tuner projects based on GF SOI process. My main work includes Cadence schematic design, simulation, and verification using ADS dynamic-link, MCM matching, lab measurement (Ron/Coff using probe station and impedance analyzer, Vpeak & harmonics measurement, etc.), and X parameter modeling using ADS.

2. UT Dallas period

(1) Orbital Angular Momentum (OAM) Based mmWave Communication

I have been working on an NSF project, which is Orbital Angular Momentum (OAM) Based mm-wave Communication system, under the supervision of Dr. Rashaunda Henderson. I have

published 6 papers, and 1 more paper was accepted this semester (Spring 2019), and 2 more journal papers will be submitted soon.

(2) A QAM based Communication Project Using MATLAB to simulate and analyze a QAM based telecommunication system involved novel (Hermite-Gaussian) pulse to increase capacity and optimize the performance.

(3) Teaching Assistant Experience

More than 2-year TA working experience for 2 major graduate-level RF engineering lab courses: EERF 7V89 *Special Topics in RF and Microwave Systems - Active Microwave Circuit Desig*n & EERF 6396 *Microwave Design and Measurement*. The main content of the two courses includes microwave filter and coupler design, linear amplifier, LNA, VCO and Mixer design, etc. My work is to give guidance to the graduate students during their design process, teach them how to set up instruments and help to debug their designs during the lab measurement.

3. SAMSUNG Electronics China (SRC-Tianjin)period

I participated in two WCDMA smartphone projects as an RF R&D engineer, I was in charge of the realization of smartphone RF connectivity part, including the system design, conduction and radiation tuning and measurement.

4. Master period

I participated in two projects - *suppression of 3rd order inter-modulation distortion in Radio over Fiber link* and *high-frequency LO signal transmission using Radio over Fiber Link*. In both projects, I took charge of the design and realization of the laser device and photodetector driving circuits, auto power and temperature control circuits, LNA, and low ripple DC-DC power supply circuits.

Publications & Presentations

[1] **L. Fang**, R. M. Henderson, "Millimeter-Wave OAM Dipole Array with Reflector," **Paper** presented at the *53rd IEEE International Conference on Communications (ICC2019)*, Shanghai, China, May 2019.

[2] **L. Fang**, R. M. Henderson, "Orbital Angular Momentum Uniform Circular Antenna Array Design and Optimization-Based Array Factor," **Paper** presented at the *2019 Texas Symposium on Wireless and Microwave Circuits & Systems*, Waco, TX, March 2019.

[3] **L. Fang**, R. M. Henderson, "Orbital Angular Momentum Generation Using Dipole Array with Reflector," **Paper** presented at the *2019 European Microwave Week (EuMW2019)*, Paris, France, September 2019.

[4] **L. Fang**, H. Yao, R. M. Henderson, "Design and Performance of OAM Modes Generated using Dipole Arrays with Different Feeds," **Paper** presented at the *2018 Radio & Microwave Week (RWW2018)*, Anaheim, CA, January 2018.

[5] H. Yao, **L. Fang**, R. M. Henderson, "Evaluating conductive paint performance on 3-D printed horn antennas" **Paper** presented at the *2018 Radio & Microwave Week (RWW2018)*, Anaheim, CA, January 2018.

[6] **L. Fang**, H. Yao, R. M. Henderson, "OAM Antenna Arrays at E-Band," **Paper** presented at the 27th *International Microwave Symposium (IMS2017)*, Honolulu, HI, June 2017.

[7] **L. Fang**, R. M. Henderson, "Broadband Conductor-Backed Coplanar Waveguide to Double-Sided Parallel Strip Line Transition at Millimeter Wave," **Paper** presented at the *2017 Texas Symposium on Wireless and Microwave Circuits & Systems*, Waco, TX, April 2017.